Landslides triggered by the 1946 Ancash Earthquake (Peru) and geologic controls on the mechanisms of initial rock slope failure

by

Tanya Sandra Kampherm

A thesis
presented to the University of Waterloo
in fulfillment of the
thesis requirement for the degree of
Master of Science
in
Earth Sciences

Waterloo, Ontario, Canada, 2009

AUTHOR'S DECLARATION

I hereby declare that I am the sole author of this thesis. This is a true copy of the thesis, including any required final revisions, as accepted by my examiners.

I understand that my thesis may be made electronically available to the public.

Abstract

The 1946 M7.3 Ancash earthquake triggered a large number of landslides in an epicentral area along the continental divide in the Andes of Peru. Reconnaissance reports by Silgado (1947, 1951), Heim (1949) and Rüegg (1950) published shortly after the earthquake describe some of the landslides, but lack any detailed documentation. A review of literature, field traverses, aerial photograph interpretation and GIS mapping, identified 45 landslides inferred to have been triggered by the event. The three largest landslides occurred at Rio Llama (36,550,546 m^3), Suytucocha (13,503,994 m^3) and Quiches (10,582,563 m^3). The cumulative volume-frequency plot shows a strong power law relation, similar in form to that derived for landslides triggered by the 1994 Northridge earthquake (Harp and Jibson, 1995). Data for the Ancash earthquake plots near the regression line calculated by Keefer (1994), and modified by Malamud et al. (2004), for earthquake moment magnitude vs. total volume moved by landslides during the earthquake. A denudation (average surface lowering) of 76 mm and a denudation rate of 0.00585 mm/yr was estimated for the area over which the earthquake-triggered landslides occurred. Rock avalanches constituted 83% of the landslides which involved Cretaceous limestones interbedded with shales. Rock slope failures were common on slopes with a southwest aspect, an orientation corresponding to the regional dip direction of major planar structures in the epicentral area. In valleys oriented transverse to the NW-SE structural trend of the epicentral area, south-westerly dipping bedding planes combined with orthogonal joint sets to form numerous wedge failures. Three rock avalanches were analysed using conventional wedge failure criteria. Two of the rock avalanches which did not satisfy conventional criteria were utilized to develop a new criteria, i.e. stepped wedge criteria. Stepped wedge failure involves wedge movement along a stepped line of intersection formed by a nearly-vertical discontinuity, striking roughly parallel to the slope, and the conventional line of intersection formed by the bedding and orthogonal joint set. The nearly-vertical discontinuity forms the essential backscarp needed to facilitate stepped wedge failure. Additional characteristics of stepped wedge failure were also distinguished based on the wedge failures studied in the epicentral area of the 1946 Ancash earthquake. This work is the first detailed study and quantitative analysis of a landslide-inducing earthquake in Peru and in the Andean region.

Acknowledgements

I would like to thank a few people who were an integral part in the collaboration of this thesis project. Firstly, my thesis advisor, Dr. Stephen Evans, whose inspiration and knowledge guided me throughout the development and completion of this thesis. Secondly, Patricio Valderrama Murillo, geological engineeer with INGEMMET (Lima), who acted as an ever so knowledgeable field guide and provided crucial data for the compilation of this thesis. Lionel Fidel Smoll, Director de Geologia Ambientale y Riesgo Geologico at INGEMMET (Lima), who facilitated the support and collaboration of field work in Peru, as well as providing our field group with the greatest driver of Andean roads, known only as "Burrito". The support and collaboration of INGEMMET in this study is indeed very much appreciated. None of this research would have been possible without the funding provided by Dr. Stephen Evans' NSERC Discovery Grant as well as the NSERC Industrial Postgraduate Scholarship which I received in collaboration with and support of Golder Associates Ltd. John Gilby, of Golder Associates Ltd. in Mississauga was instrumental in this collaboration along with other Golder Associates employees, including Carla Evans and Paul Moser who provided invaluable GIS data and skills to the project. Jorge Chavez, of Golder Associates Ltd. in Lima, Peru also collaborated with the project and extended a warm welcome to me in Lima. Closer to home, fellow graduate students, Keith Delaney and Mona Khaleghy Rad, provided invaluable assistance while the University of Waterloo Map Library staff were invaluable in acquiring crucial data. Last but certainly not least, I would like to thank my husband Bob, who has supported me unconditionally throughout this tremendous endeavour with his steadfast patience and love.

Table of Contents

List of Figures

List of Tables

Chapter 1
Introduction

1.1 Landslide-Inducing Earthquakes in Peru

Earthquakes are a destructive force of nature which have resulted in massive loss of life in historical times (Utsu, 2002). The impacts may be magnified when they trigger landslides (Keefer, 1984; Bommer and Rodriguez, 2002; Khazai and Sitar, 2004) which impact on communities and infrastructure. Earthquake-triggered landslides frequently occur in regions which exhibit steep rock slopes, high relief, abundant precipitation, and widespread residual soils. Peru exhibits these types of regions, particularly in the high Andes. Although, earthquake-triggered landslides are a relatively common occurrence in the Andes, there is a surprising lack of detailed documentation regarding these events.

A review of earthquake catalogues for South America and descriptions of historical earthquakes indicates that a total of thirteen catastrophic landslide-inducing earthquake events greater or equal to magnitude 7.0 have occurred in Peru from 1890 to 2007 (Table 1. 1) (Appendix A). A landslide-inducing earthquake can be loosely defined as an earthquake which triggers significant landslide event(s) within the epicentral area of the earthquake. A review of historical earthquakes in the Andes (1890-2007) indicates that the highest frequency of landslide-inducing earthquakes within the Andean countries occurs in Peru, where a landslide-inducing earthquake of magnitude 7.0 or greater takes place approximately every 9 years. Based on the empirical relation developed by Keefer (1994), these earthquakes were responsible for a landslide-based denudation rate of 0.192 mm/yr. This rate can be compared to regional denudation rates for the Andes as a whole, which range from 0.01 to 6.9 mm/yr (Aalto et al., 2006).

1.2 The M7.3 1946 Ancash Earthquake, Peru

One of the thirteen earthquakes noted above is the M7.3 Ancash earthquake which occurred in the northern Andes of Peru in 1946. The 1946 Ancash earthquake (Table 1. 1) caused widespread landsliding throughout the epicentral area, including valley damming in the Pelagatos Valley, a massive rock avalanche in the Suytucocha Valley and the total burial of Acobamba village (Silgado, 1947; Heim, 1949, Rüegg, 1950, Silgado, 1951). Reconnaissance reports (Silgado, 1947; Heim, 1949; Rüegg, 1950; Silgado, 1951) conducted within the epicentral area shortly after the earthquake lack details on specific landslide locations, landslide characteristics and mechanisms of occurrence. Significant knowledge gaps therefore exist concerning the landslides triggered by the 1946 Ancash earthquake.

This thesis presents the first detailed account of landslides triggered in the 1946 Ancash earthquake and is the first detailed quantitative analysis of landslides triggered by an earthquake in the Andean region.

1.3 Investigation Methods

Research on landslides triggered by the 1946 Ancash earthquake was conducted through detailed field investigations throughout the epicentral area over 11 days in July and August of 2007 and 14 days in June and July of 2008 by vehicle and foot traverses. In preparation, an extensive literature review was conducted including earthquake catalogues, journal articles and books in order to gain a complete understanding of earthquake-triggered landslides in the Andes. Reconnaissance reports of the 1946 Ancash earthquake event were also reviewed in detail. Aerial photographs (scale 1:35,000) taken in 1962, obtained from the Instituto Geografico Nacional, were invaluable in providing a snapshot of the epicentral area 16 years after the event. Landsat 7 ETM+ imagery was used in conjunction with a geographic information system (ArcMap) to georeference the aerial photographs. Additional maps of the area were utilized, including digitized topographic maps (scale 1:100,000), digitized geological maps (scale 1:100,000) and paper contour maps (1:50,000). Datasets were obtained in order to map the continental divide (Centre for Research in Water Resources, 1999). Villages within the epicentral area were located using digitized maps outlined above as well as a data set acquired online from the GeoNET Names Server (National Geospatial - Intelligence Agency, 2008). In addition, a 25 m resolution digital elevation model (DEM) was utilized in order to obtain relevant information concerning slope and path geometry.

1.4 Objectives

In the following chapters two important aspects of the 1946 Ancash earthquake are examined. Firstly, a regional study is conducted to develop an earthquake-triggered landslide inventory for the 1946 event. Secondly, a dominant initial failure mechanism in rock avalanches triggered by the earthquake is examined with reference to the rock mass fabric measured at three rock slope failure sites.

The research conducted has four objectives:

1. Assemble and synthesize geophysical knowledge and impacts of the 1946 Ancash earthquake.
2. Compile an inventory of landslides triggered by the 1946 Ancash earthquake and examine characteristics of the ten largest landslides.
3. Examine initial failure mechanisms in rock avalanches in relation to wedge failure potential and evaluate rock mass fabric using conventional wedge failure criteria.

4. Develop new wedge failure criteria applicable to wedge failures within the epicentral area which do not meet conventional wedge failure criteria.

Objectives 1 and 2 are addressed in Chapter 2 whilst objectives 3 and 4 are addressed in Chapter 3.

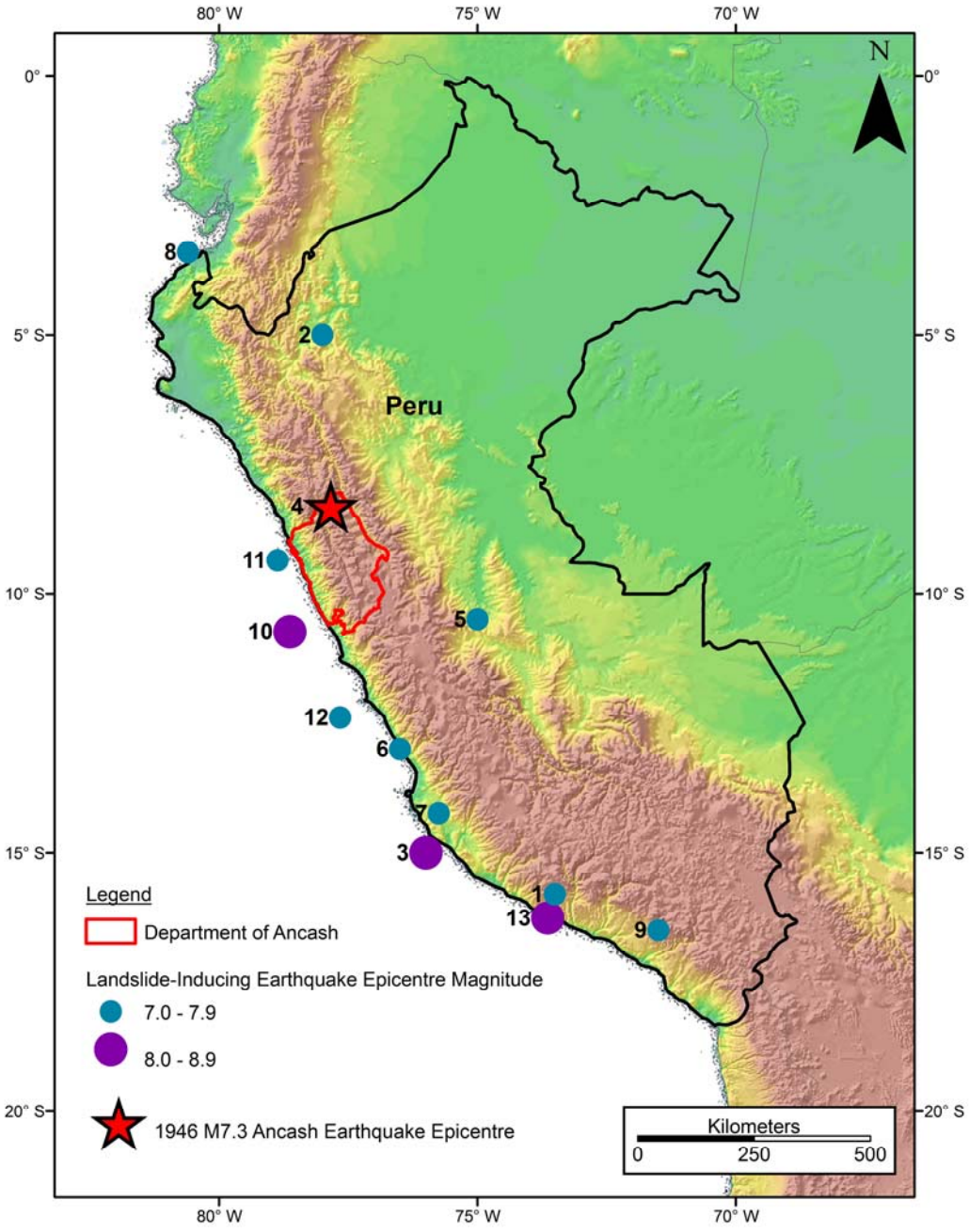

Figure 1. 1: Distribution of historical landslide-inducing earthquake epicentres in Peru (1890-2007)

Epicentres of landslide-inducing earthquakes greater than or equal to magnitude 7.0 between 1890 and 2007. Data derived from Silgado (1951), Ericksen et al. (1970), Plafker et al. (1971), Silgado, (1978), Silgado and Giesecke (1981), Alva Hurtado and Chang Chang (1985) and Keefer and Mosely (2004). Numbers adjacent to epicentres correspond to those in Table 1. 1.

Table 1. 1: Historical landslide-inducing earthquakes in Peru (1890-2007)

1946 M7.3 Ancash earthquake shown in shaded area.

Earthquake Number	Latitude	Longitude	Year	Month	Day	Earthquake Magnitude
1	15° 48′ 0″ S	73° 30′ 0″ W	1913	August	6	7.8
2	5° 0′ 0″ S	78° 0′ 0″ W	1928	May	14	7.3
3	15° 0′ 0″ S	76° 0′ 0″ W	1942	August	24	8.1
4	8° 19′ 0″ S	77° 50′ 18″ W	1946	November	10	7.3
5	10° 30′ 0″ S	75° 0′ 0″ W	1947	November	1	7.3
6	13° 0′ 0″ S	76° 30′ 0″ W	1948	May	28	7.0
7	14° 14′ 24″ S	75° 45′ 0″ W	1950	December	10	7.0
8	3° 24′ 0″ S	80° 36′ 0″ W	1953	December	12	7.8
9	16° 30′ 0″ S	71° 30′ 0″ W	1958	January	15	7.0
10	10° 44′ 24″ S	78° 37′ 48″ W	1966	October	17	8.1
11	9° 21′ 36″ S	78° 52′ 12″ W	1970	May	31	7.9
12	12° 23′ 24″ S	77° 39′ 36″ W	1974	October	3	7.6
13	16° 15′ 36″ S	73° 38′ 24″ W	2001	June	23	8.4

Chapter 2
Landslides triggered by the 1946 Ancash Earthquake, Peru

2.1 Introduction

The M7.3 1946 Ancash earthquake, which occurred in the northeastern region of the Western Cordillera in the Department of Ancash, triggered numerous landslides in the epicentral area of the earthquake (Silgado, 1947; Heim, 1949; Rüegg, 1950; Silgado, 1951). The landslides have never been documented in detail and only reconnaissance reports by Silgado (1947; 1951), Heim (1949) and Rüegg (1950) have been previously published. The reconnaissance reports (Silgado, 1947; Heim, 1949; Rüegg, 1950; Silgado, 1951) have important knowledge gaps such as precise locations of the landslides which were triggered by the earthquake and lack any detailed field documentation.

According to Silgado (1947) and Heim (1949), the 1946 Ancash earthquake was felt over an area of approximately 600,000 km^2. The region largely affected by the earthquake straddles the continental divide between 8° 9'S and 8° 39'S (Silgado, 1947). In addition to the occurrence of numerous landslides, many villages within the epicentral area were heavily damaged (Silgado, 1947; Rüegg, 1950; Silgado, 1951) and visible surface faulting was documented along the Quiches fault (Silgado, 1951; Bellier et al., 1991).

2.1.1 Objectives

The investigation of landslides triggered by the 1946 Ancash earthquake has four main objectives. Firstly, geophysical knowledge and impacts of the 1946 earthquake are synthesized. The earthquake is examined in detail including a description of the tectonic setting, epicentral area, impacts and effects and a review of the estimated recurrence interval for the earthquake. In addition, the regional setting of the epicentral area is described in terms of topography, structure and lithology. Secondly, the major focus is to create an inventory of earthquake-triggered landslides, utilizing geographic information systems (GIS) together with aerial photographs. A total of 45 landslides are documented in a table containing important landslide characteristics including location, failure type, geology, slope geometry, path geometry as well as area and volume estimates. Thirdly, the ten largest landslides triggered by the 1946 Ancash earthquake are described and summarized. Lastly, volume estimates of materials moved by the earthquake-triggered

landslides are compared to other earthquake-triggered landslide events worldwide and the approximate denudation and related denudation rate is calculated for the earthquake.

2.1.2 Methodology

Field work was conducted within the epicentral area of the 1946 Ancash earthquake over 11 days in July and August of 2007 and 14 days in June and July of 2008. Field traverses were made by vehicle and by foot across a number of landslide sites. Within the epicentral area, landslides previously documented by others were observed which then allowed us to calibrate our eye for additional landslides triggered by the 1946 Ancash event. Field observations were augmented by the interpretation of 1:35,000 scale aerial photographs taken in 1962 covering the VIII intensity isoseismal area. In addition, the 1962 aerial photographs were used to interpret a number of slides which were inaccessible by vehicle or foot. This type of interpretation is subject to a certain degree of uncertainty. Based on this, we believe that our interpretation of the landslides within the epicentral area has allowed us to formulate a best estimate of the number of landslides triggered by the 1946 Ancash earthquake.

Landslides inferred to have been triggered by the earthquake were plotted using ArcMap 9.2, a geographic information system (GIS) with the aid of Landsat 7 ETM+ imagery and a series of georeferenced aerial photographs (scale 1:35,000) covering the epicentral area taken between June and November 1962. The continental divide was mapped based on the Pacific and Atlantic drainage basins (Centre for Research in Water Resources, 1999). Bedrock geology for the epicentral area was obtained from digitized maps (Sanchez Fernandez, 1995), which also included faults and fold axes. Village locations in the epicentral area were obtained from a digitized 1:100,000 topographic data set. In addition, villages were located based on latitude and longitude measurements available through GeoNET Names Server (National Geospatial - Intelligence Agency, 2008) and plotted using GIS.

A digital elevation model (DEM) with a resolution of 25 m for the epicentral area was used in conjunction with the georeferenced aerial photographs to calculate the source slope angle and dip direction of each individual landslide. In addition, path height and length of the ten largest landslides were calculated using the DEM and GIS. Using path height and length, the fahrböschung (Figure 2. 1) was also calculated for the ten largest landslides. Finally, the area of the debris for each individual landslide was mapped based on field observations and air photo interpretation and calculated using GIS and georeferenced aerial photographs. An error of 10% is estimated for the values obtained in GIS. A detection threshold of approximately 1,750 m^2, the area of the smallest landslide which was recorded, exists for the landslide mapping. Thus landslides smaller than this area were not included in the inventory.

2.2 The 1946 Ancash Earthquake

The Ancash, Peru earthquake occurred on Sunday, November 10, 1946 at 17:43 (GMT), 12:43 local time (Silgado, 1951). The magnitude of the earthquake was recorded as 7.3 with a focal depth of 30 – 40 km (Silgado, 1951). A strong detonation was heard near the village of Mayas following the earthquake and the shaking there was reportedly so violent that people were unable to stand (Silgado, 1951). Successive aftershocks continued in the area for a period of many months after the initial shock (Rüegg, 1950; Silgado, 1951). Epicentre coordinates were reported as 8° 19' 00" S and 77° 50' 18" W (Silgado, 1951), calculated based on the analysis of original seismograms from several stations and a least-squares adjustment. The earthquake affected the northern region of the Department of Ancash and the southern region of the Department of La Libertad (Silgado, 1947).

2.2.1 Tectonic Setting

The Andes mountain chain has developed as a result of the subduction of the Pacific oceanic plate (Nazca plate) beneath the South America continental plate (Suárez et al., 1983) (Figure 2. 2). The Nazca plate has been undergoing subduction at a shallow dip in the plate-vergence direction of 078° ± 10° at an approximate convergence rate of 11.0 ± 0.8 cm/yr (McNulty et al., 1998). In the region of Ancash, the Nazca plate is subducted almost horizontally beneath the South American plate at a very shallow dip of 10°–15°, making this segment one of the largest zones of flat subduction in the world (Stauder, 1975; Doser, 1987; Norabuena and Snoke, 1994). The 1946 Ancash earthquake occurred in the interior of the South American plate; it is therefore an intraplate earthquake (Doser, 1987). This is significant since intraplate earthquakes tend to exhibit a much longer recurrence interval than those earthquakes which occur at plate margins (Johnston and Kanter, 1990).

2.2.2 Epicentral Area

The Ancash earthquake was felt over an area of approximately 600,000 km^2 (Silgado, 1947; Heim, 1949). The provinces of Pallasca and Pomabamba in the northern region of the Department of Ancash (Figure 1. 1) were subjected to macroseismic effects (Heim, 1949; Rüegg, 1950; Silgado, 1951; Silgado, 1978; Silgado and Giesecke, 1981). The epicentral area of the earthquake is located between 8° 10' S and 8° 26' S and 77° 27' W and 77° 52' W (Silgado, 1978). An isoseismal map of the epicentral area (Silgado, 1951) shows the maximum isoseismal intensity of IX bounding a NW-SE elliptical area of approximately 500 km^3 (Figure 2. 3). Intensities were mapped (Silgado, 1951) based on field observations of topographical changes, including landslides and other secondary effects. The shape of the isoseismals in the epicentral area suggests that the Quiches fault, along which visible surface faulting occurred, is the main fault

associated with the earthquake. The elliptical shape of the isoseismals could also be a result of the topographic effect controlled by the steep gorge of the Marañón River to the east (Doser, 1987).

2.2.3 Impacts and Effects

An extensive array of impacts resulted from the intense ground shaking in the epicentral area. Numerous villages were destroyed and important secondary effects occurred across the epicentral area including surface faulting and landslides.

2.2.3.1 Impacts on Villages

Approximately 1400 people died in the Ancash earthquake (Silgado, 1951). The large loss of life and extensive damage to villages in the epicentral area may be in part due to the poor construction of buildings in addition to the fact that many of the villages were built on alluvium debris where ground shaking by the earthquake was amplified (Rüegg, 1950; Doser, 1987). In addition, the village of Acobamba was buried by a major rock/debris avalanche.

Extensive destruction and death occurred in the villages of Acobamba, Sihuas, Quiches, Conchucos, and Pampas (Table 2. 1) (Figure 2. 3) (Silgado, 1947). The present day setting of Pampas and Conchucos is seen in Figure 2. 4.

Table 2. 1: Village locations within the epicentral area where major destruction occurred in the 1946 Ancash earthquake (summarized after Silgado, 1947)

Locations determined in this study.

Village	Latitude	Longitude	% Destruction	Total Deaths
Acobamba	8° 19′ 33″ S	77° 34′ 56″ W	100%	217
Sihuas	8° 33′ 18″ S	77° 37′ 54″ W	98%	133
Quiches	8° 23′ 38″ S	77° 29′ 27″ W	98%	677*
Conchucos	8° 16′ 2″ S	77° 51′ 09″ W	95%	151
Pampas	8° 11′ 45″ S	77° 53′ 43″ W	60-70%	210

* Total deaths includes 419 people from the villages of Quilca, Acobamba, Huasco, Chingalpo and San Miguel.

In addition, many other Andean villages within the epicentral area were partially destroyed (Table 2. 2) (Figure 2. 3) (Silgado, 1947; Silgado, 1951).

Table 2. 2: Village locations where minor destruction occurred in the 1946 Ancash earthquake (Silgado, 1947; Silgado, 1951).

Locations determined in this study.

Village	Latitude	Longitude	Damages
Casablanca	8° 24′ 53″ S	77° 32′ 54″ W	Minor
Chalan	8° 11′ 7″ S	77° 41′ 0″ W	Minor
Chingalpo	8° 20′ 20″ S	77° 35′ 48″ W	Minor
Citabamba	8° 2′ 0″ S	77° 44′ 0″ W	Minor
Corongo	8° 34′ 15″ S	77° 53′ 53″ W	Minor
Huasco	8° 20′ 16″ S	77° 33′ 24″ W	Minor
Jocosbamba	8° 23′ 33″ S	77° 32′ 24″ W	Minor
Llama	8° 25′ 3″ S	77° 38′ 42″ W	Minor
Mayas	8° 16′ 20″ S	77° 39′ 53″ W	Minor
Mollebamba	8° 10′ 0″ S	77° 58′ 0″ W	Minor
Mollepata	8° 12′ 0″ S	77° 57′ 0″ W	Minor
Pasta Bueno	8° 10' 6" S	77° 49' 52" W	Minor
Quilca	8° 19′ 21″ S	77° 34′ 1″ W	Minor
San Miguel	8° 21′ 45″ S	77° 39′ 37″ W	Minor
Soledad	8° 40′ 0″ S	78° 0′ 0″ W	Minor

2.2.3.2 Surface Effects

In addition to the destruction of many Andean villages, extensive surficial cracks due to earthquake-induced ground failure were observed throughout the epicentral area near Quiches, Mayas, Huancabamba, Conchucos and Citabamba (Silgado, 1951).

Surface faulting was also observed along the Quiches fault (Silgado, 1951; Doser, 1987; Bellier et al., 1991). The Quiches fault (Figure 2. 3) is situated at an elevation of 3600 to 4100 m near the village of Quiches within the northwest-southeast striking Marañón Thrust and Fold Belt, which forms the

northeastern part of the Western Cordillera (Bellier et al., 1991). The 1946 Ancash earthquake produced approximately 20 km of discontinuous northwest-southeast striking normal fault scarps in the vicinity of Quiches (Doser, 1987). The 1946 earthquake faulting is defined by southwest facing scarps which displace late Quaternary fluvio-glacial deposits, as well as Mesozoic limestones and sandstones along an older, pre-existing fault (Bellier et al., 1991). The southernmost segment is 5 km long with a strike of N 42° W and dip of S 58° W with a maximum vertical displacement of 3.5 m (Silgado, 1951). The northernmost segment is 3 km with a strike of N 55° W and maximum displacement of 1 m (Silgado, 1951).

2.2.3.3 Landslides

In addition to the destruction of villages within the epicentral area of the 1946 Ancash earthquake a large number of landslides occurred within the region (Heim, 1949; Silgado, 1951). Approximately 500 people were killed due to landslides in the epicentral area, including 217 deaths in the village of Acobamba (Silgado, 1951). It is probable that the high degree of topographical amplification may in part explain the large number of mass movements which occurred within the epicentral area.

2.2.4 Recurrence Interval

Surface ruptures along the Quiches fault during the 1946 event displaced Quaternary deposits and Mesozoic sedimentary rocks (Bellier et al., 1991). Morphological analysis of the fault scarp and field observations of an excavated trench across the fault (Bellier et al., 1991) showed evidence of a single normal-fault displacement prior to the 1946 seismic event which offset late Pleistocene deposits. The single normal-fault displacement prior to 1946 earthquake is older than the younger moraine deposits but postdates the older moraine deposits (Bellier et al., 1991). According to age estimations of the Quiches moraines, the single normal fault displacement prior to 1946 occurred in the Late Pleistocene prior to the last glaciation at approximately 13,000 years B.P. (Bellier et al., 1991). Thus the maximum recurrence interval for major surface faulting earthquakes on the Quiches fault can be estimated at approximately 13,000 years (Bellier et al., 1991; Macharé et al., 2003). This recurrence interval is further supported by the fact that the Peruvian catalogue of historical seismicity (Silgado, 1978) reported no shallow earthquakes in the Quiches region between 1513 and 1946 (Bellier et al., 1991). In addition, Silgado (1978) has reported relatively low seismicity in the Quiches region since 1946 with the strongest earthquake occurring on May 5, 1971 with a magnitude of 4.9 (Bellier et al., 1991).

The maximum vertical displacement of 3.5 m reported during the 1946 Ancash earthquake surface faulting and a recurrence interval of 13,000 years indicates an estimated slip rate for the Quiches fault at

less than 0.25 mm/yr (Bellier et al., 1991; Macharé et al., 2003). Clearly, this indicates a very long recurrence interval for major intraplate earthquakes in the epicentral area of the 1946 Ancash earthquake.

2.3 Regional Setting of Epicentral Area

2.3.1 Topography

The epicentral area of the Ancash earthquake is located on the northeastern edge of the Western Cordillera of the Andes of Peru, also known as the Cordillera Occidental, along the continental divide where elevations range from 1600 to 4800 m.a.s.l. (Figure 2. 5) (Silgado, 1978). The rugged topography in the epicentral area corresponds to an old erosional plateau (Silgado, 1978) with deeply dissected V-shaped valleys and rivers with stream gradients of 200m/km (Doser, 1987). Summits and valleys within the epicentral area show evidence of Pleistocene glaciation (Silgado, 1951).

2.3.2 Structure

The bedrock structure of the epicentral area along the continental divide consists of northwest-southeast trending folds and faults (Figure 2. 6) (Silgado, 1947; Wilson, 1963). Mesozoic rocks within the epicentral area display structures similar to those of a foreland fold and thrust belt (Suárez et al., 1983). Many conformable Mesozoic sequences consist of a series of stacked thrust sheets which are thrust over one another (Wilson, 1963). The folds and thrusts in this area are generally of the flexural slip type with both broad-rounded hinges and chevron geometry (Suárez et al., 1983). The Mesozoic sequences were thrust eastward over gentle west dipping faults, while underlying Jurassic shales formed tight flexural slip folds (Heim, 1949; Suárez et al., 1983; Doser, 1987; Bellier et al., 1991). The tectonic style implies detachment of the Mesozoic cover from an older substratum and extensive east-west shortening (Suárez et al., 1983). Major structures within the epicentral area are parallel to the northwest-southeast orientation of the continental margin (Silgado, 1978; Cobbing et al., 1981). Thrust sheets impart a structural fabric to the landslide-forming rock masses with major planar structures dipping to the southwest. Topography is dominated by strike valleys (Figure 2. 6) as well as valleys running transverse to the structural grain.

2.3.3 Lithology

Rocks in the epicentral area of the Ancash earthquake are mostly sedimentary and Cretaceous in age and are overlain by alluvial, eluvial and fluvial formations Pleistocene and Holocene in age (Silgado, 1947). The large number of landslides that occurred throughout the epicentral area mostly involved Cretaceous sedimentary rocks, including limestones, shales and sandstones.

Rock slope failures inferred to have been triggered by the Ancash earthquake within the epicentral area occurred within five mapping units of Cretaceous age (Figure 2. 7). A regional stratigraphical column (Figure 2. 8) shows period, epoch, mapping unit, formation, thickness, metres below top of Celendin Formation, relative resistance (as estimated from field exposures) and the number and percentage of landslides per formation. In the following each mapping unit is described from oldest to youngest.

Chimu Formation (Ki-chi)

The Chimu Formation consists of approximately 700 m of orthoquartzites with shale and coal intercalations (Figure 2. 8) (Benavides-Cáceres, 1956; Wilson, 1963; Cobbing et al., 1981). The orthoquartzites are white to light grey in colour but light reddish brown to light grey once exposed (Benavides-Cáceres, 1956). In addition, the orthoquartzites of the Chimu Formation are hard and thickly bedded with well developed cross-bedding (Benavides-Cáceres, 1956; Wilson, 1963; Cobbing et al., 1981). The Chimu Formation overlies the upper Jurassic Chicama Formation (Benavides-Cáceres, 1956; Wilson, 1963; Cobbing et al., 1981).

Santa/Carhuaz formations (Ki-saca)

The Santa Formation consists of approximately 300 m of limestones and shales (Figure 2. 8) (Benavides-Cáceres, 1956; Wilson, 1963; Cobbing et al., 1981). The northern facies of the Santa Formation lies north of Huaraz and consists mainly of grey shales, with subsidiary intercalations of limestones (Cobbing et al., 1981). The Carhuaz Formation consists of approximately 1500 m of shales, siltstones and quartz sandstones with thin intercalations of limestone (Figure 2. 8) (Benavides-Cáceres, 1956; Wilson, 1963; Cobbing et al., 1981). The thin to medium interbedded shales, siltstones and quartz sandstones are grey and brown in colour (Benavides-Cáceres, 1956; Wilson, 1963; Cobbing et al., 1981).

Farrat Formation (Ki-f)

The Farrat Formation consists of over 250 m of protoquartzites and orthoquartzites (Figure 2. 8) (Wilson, 1963; Cobbing et al., 1981). The orthoquartzites and protoquartzites are white or grey in colour, medium to coarse grained and moderate to poorly sorted (Wilson, 1963; Cobbing et al., 1981).

Parihuanca/Chulec/Pariatambo formations (Kis-Pchp)

The Parihuanca Formation consists of approximately 100 m of limestones with lesser amounts of calcareous sandstone and shale (Figure 2. 8) (Benavides-Cáceres, 1956; Wilson, 1963; Cobbing et al., 1981). The limestones are massive, medium to thickly bedded and grey in colour (Benavides-Cáceres, 1956; Wilson, 1963). The Chulec Formation consists of approximately 250 m of shales interbedded with limestones and calcareous sandstones (Figure 2. 8) (Benavides-Cáceres, 1956; Wilson, 1963; Cobbing et

al., 1981). The formation is light coloured and very fossiliferous (Benavides-Cáceres, 1956; Wilson, 1963). The Pariatambo Formation consists of approximately 200 m of bituminous shales interbedded with fetid limestones and cherts (Figure 2. 8) (Benavides-Cáceres, 1956; Wilson, 1963; Cobbing et al., 1981). The black or dark colour of this unit distinguishes it from the light-coloured Chulec and Jumasha formations (Benavides-Cáceres, 1956; Wilson, 1963).

Jumasha/Celendin formations (Kis-jc)

The Jumasha Formation consists of approximately 800 m of limestones and dolomites (Figure 2. 8) (Benavides-Cáceres, 1956; Wilson, 1963; Cobbing et al., 1981). The unit is characteristically light gray in colour and is topographically prominent throughout the mountains along the continental divide (Wilson, 1963). The Celendin Formation consists of approximately 300 m of shales interbedded with limestones (Figure 2. 8) (Benavides-Cáceres, 1956; Wilson, 1963; Cobbing et al., 1981). The shales are soft, yellow in colour and very fossiliferous (Benavides-Cáceres, 1956; Wilson, 1963).

2.4 Landslides

A total of 45 landslides were inferred to have been triggered by the 1946 Ancash earthquake within the epicentral area (Figure 2. 9). Six of these landslides, Rio Llama, Suytucocha, Quiches, Pelagatos, Acobamba and Peñacocha, were reported in earlier studies of the 1946 Ancash earthquake (Heim, 1949; Silgado, 1951). However, the remaining 39 landslides were mapped as part of this study using methods outlined above in the section on methodology. Of those landslides which are not previously documented, the nature of the debris, occurrence of the failure and similar patterns of vegetation suggest an occurrence similar in time to the other landslides documented at the time of the 1946 earthquake. The characteristics of the 45 landslides inferred to have been triggered by the 1946 earthquake, include type of failure, latitude, longitude, isoseismal area, distance to epicentre, mapping unit, formation, slope dip direction, slope angle, path height, path length, fahrböschung, area and volume which are reported in Table 2. 3.

2.4.1 Landslide Characteristics

A number of different types of landslides occurred, including rock avalanches, debris avalanches, rock slides, flowslides and rock falls (Table 2. 3). 83% of the landslides were rock avalanches. Only 8% of the landslides were debris avalanches, 4% were rockslides and 4% were flow slides and rock falls.

Landslides occurred from 8° 10' 35"S to 8° 26' 21"S and from 77° 30' 18"W to 77° 49' 8"W within the VIII and IX intensity isoseismals of the epicentral area, with 80% of landslides occurring within the IX intensity isoseismal (Table 2. 3) on both sides of the continental divide (Figure 2. 9). Landslides occurred as close as 7.3 km to the epicentre of the earthquake and as far as 38.9 km (Table 2. 3).

All the landslides occurred in Cretaceous sedimentary rocks, with 60% in the Jumasha/Celendin formations (Kis-jc), 36% in the Parihuanca/Chulec/Pariatambo formations (Kis-Pchp) and 2% in both the Farrat Formation (Ki-f) and Santa/Carhuaz and Chimu formations (Ki-saca) (Ki-chi) (Figure 2. 8) (Table 2. 3). As noted above, 80% of the landslides occurred within the IX isoseismal. 53% of these landslides occurred in the Kis-jc which underlies only 21% of the IX isoseismal area. This indicates that this Cretaceous unit was particularly prone to earthquake-triggered rock slope failure.

Source slope dip direction measurements (Table 2. 3) of all 45 landslides within the epicentral area show a strong southwest trend (Figure 2. 10). This indicates that rock slopes oriented perpendicular to the major structural trend in the epicentral area and sloping parallel to the southwest regional dip of major planar structures were particularly prone to failure. Southwest dipping bedding planes occur throughout the epicentral area in valleys which are both parallel and transverse to the strike of the structural trend.

Source slope angles for the landslides ranged from 15° to 46° (Table 2. 3). 48% of landslides occurred on a slope angle between 31° and 40° (Figure 2. 11). Mapping units did not appear to have any dominant effect on the angle of the source slope (Figure 2. 11).

Debris areas of the landslides measured on georeferenced aerial photographs ranged from approximately 1,800 m^2 to 1,400,000 m^2 (Table 2. 3). Estimates of debris volumes of all 45 landslides were calculated based on areas using the regression equation, developed for estimating the volume of rock avalanches, with an r^2 value of 0.95 (S.G. Evans, Personal Communication, 2008):

$$\text{Volume} = 0.02999282568 * \text{Area}^{1.4784627} \qquad \text{[Equation 2. 1]}$$

Volumes of the landslides calculated from Equation 2. 1 ranged from approximately 2,000 m^3 to 37,000,000 m^3 (Table 2. 3).

In addition to the other landslide characteristics, path height, length and fahrböschung (defined in Figure 2. 1) were calculated for the ten largest landslides in the epicentral area. The fahrböschung ranged from 11° to 24° for the ten largest landslides (Table 2. 3).

2.5 Major Landslides Triggered by the Ancash Earthquake

The location, geology, slope and path geometry and metrics of the ten largest landslides (Figure 2. 12) within the epicentral area are summarized below.

2.5.1 Rio Llama Rock Avalanche

The Rio Llama rock avalanche (Figure 2. 13 and 2. 14) (8° 23' 53" S, 77° 35' 26" W) is located approximately 29 km southeast of the epicentre within the IX intensity isoseismal (Figure 2. 12). The

landslide has not been previously reported in any detail and has only been mentioned in previous studies as occurring near the village of Llama at the time of the earthquake (Silgado, 1951, p.92).

The source slope of the Rio Llama rock avalanche is underlain by limestone, shale and calcareous sandstone of the Parihuanca, Chulec and Pariatambo formations (Sanchez Fernandez, 1995) (Figure 2. 7). An average source slope angle of 38° and slope dip direction of S 210° W was estimated for the rock avalanche source area (Table 2. 3). Aerial photo interpretation shows that the rock avalanche initiated on a bedding plane with an approximate dip of 27° and dip direction of 221° (Figure 2. 13) and the initial direction of movement was parallel to the southwest dip direction of the bedding plane. Topographic features appear to have re-directed the failure in a southerly direction before reaching the valley bottom where the flow was once again re-directed downstream to the east (Figure 2. 13).

The Rio Llama rock avalanche is the largest landslide triggered by the 1946 earthquake. The debris covers an approximate area of 1,400,000 m^2 with an estimated volume of 37,000,000 m^3 (Table 2. 3). The height of the rock avalanche path is estimated at 1,300 m with a run out distance of approximately 5,000 m. A fahrböschung of 15° was calculated for the rock avalanche, the low angle reflecting the long run-out of the debris. The Rio Llama rock avalanche appears to have entrained colluvium as it descended the slope since the debris is composed of small blocks in a finer matrix (Figure 2. 14).

2.5.2 Suytucocha Rock Avalanche

The Suytucocha rock avalanche (Figure 2. 15, 2. 16 and 2. 17) was reported as being triggered by the 1946 Ancash earthquake (Heim, 1949; Silgado, 1951). The landslide killed 200 farmers/shepherds who had gathered in the valley to help with sheep shearing, according to a local woman from the village of Mayas, who was interviewed during our field work in the area. The Suytucocha rock avalanche (8° 16' 35" S, 77° 43' 4" W) is located approximately 14 km northeast of the epicentre within the IX intensity isoseismal (Figure 2. 12).

The source slope is underlain by limestone, shale and calcareous sandstone of the Parihuanca, Chulec and Pariatambo formations (Sanchez Fernandez, 1995) (Figure 2. 7). An average slope angle of 40° and slope dip direction of S 152° E was estimated for the source area (Table 2. 3). Field observations indicate that the Suytucocha rock avalanche is a wedge failure (Hoek and Bray, 1977) formed by the intersection of southwest dipping bedding planes and a set of east dipping discontinuities, in addition to a nearly-vertical southeast dipping set of discontinuities forming the backscarp (Figure 2. 15).

The Suytucocha rock avalanche path has an approximate height (H) of 400 m and a run out (L) of over 2000 m (Table 2. 3). A low fahrböschung ($\tan^{-1}$H/L) of 11° indicates the high mobility of the rock avalanche. Initial movement of the rock mass forming the wedge was to the south. Upon reaching the

valley bottom the debris continued downstream to the east (Figure 2. 16). The debris covers an approximate area of 700,000 m^2 with an approximate volume of 13,500,000 m^3 (Table 2. 3). A previous volume estimate of 500,000 m^3 was estimated by Heim (1949).

Large sections of the original land surface were preserved within the debris of the rock avalanche (Figure 2. 18) and multiple scarps were evident throughout the debris indicating the occurrence of secondary movement (Figure 2. 16). Secondary movement occurs when a decrease in the velocity of the debris movement allows debris to pile up. Secondary movement may have been facilitated by mobilization of the finer valley bottom sediments that appear to have been squeezed out from the sides of the rock avalanche (Figure 2. 18) as a result of the impact loading of the debris. Suytucocha Valley was the site of an empty lake bed prior to the occurrence of the rock avalanche (Heim, 1949). Evidence of a former lake bed was found on the upstream limit of the debris within the valley bottom (Figure 2. 18).

2.5.3 Quiches Debris Avalanche

The Quiches debris avalanche (Figure 2. 19, 2. 20 and 2. 21) (8° 23' 35" S, 77° 30' 18" W) is located approximately 38 km from the earthquake epicentre within the IX intensity isoseismal (Figure 2. 12). The debris avalanche was reported as the failure of Huaychachaco hill due to the 1946 Ancash earthquake (Heim, 1949; Silgado, 1951). The Quiches debris avalanche along with associated failures along the same slope are shown in an aerial photograph by Heim (1948) (Figure 2. 20). Field observations indicated that the Quiches debris avalanche and the other earthquake-triggered failures noted in Figure 2. 20 occurred along a reverse slope where the dip of the Cretaceous strata is into the slope. This is also evident in the profile of the Quiches debris avalanche (Figure 2. 22) (Heim, 1949).

The slope is underlain by limestone, shale and calcareous sandstone of the Parihuanca, Chulec and Pariatambo formations (Sanchez Fernandez, 1995) (Figure 2. 7). An average slope angle of 35° in the source area and slope dip direction of N 036° E was estimated.

The height of the Quiches debris avalanche path (H) is estimated at 600 m with a run out (L) of 1,700 m (Table 2. 3). Similar values are obtained from a profile constructed by Heim (1949) (Figure 2. 22). Based on the height and length of the debris avalanche, a fahrböschung ($\tan^{-1}H/L$) of 21° was calculated.

The debris covers an approximate area of 600,000 m^2 with an approximate volume estimated from Equation 2. 1 of 10,000,000 m^3. A previous volume estimate of the Quiches debris avalanche is 5,000,000 m^3 (Silgado, 1947). The debris of the Quiches debris avalanche consisted of larger blocks within a finer matrix of shattered rock. A large amount of shattered rock colluvium was also evident in the area of the landslide scarp and strongly suggests the occurrence of fault related alteration.

2.5.4 Pelagatos Rock Avalanche

The Pelagatos rock avalanche (Figure 2. 23 and 2. 24) (8° 10' 35" S, 77° 49' 3" W) is located approximately 16 km north of the 1946 Ancash earthquake epicentre within the IX intensity isoseismal (Figure 2. 12). This rock avalanche was reported as being triggered by the 1946 Ancash earthquake (Heim, 1949; Silgado, 1951). The 1946 Pelagatos rock avalanche is the most recent failure to have occurred in this area. Heim (1949) reported the occurrence of a prehistoric landslide that created a landslide dam and formed Pelagatos Lake. The prehistoric rock avalanche is shown in Figure 2. 24.

The slope is underlain by orthoquartzites, limestones, shales and siltstones of the Santa, Carhuaz and Chimu formations (Sanchez Fernandez, 1995) (Figure 2. 7). In addition, field observations showed larger blocks within a finer matrix of colluvium and highly metamorphosed rocks in the debris (Figure 2. 25), suggesting that the initial failure may have occurred along a fault contact zone.

The Pelagatos rock avalanche debris formed a landslide dam (Figure 2. 24). According to Heim (1949) and Rüegg (1950), the landslide dam created by the Pelagatos rock avalanche formed two small ponds in the valley bottom (Figure 2. 24).

An average slope angle of 31° and slope dip direction of N 013° E was estimated for the rock avalanche source area. A height of approximately 600 m and run out distance of 1,300 m was estimated for the Pelagatos rock avalanche path (Figure 2. 24). Based on these measurements, a fahrböschung of 24° was calculated.

The debris covers an approximate area of 500,000 m^2 with an approximate volume of 8,000,000 m^3 (Table 2. 3). A previous estimate of 25,000,000 m^3 was reported by Silgado (1951).

2.5.5 Shundoy Rock Avalanche

The Shundoy rock avalanche (Figure 2. 26) (8° 15' 55" S, 77° 46' 49" W) is located approximately 9 km northeast of the 1946 Ancash earthquake epicentre within the IX intensity isoseismal (Figure 2. 12). The Shundoy rock avalanche has not been previously reported and was not visited in the field. However, aerial photo interpretation strongly suggests that it occurred within the same time frame as the previously documented 1946 landslides and is inferred to have been triggered by the earthquake.

The source slope is underlain by sedimentary rocks, largely composed of limestone, dolomite and calcareous shale of the Jumasha and Celendin formations, Late Cretaceous in age (Sanchez Fernandez, 1995) (Figure 2. 7).

The approximate height of the Shundoy rock avalanche path is 400 m while the run out was estimated at 1,700 m. A fahrböschung of 13° of was calculated based on these measurements.

The Shundoy rock avalanche initiated along the western limb of a syncline and therefore originated as a dip slope failure. An average slope angle of 20° and slope dip direction of S 147° E was estimated for the source area of the rock avalanche (Table 2. 3). Initial failure of the Shundoy rock avalanche occurred along northeast dipping bedding planes and debris diverted to the southeast by topography (Figure 2. 26). The debris covers an approximate area of 500,000 m^2 with an approximate volume of 8,000,000 m^3 (Table 2. 3).

2.5.6 Acobamba Rock/Debris Avalanche

Silgado (1947) reported that the Acobamba rock/debris avalanche was triggered by the 1946 Ancash earthquake (Figure 2. 27 and 2. 28) and buried the village of Acobamba killing a total of 217 people. The Acobamba rock/debris avalanche (8° 19' 51" S, 77° 35' 23" W) is located approximately 27 km southeast of the earthquake epicentre within the VIII intensity isoseismal (Figure 2. 12).

An average slope angle of 31° and slope dip direction of S 207° W was estimated for the source slope (Table 2. 3). The Acobamba rock/debris avalanche initiated in bedrock on a southwest dipping bedding plane located in the hills to the northeast of the village (Figure 2. 27 and 2. 28). The rock avalanche entrained colluvium as it descended the slope and was transported into a rock/debris avalanche. The massive amount of debris was redirected by topography to the southeast (Figure 2. 28). The debris continued moving southeast covering the entire village of Acobamba. Field work led to the discovery of a partially buried structure located along the eastern boundary of the debris (Figure 2. 28 and 2. 29).

The source slope is underlain by limestone, shale and calcareous sandstone of the Parihuanca, Chulec and Pariatambo formations (Sanchez Fernandez, 1995) (Figure 2. 7). The debris of the Acobamba rock/debris avalanche is composed of small blocks in a finer matrix of colluvium (Figure 2. 30) which is also demonstrated in a 1946 photograph taken at the site following the occurrence of the failure (Figure 2. 30).

The height and run out of the Acobamba rock/debris avalanche path is estimated at 800 m and 2000 m respectively (Table 2. 3). Based on these measurements a fahrböschung of 20° was calculated. The run-out of the debris over the village of Acobamba is over a low angle surface. The debris depth was estimated by Silgado (1947) at approximately 20 m. An area of approximately 330,000 m^2 was calculated for the debris with an approximate volume of 4,300,000 m^3 (Table 2. 3) being indicated by Equation 2. 1 and suggesting an average depth of 13 m.

2.5.7 Lechecocha 1 Rock Avalanche

The Lechecocha 1 rock avalanche (Figure 2. 31 and 2. 32) (8° 11' 60" S, 77° 45' 2" W) is located approximately 16 km northeast of the earthquake epicentre within the IX intensity isoseismal (Figure 2. 12). This rock avalanche was not reported as being triggered by the 1946 Ancash earthquake. However, field observations and aerial photo interpretation suggest that it occurred around the same time as the reported earthquake-triggered 1946 landslides.

The source slope forms the continental divide and is underlain by limestone, shale and calcareous sandstone of the Parihuanca, Chulec and Pariatambo formations (Sanchez Fernandez, 1995) (Figure 2. 7). An average slope angle of 21° and slope dip direction of S 204° W was estimated in the source area. The Lechecocha 1 rock avalanche initiated as a wedge failure (Figure 2. 31). A height of approximately 700 m and run out of 1,700 m yielded a fahrboschung of 24° for the rock avalanche path (Table 2. 3). The debris of the Lechecocha 1 rock avalanche covers an approximate area of 200,000 m^2 with an approximate volume of 2,000,000 m^3 (Table 2. 3).

2.5.8 Paccha Flowslide

The Paccha flowslide (Figure 2. 33 and 2. 34) was not reported as occurring in the 1946 Ancash earthquake. However, field observations indicate its occurrence within the same time frame as other landslides reported during the 1946 event. The Paccha flowslide (8° 26' 21" S, 77° 30' 26" W) is located approximately 39 km southeast of the 1946 Ancash earthquake epicentre within the IX intensity isoseismal (Figure 2. 12).

Although the source slope is underlain by Cretaceous rocks of the Parihuanca, Chulec and Pariatambo formations (Sanchez Fernandez, 1995) (Figure 2. 7), the flowslide occurred in glacial moraine or colluvial cover (Figure 2. 35).

An average slope angle of 23° and slope dip direction of S 139° E was estimated for the Paccha flowslide. The failure occurred on the north side of the valley and debris flowed downslope into the valley bottom, running up the other side before being deflected downstream to the east (Figure 2. 34). The run-up is estimated to be approximately 30 m. A fahrböschung of 15° was calculated based on an approximate height of 300 m and length of 1000 m for the flowslide path.

The debris covers an approximate area of 150,000 m^2 with an approximate volume of 1,400,000 m^3. The high mobility of the debris is evident from the run-up which occurred on the opposite side of the slope which probably caused a temporary landslide dam, before continuing further downstream.

2.5.9 Peñacocha Rock Slide

The Peñacocha rock slide (Figure 2. 36 and 2. 37) (8° 16' 47" S, 77° 43' 40" W) is located approximately 13 km northeast of the earthquake epicentre within the IX intensity isoseismal (Figure 2. 12). This rock slide is reported by Heim (1949) as being triggered by the 1946 Ancash earthquake. It is located in the vicinity of the Suytucocha rock avalanche (Figure 2. 12).

The source slope is underlain by limestone, shale and calcareous sandstone of the Parihuanca, Chulec and Pariatambo formations (Sanchez Fernandez, 1995) (Figure 2. 7). Heim (1949) also noted large amounts of black peat in the valley bottom, with small holes similar to gaseous eruptions in a basaltic lava flow. These small holes were believed to have occurred due to the vigorous shaking of the ground caused by the earthquake (Heim, 1949).

An average slope angle of 19° and slope dip direction of S 214° W was estimated for the source slope. The Peñacocha rock slide slid on a southwest dipping bedding plane into the valley bottom (Figure 2. 36). A path height of approximately 80 m and a run out of 300 m yielded a fahrböschung of 14°.

The debris of the Peñacocha rock slide covers an approximate area of 100,000 m^2 with an approximate volume of 1,000,000 m^3.

2.5.10 Trucha Rock Avalanche

The Trucha rock avalanche (Figure 2. 38 and 2. 39) was not reported as being triggered by the Ancash earthquake. However, field observations indicate that the rock avalanche occurred within the same time frame as the other reported 1946 landslides. The Trucha rock avalanche (8° 14' 26" S, 77° 46' 13" W) is located approximately 11 km northeast of the epicentre within the IX intensity isoseismal (Figure 2. 12).

The slope is underlain by limestone, dolomite, and calcareous shale of the Jumasha and Celendin formations (Sanchez Fernandez, 1995) (Figure 2. 7).

Field observations indicate that the Trucha rock avalanche is a wedge failure formed by the intersection of west dipping bedding planes and a set of east dipping joints. In addition, nearly-vertical to south dipping joints form the backscarp of the wedge failure (Figure 2. 40). An average slope angle of 38° and slope direction of S 180° was estimated in the source slope area. Striations measured in the scar (Figure 2. 41) indicated that the wedge moved along an approximate orientation of 203° to 224°. The debris was directed out of the slope by the line of intersection and continued downslope into the valley bottom where it followed the valley downstream to the west (Figure 2. 39).

The height of the Trucha rock avalanche path is estimated at 300 m while the run out is 700 m. These measurements yield a fahrböschung of 20°.

The debris covers an approximate area of 100,000 m^2 with an estimated volume of 800,000 m^3 (Table 2. 3).

2.6 Discussion

2.6.1 Topographic and Structural Trends

The structural fabric within the epicentral area exhibits a northwest-southeast trend largely due to the southwest-northeast compression which is occurring between the Nazca and South American plates. Thrust sheets are compressed to the northeast generating layers of southwest dipping bedding planes. Some valleys run perpendicular to the strike of the thrust sheets, transverse to the regional structural fabric.

The majority of landslides inferred to have been triggered by the 1946 Ancash earthquake were rock avalanches which occurred in Cretaceous limestone and shale formations. Some of these landslides initiated as wedge failures which formed along the intersection of southwest dipping bedding planes and orthogonal joint systems and exited the slope along the line of intersection, parallel to the dip direction of the slope.

2.6.2 Landslide Volume vs. Cumulative Frequency

Landslides triggered by individual earthquakes can be compared using total volume of material moved and cumulative frequency. Volume vs. cumulative frequency was plotted for all 45 landslides in the epicentral area of the 1946 Ancash earthquake (Figure 2. 42). The graph shows a higher frequency of the smaller landslides compared to a lower frequency of larger landslides triggered by the earthquake. The detection of smaller landslides near the detection threshold is much less complete since these types of landslides are more difficult to document with certainty in the field. Therefore, the graph displays a rollover effect commonly observed in these studies. A best fit power law was calculated for the data below the rollover point and has an r^2 value of 0.97:

$$\ln(Y) = -0.513 * \ln(X) + 5.55 \qquad \text{[Equation 2. 2]}$$

At higher volumes, the plot shows significant deviations from the best fit power law line (Figure 2. 42). These deviations could be due to the occurrence of volume enhancement due to entrainment following initial failure.

The volume/frequency curve of the 1946 Ancash landslides displays a similar form to other earthquake-triggered landslide volume/frequency curves, such as the 1994 Northridge earthquake (Figure

2. 42) (Harp and Jibson, 1995). A best fit power law was calculated for the Northridge data below the rollover point and has an r^2 value of 0.98 (Harp and Jibson, 1995):

$$\ln(Y) = -0.804 * \ln(X) + 4.68 \quad \text{[Equation 2. 3]}$$

The 1946 Ancash earthquake has a similar best fit line to the 1994 Northridge earthquake although the slope is steeper for the latter data set. However, the 1946 earthquake volume/frequency curve is situated much further to the right of the 1994 Northridge earthquake curve, indicating higher landslide volumes occurred during the 1946 Ancash earthquake. The slightly flatter slope of the 1946 Ancash earthquake data also indicates that larger failures are much more frequent than those associated with the 1994 Northridge earthquake. Higher landslide volumes and frequency can largely be attributed to the higher magnitude of the Ancash earthquake which was recorded at 7.3 compared to a magnitude of 6.7 for the Northridge earthquake (Harp and Jibson, 1995).

2.6.3 Total Landslide Volume vs. Earthquake Magnitude

The total volume of landslides triggered by the 1946 Ancash earthquake was examined in relation to earthquake magnitude. Empirical correlations have been derived between the total volume of landslides triggered by an earthquake (V_{LT}) and the earthquake's moment magnitude (*M*) (Keefer, 1994; Malamud et al., 2004). Keefer (1994) originally considered the total volume of landslide material generated by 15 historical earthquakes and Malamud et al. (2004) added the total landslide volume obtained for the 1994 Northridge earthquake. Although a wide range of geological, geophysical and climatic conditions are associated with these earthquake-triggered landslide events, a relatively good power law dependence of the total landslide volume (V_{LT}) on earthquake moment magnitude (*M*) was obtained (Malamud et al., 2004). As a result, the best fit exponential line of the data gives (Malamud et al., 2004):

$$\ln(Y) = 3.27 * X - 25.9 \quad \text{[Equation 2. 4]}$$

The total landslide volume, V_{LT}, and earthquake moment magnitude, *M*, data from Malamud et al. (2004) and Keefer (1994) are plotted (Figure 2. 43). Data for the 1946 Ancash earthquake is added to the plot (Figure 2. 43). The total landslide volume (V_{LT}) of 0.093 km^3 for the 1946 Ancash earthquake was obtained by summing the volumes of all 45 landslides inferred to have occurred within the epicentral area and the earthquake moment magnitude (*M*) of 7.0 ± 0.1 for the 1946 Ancash earthquake was obtained from Bellier et al. (1991). The 1946 Ancash earthquake data clearly plots within the standard deviations of the fit (Figure 2. 43).

2.6.4 Denudation and Denudation Rate

Denudation and denudation rates are important in determining the effects of earthquake-triggered mass movements on the landscape. Denudation (D) for an area can be calculated by dividing the total landslide volume (V_{LT}) (km^3) by the area over which the landslides are concentrated (A_R) (km^2). Denudation for the 1946 Ancash earthquake was calculated by dividing the total estimated landslide volume by the area over which the landslides are concentrated represented by the VIII intensity isoseismal.

$D = V_{LT} / A_R$ [Equation 2. 5]

$D = 9.3E\text{-}02\ km^3 / 1216\ km^2$

$D = 7.6E\text{-}05$ km

$D = 76$ mm

An average surface lowering of 76 mm thus occurred within the VIII intensity isoseismal for the 1946 Ancash earthquake.

In addition, denudation rates (km/yr) based on landslide event inventories can be calculated by the following equation (Malamud et al., 2004):

$h = V_{LT} / (A_R * T_L)$ [Equation 2. 6]

Where h is equal to the denudation rate (km/yr), V_{LT} is the total landslide volume (km^3) and A_R is the area over which the landslides are concentrated (km^2) (Malamud et al., 2004). For landslide event inventories a trigger is repeated at regular intervals, therefore T_L is the recurrence interval for landslide-inducing earthquakes (years) (Malamud et al., 2004). The denudation rate based on the 1946 Ancash earthquake was calculated, where V_{LT} was estimated by summing the volumes of all 45 landslides occurring in the epicentral area, A_R was calculated based on the area of the VIII intensity isoseismal within which all the 1946 inferred landslides were located, and T_L was calculated based on the recurrence interval of the 1946 Ancash earthquake which was noted above as 13,000 years.

The denudation rate based on the 1946 Ancash earthquake was calculated as follows:

$h = V_{LT} / (A_R * T_L)$ [Equation 2. 6]

$h = 9.3E\text{-}02\ km^3 / (1216\ km^2 * 13{,}000$ years)

$h = 5.85E\text{-}09$ km/yr

$h = 5.85E\text{-}03$ mm/yr

The denudation rate for the 1946 Ancash earthquake is thus estimated as being 0.00585 mm/yr. This denudation rate may be compared to other denudation rates associated with landslide-inducing earthquakes, such as the 1994 Northridge earthquake which had a denudation rate of 0.1 mm/yr (Malamud et al., 2004). The 1946 Ancash earthquake denudation rate is less than that of the 1994 Northridge earthquake due to a very long recurrence interval associated with the triggering event.

2.7 Conclusions

The 1946 Ancash earthquake caused macroseismic effects throughout the epicentral area, including damage to villages, surface faulting and numerous landslides. The epicentral area of the 1946 event straddles the continental divide where there is strong evidence of eastward compression due to the subduction of the Nazca plate beneath the South American plate. Due to this compression, the structural fabric in the area shows major northwest-southeast trends. Specifically, thrusts sheets have formed creating successive layers of southwest dipping bedding planes striking northwest-southeast. Valleys within the epicentral area are both parallel and transverse to this dominant northwest-southeast trend.

Topographic amplification of ground shaking may have contributed to the large number of landslides which were inferred to have occurred during the 1946 Ancash earthquake. A large percentage of these landslides are rock avalanches, some of which occurred as wedge failures. Wedge failures were formed by the intersection of southwest dipping bedding planes and a set of east dipping joint sets and occurred in valleys that run transverse to the structural trend.

The landslide inventory compiled for the 1946 Ancash earthquake enabled a best estimate of 0.093 km^3 for the total volume of material moved during the earthquake. Comparisons between the 1946 Ancash earthquake landslide volumes and other earthquake-triggered landslide volumes yielded similar results relative to cumulative frequency and earthquake magnitude. In addition, an average surface lowering of 76 mm was estimated to have occurred over the epicentral area and a denudation rate of 0.00585 mm/yr due to earthquake-triggered landsliding in the epicentral area was estimated.

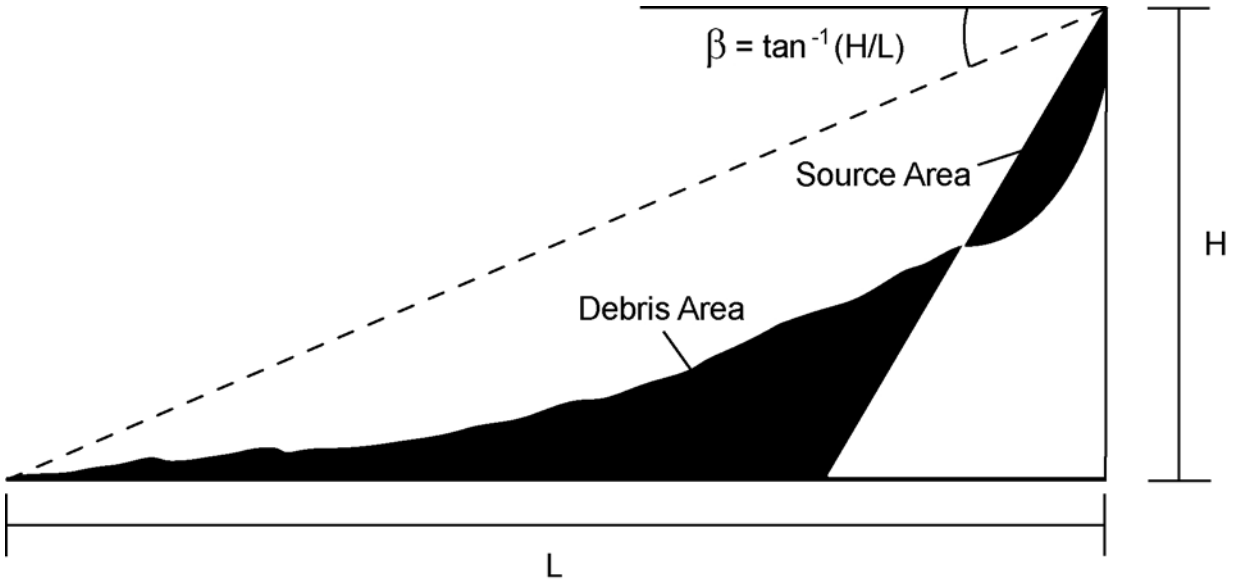

Figure 2. 1: Schematic diagram showing fahrböschung (β) in relation to height (H) and length (L) of landslide path

(S.G. Evans, Personal Communication, 2007)

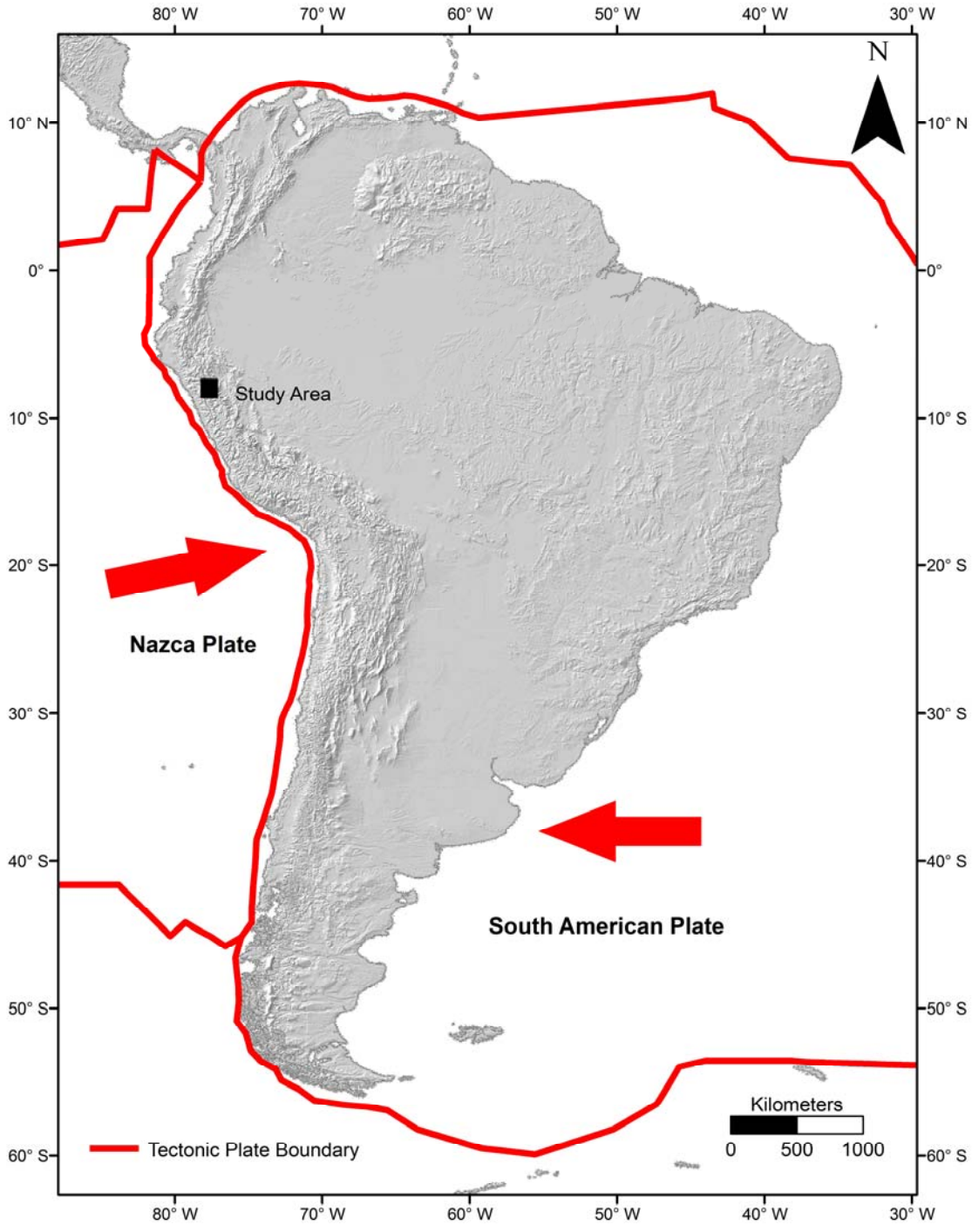

Figure 2. 2: Shaded relief map of South America showing the subduction of the Nazca plate under the South American plate at the location of the study area

Tectonic plate boundaries (ESRI Canada Schools and Libraries Program, 2005) are shown in red. Red arrows indicate direction of plate movement. Black square indicates study area of the 1946 Ancash earthquake.

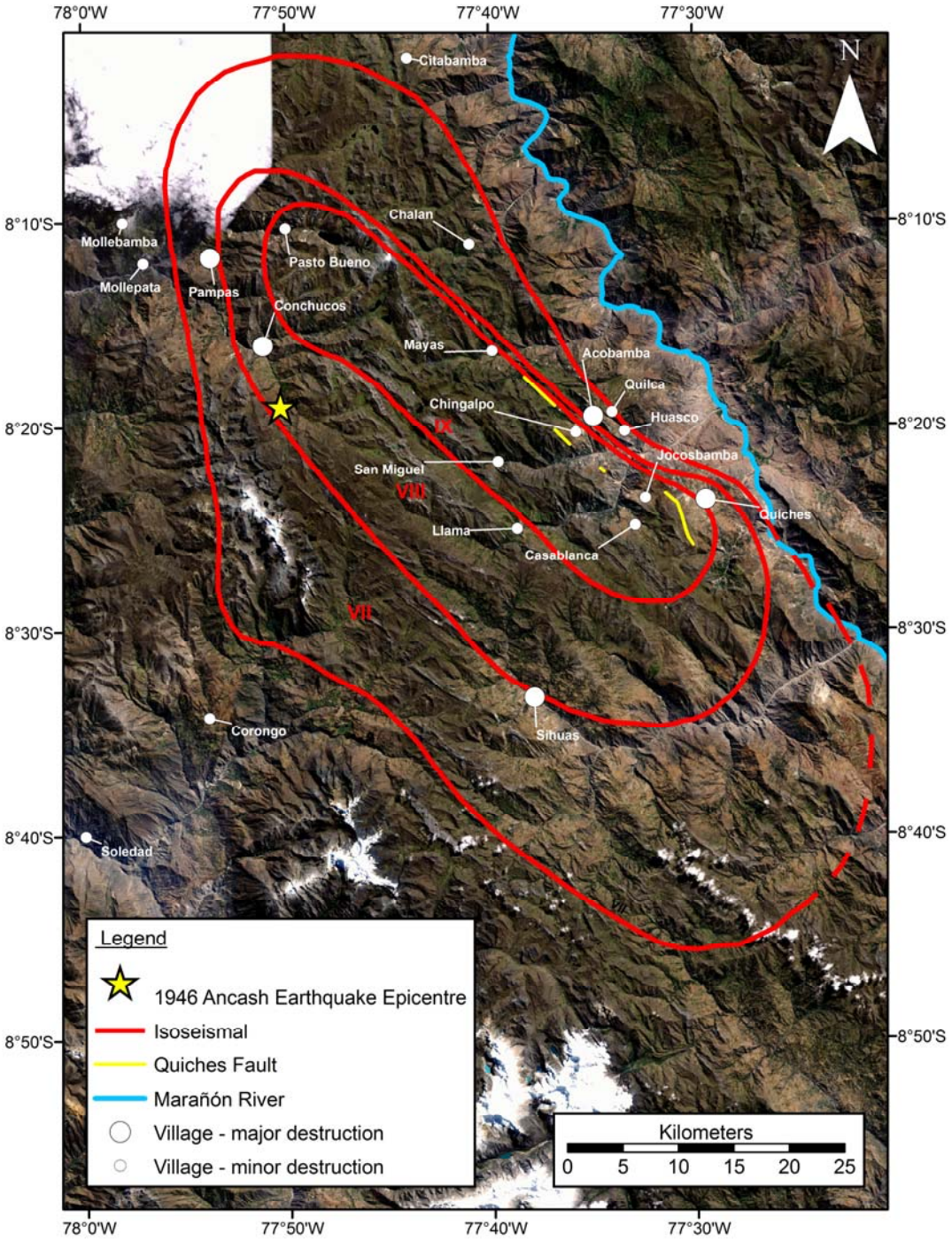

Figure 2. 3: Epicentral area of the 1946 Ancash earthquake

Landsat 7 ETM+ showing 1946 M7.3 Ancash earthquake epicenter and isoseismal intensities (Silgado, 1951). The Quiches fault is shown in yellow (Bellier et al., 1991). The Marañón River is the main river valley in the region. Villages with major and minor destruction (Silgado, 1947; Silgado, 1951) are also indicated by scaled white circles.

Figure 2. 4: The present day setting (2008) of the villages Pampas (A) and Conchucos (B)

Both villages are located within the epicentral area of the 1946 Ancash earthquake and were more or less destroyed during the earthquake.

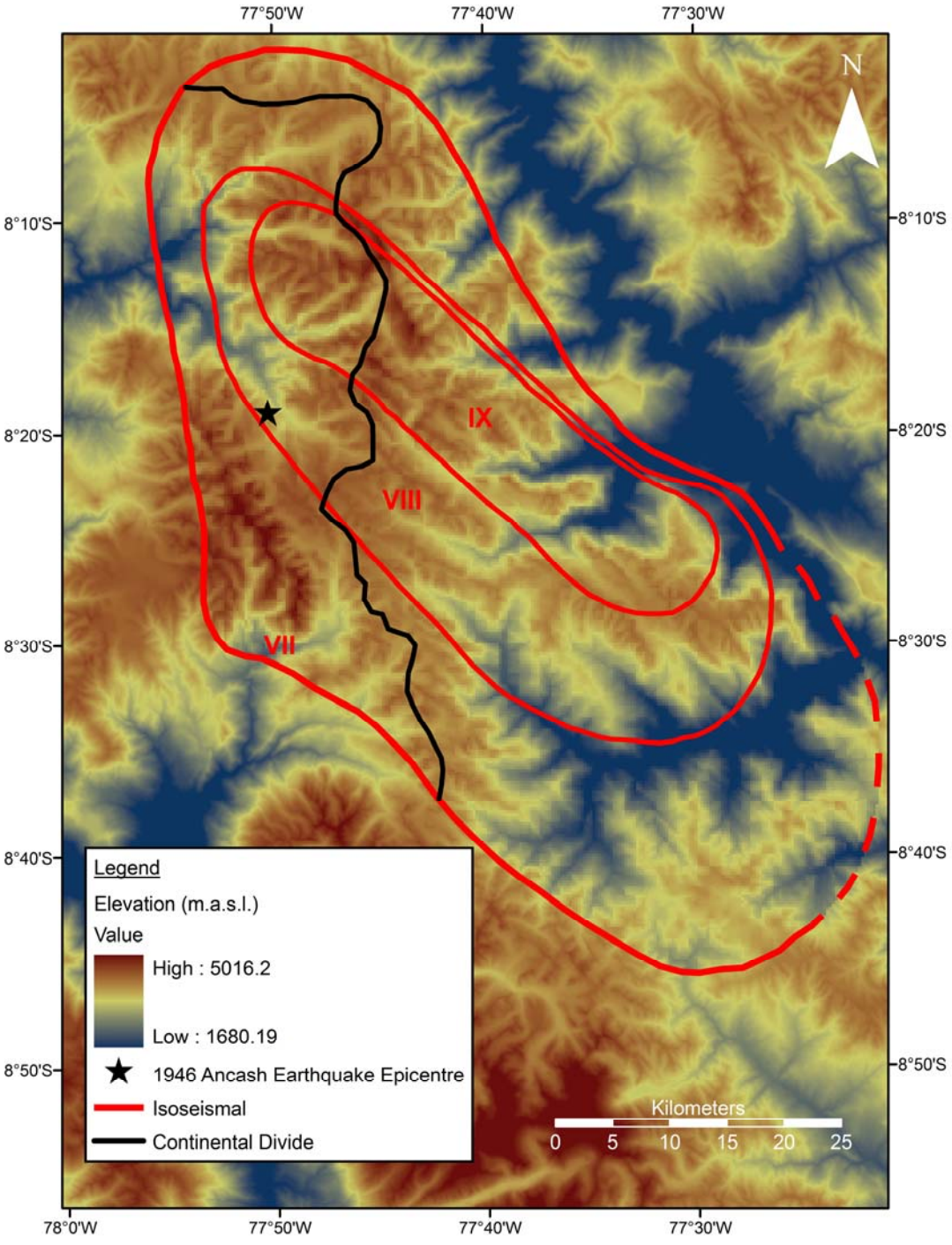

Figure 2. 5: Digital elevation model (DEM) showing the peaks and valleys of the epicentral area

The 1946 Ancash earthquake epicentre and intensity isoseismals (Silgado, 1951) are shown. The continental divide between the Pacific and Atlantic is shown in black.

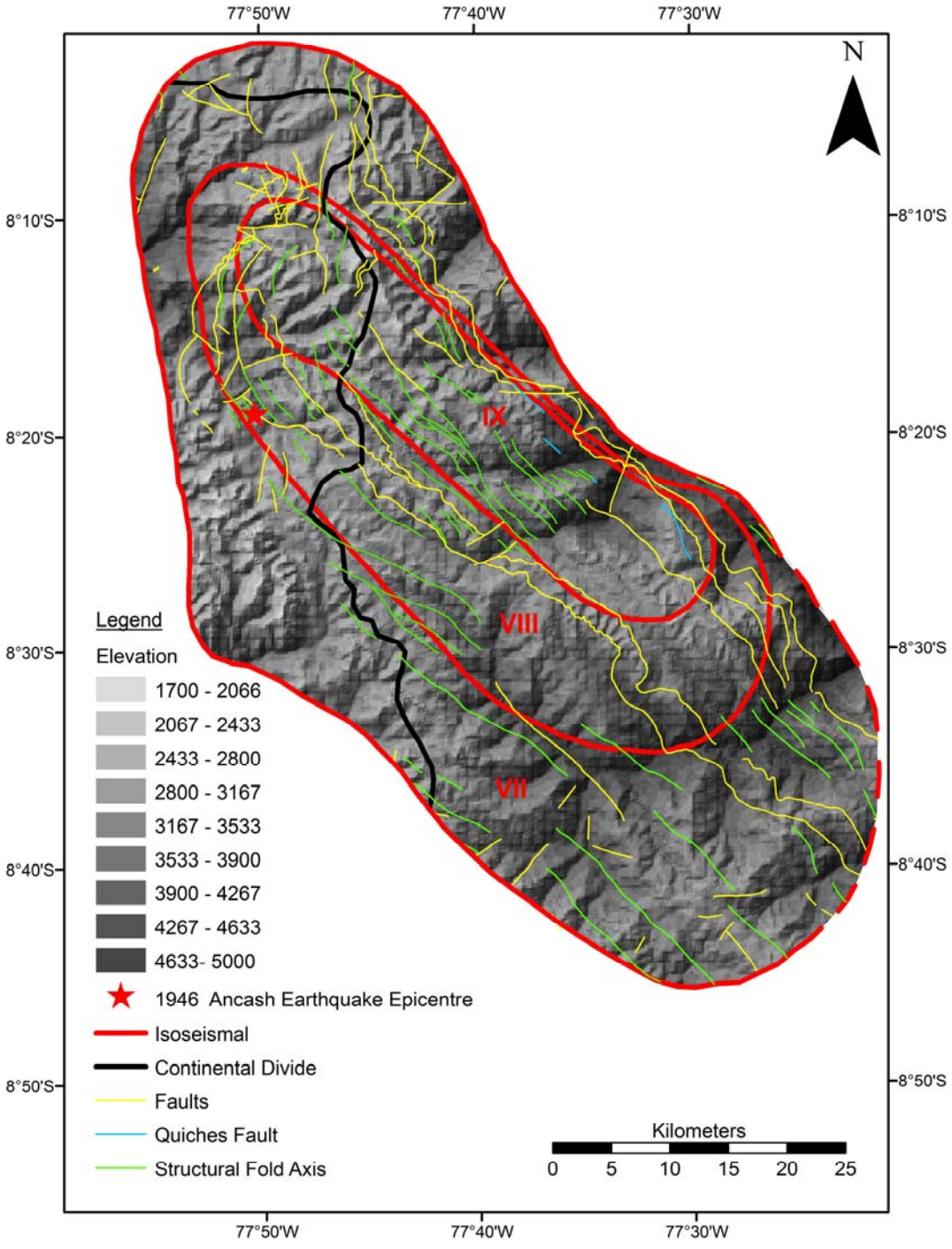

Figure 2. 6: Triangulated Irregular Network (TIN) showing elevations within the epicentral area

The 1946 Ancash earthquake epicentre and isoseismal intensities are shown in red (Silgado, 1951) as well as the continental divide in black. Faults (yellow) (Sanchez Fernandez, 1995) including the Quiches fault (blue) (Bellier et al., 1991) and structural fold axes (green) (Sanchez Fernandez, 1995) are also shown.

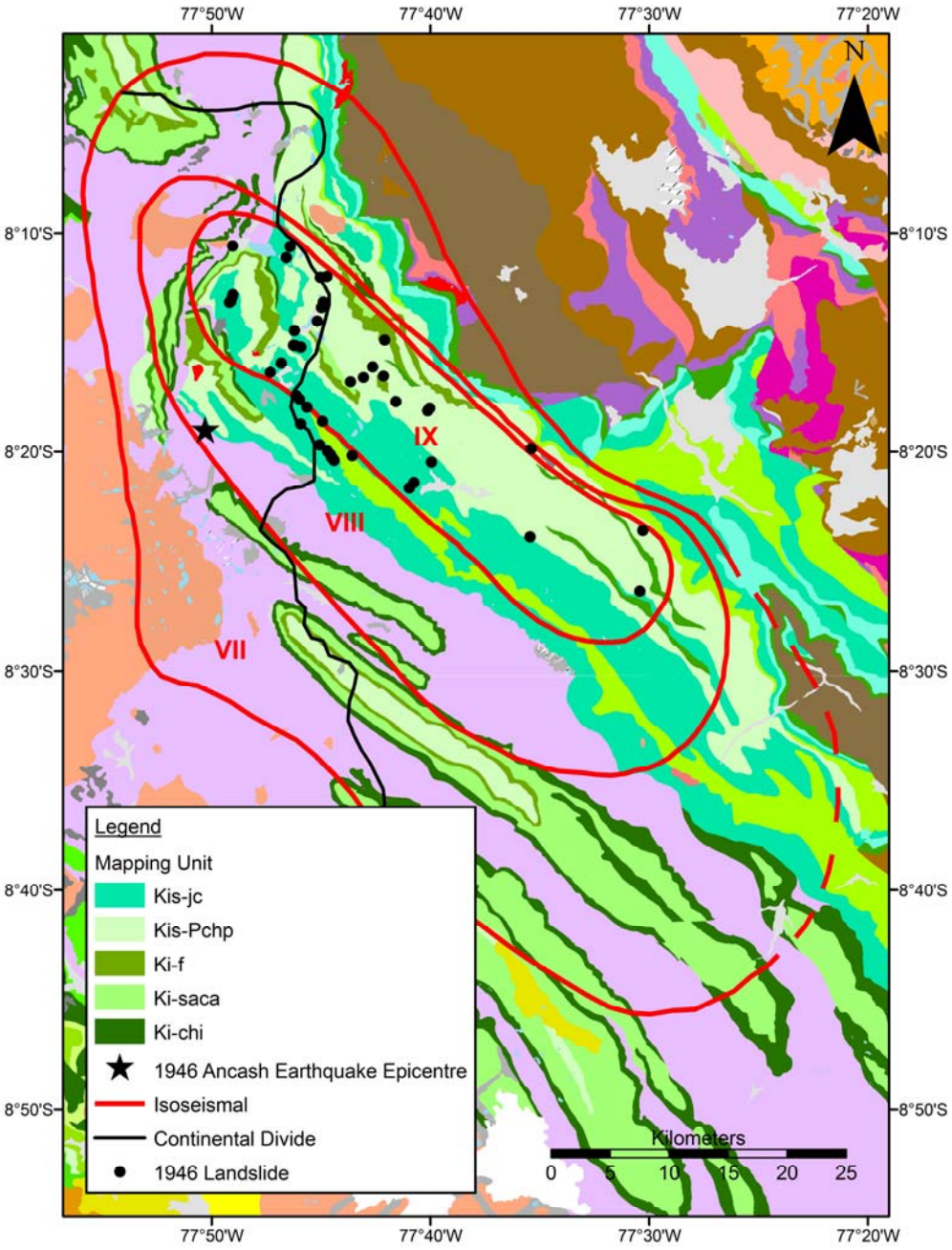

Figure 2. 7: Geology of the epicentral area showing the five mapping units within which landslides triggered by the 1946 Ancash earthquake occurred

Geology of the epicentral area (Sanchez Fernandez, 1995). Key to mapping units is in Figure 2. 8. The 1946 Ancash earthquake epicentre and isoseismal intensities (Silgado, 1951) are shown as well as the continental divide. Landslides inferred to have occurred during the 1946 Ancash earthquake are shown as black dots.

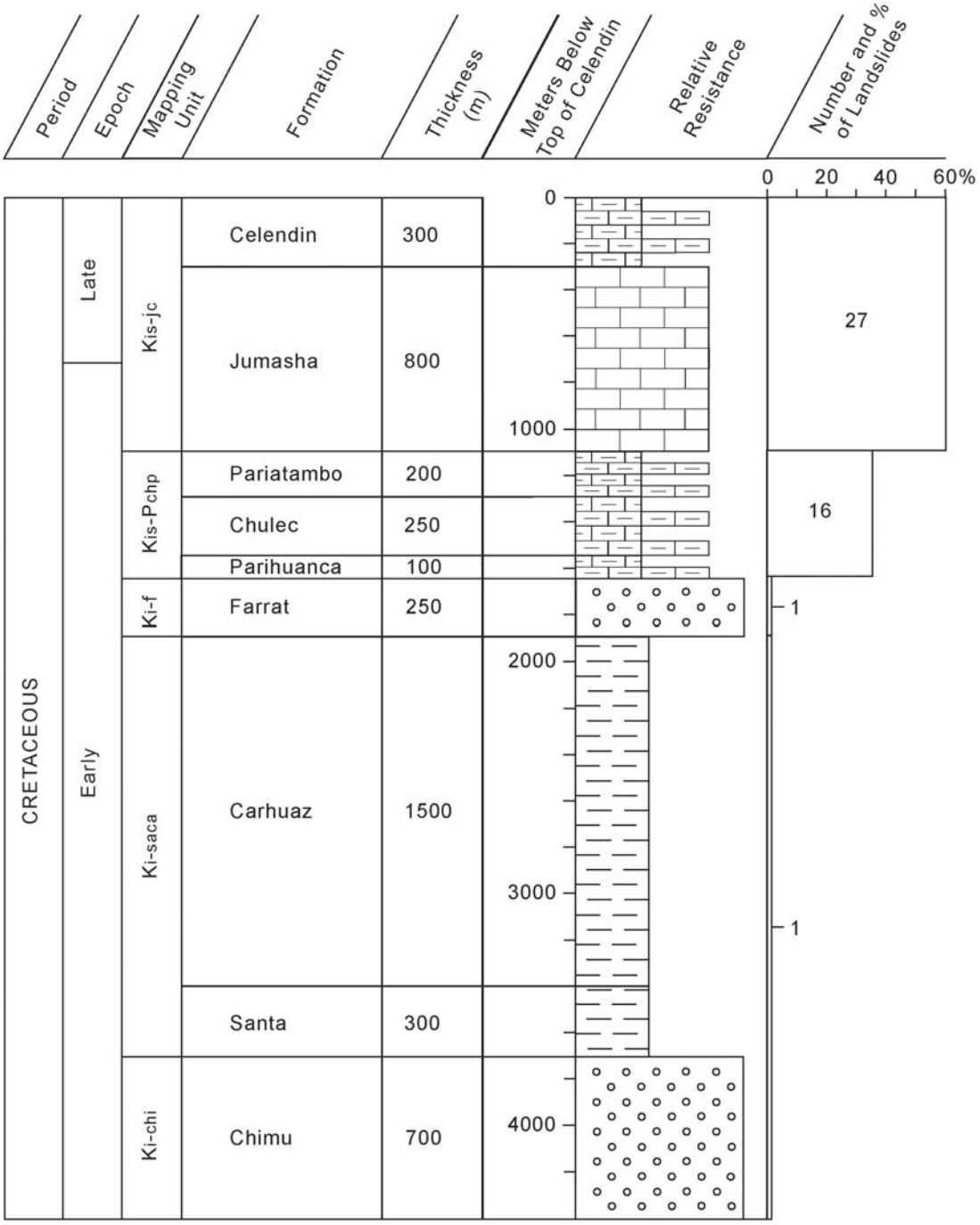

Figure 2. 8: A regional stratigraphical column of the five mapping units within which landslides occurred in the epicentral area of the 1946 Ancash earthquake

Stratigraphy based on Benavides-Cáceres (1956), Wilson (1963) and Cobbing et al. (1981). Period, epoch, mapping unit (Sanchez Fernandez, 1995), formation, thickness (m), meters below top of Celendin Formation, relative resistance (based on field exposures and the number and % of landslides which occurred within each unit are shown. Data on landslides abstracted from Table 2. 3.

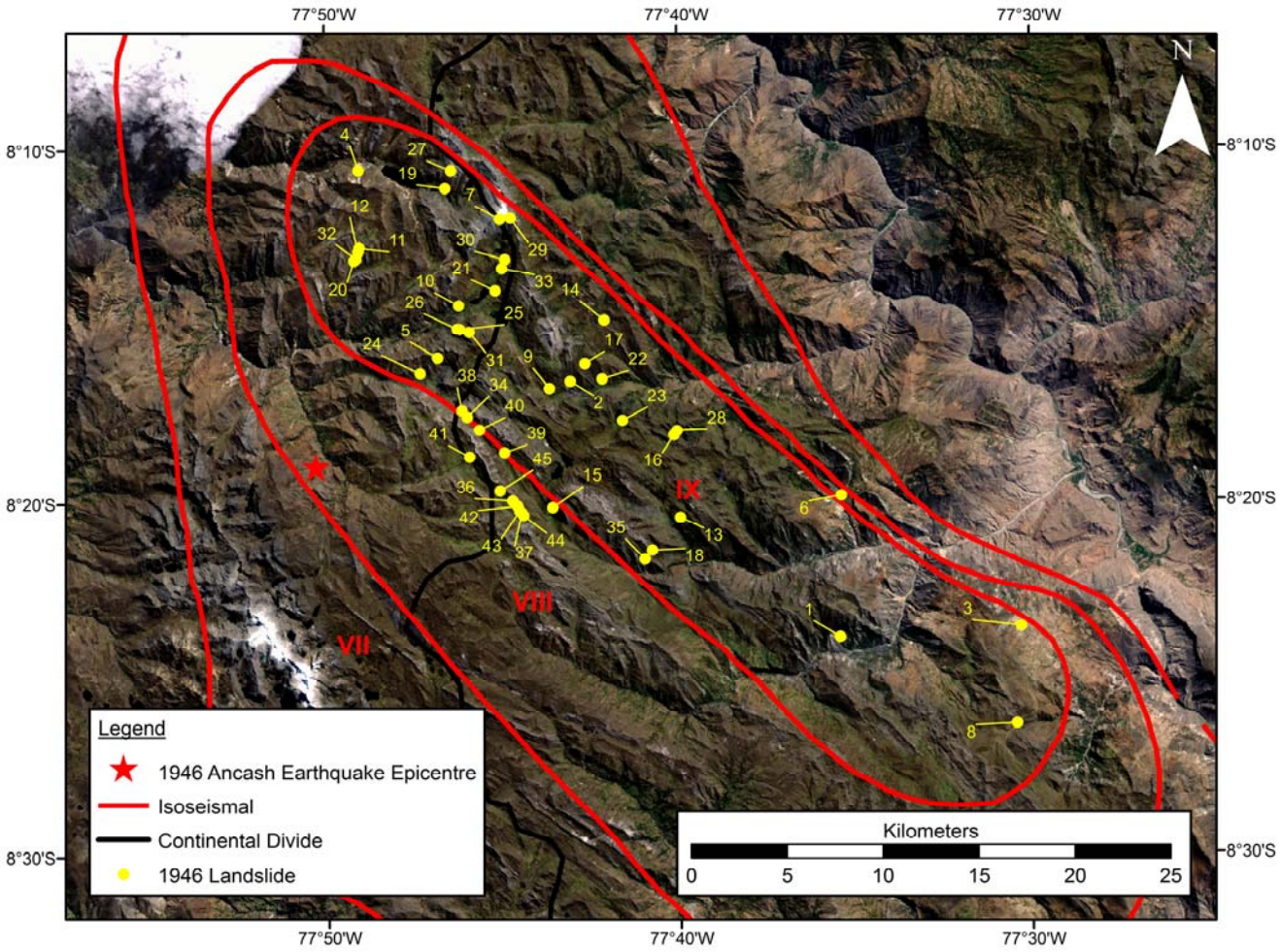

Figure 2. 9: Distribution map of landslides inferred to have been triggered by the 1946 Ancash earthquake

Landsat 7 ETM+ showing 1946 Ancash earthquake epicentre and isoseismal intensities (Silgado, 1951) as well as the continental divide. Number label of landslide corresponds to Table 2. 3.

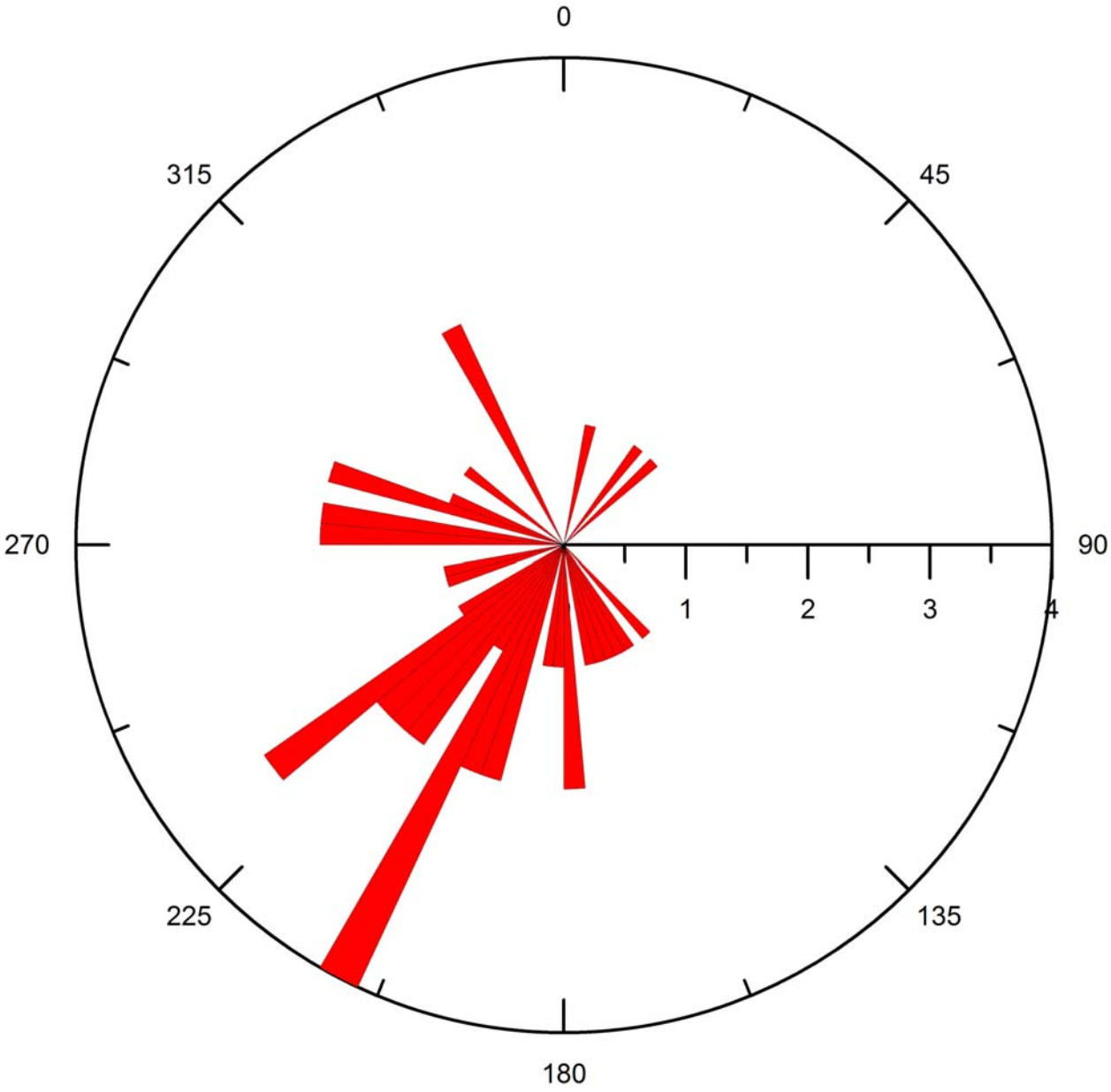

Figure 2. 10: Rosette plot showing the source topographic slope dip direction for all 45 landslides which occurred within the epicentral area of the 1946 Ancash earthquake

A dominant southwest dip direction is evident.

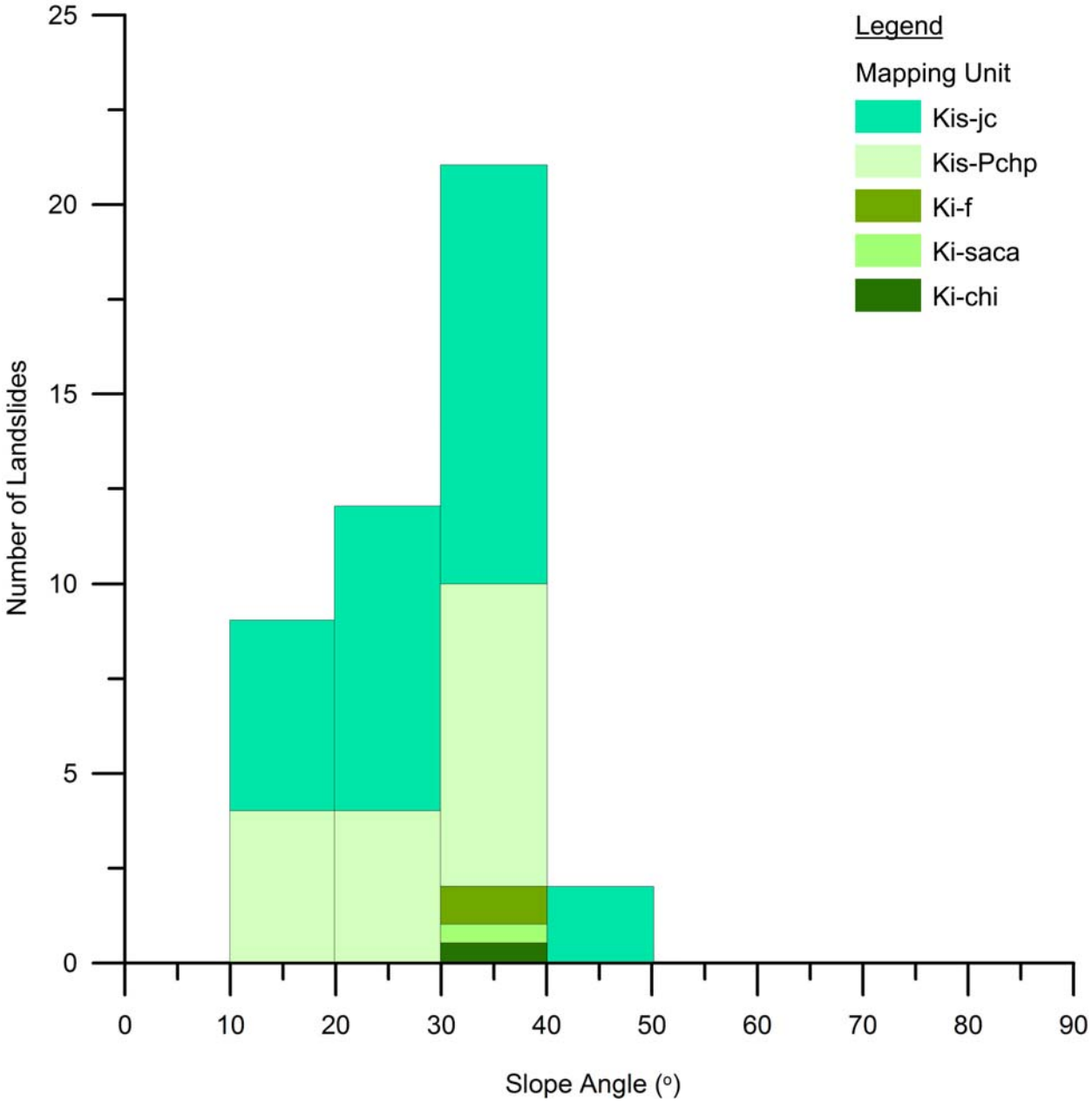

Figure 2. 11: Histogram showing the distribution of source slope angles in 10˚bins for all 45 landslides which occurred within the epicentral area of the 1946 Ancash earthquake

Mapping unit distribution is also shown within the source slope angle bins. Key to mapping units is in Figure 2. 8.

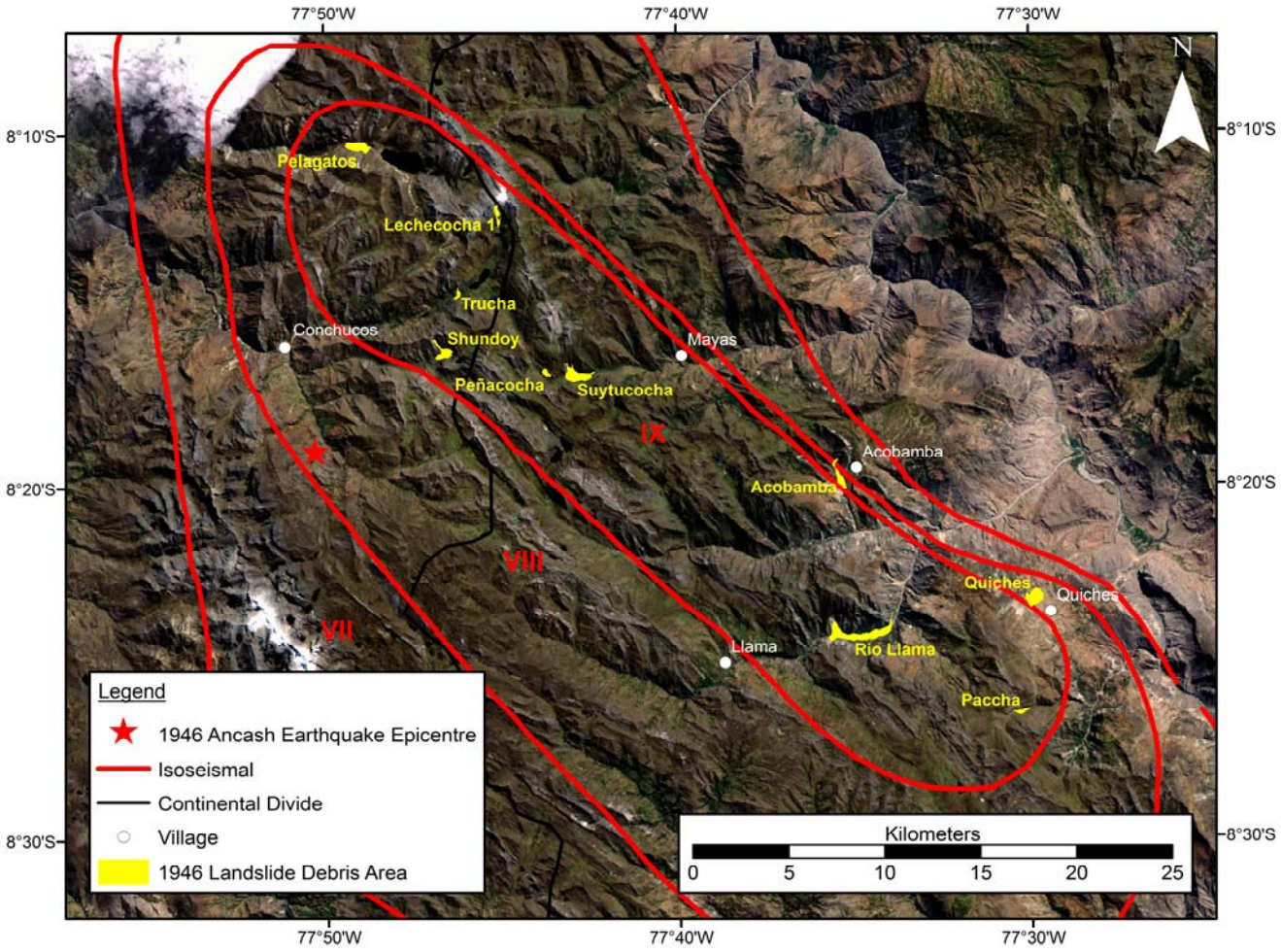

Figure 2. 12: Landslide debris areas for the ten largest landslides triggered by the 1946 Ancash earthquake

Landsat 7 ETM+ showing earthquake epicentre and isoseismal intensities (Silgado, 1951). Continental divide is shown along with selected villages within the epicentral area.

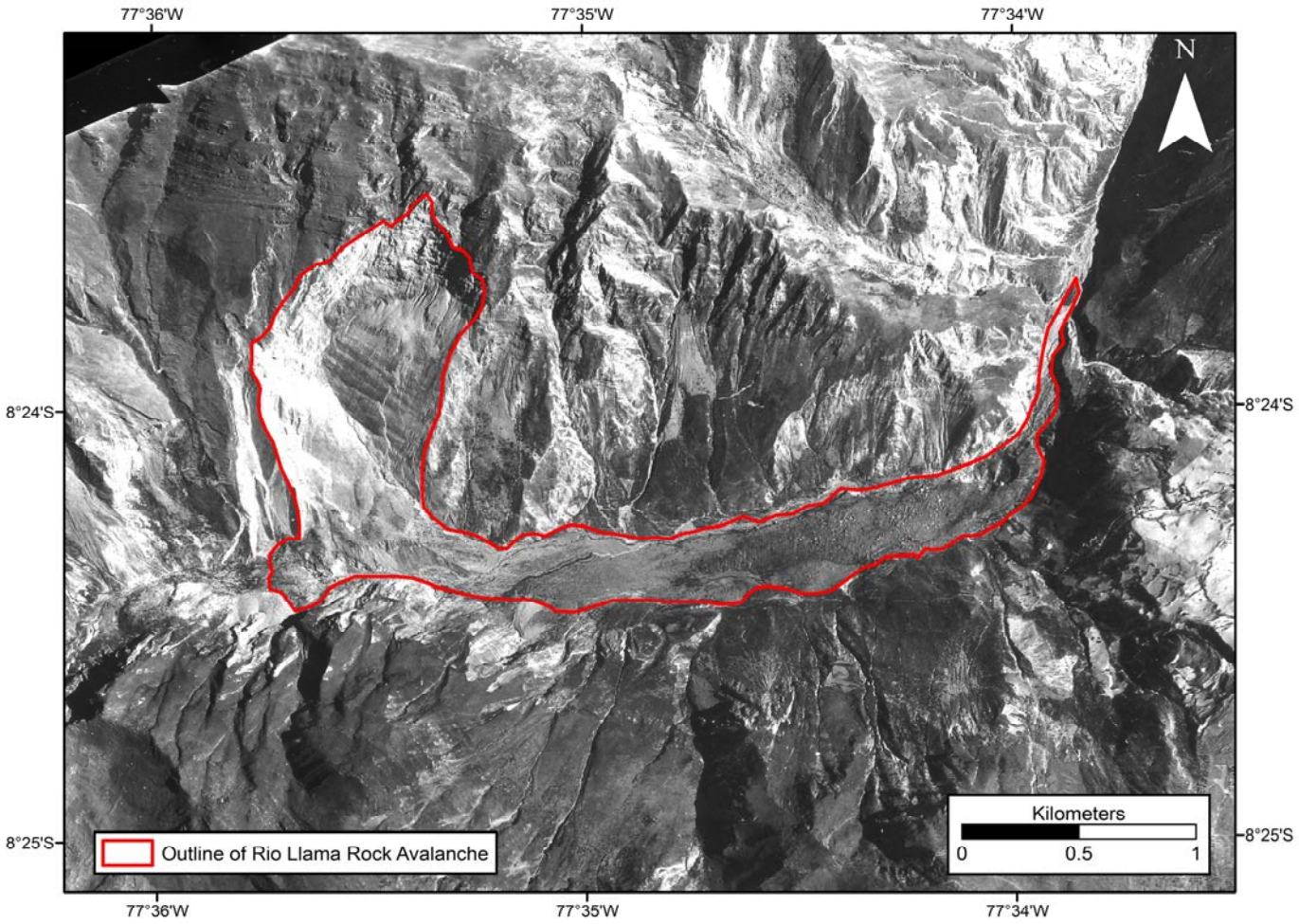

Figure 2. 13: Aerial photograph (1370PMW-M255-31448) showing the Rio Llama rock avalanche

Failure initiated on a southwest dipping bedding plane and was directed south by topography until it reached the valley bottom where it flowed downstream to the east.

Figure 2. 14: The Rio Llama rock avalanche, looking west

Partial view of the southwest dipping bedding planes in the source area of the Rio Llama rock avalanche on the slope to the right. Debris from the Rio Llama rock avalanche covers the valley bottom (foreground).

Figure 2. 15: The Suytucocha rock avalanche, looking north

The Suytucocha rock avalanche is a wedge failure formed by the intersection of a set of southwest dipping bedding planes shown on the right and a set of east dipping discontinuities shown on the left. A nearly-vertical southeast dipping set of discontinuities forming the backscarp is also evident near the top of the source slope.

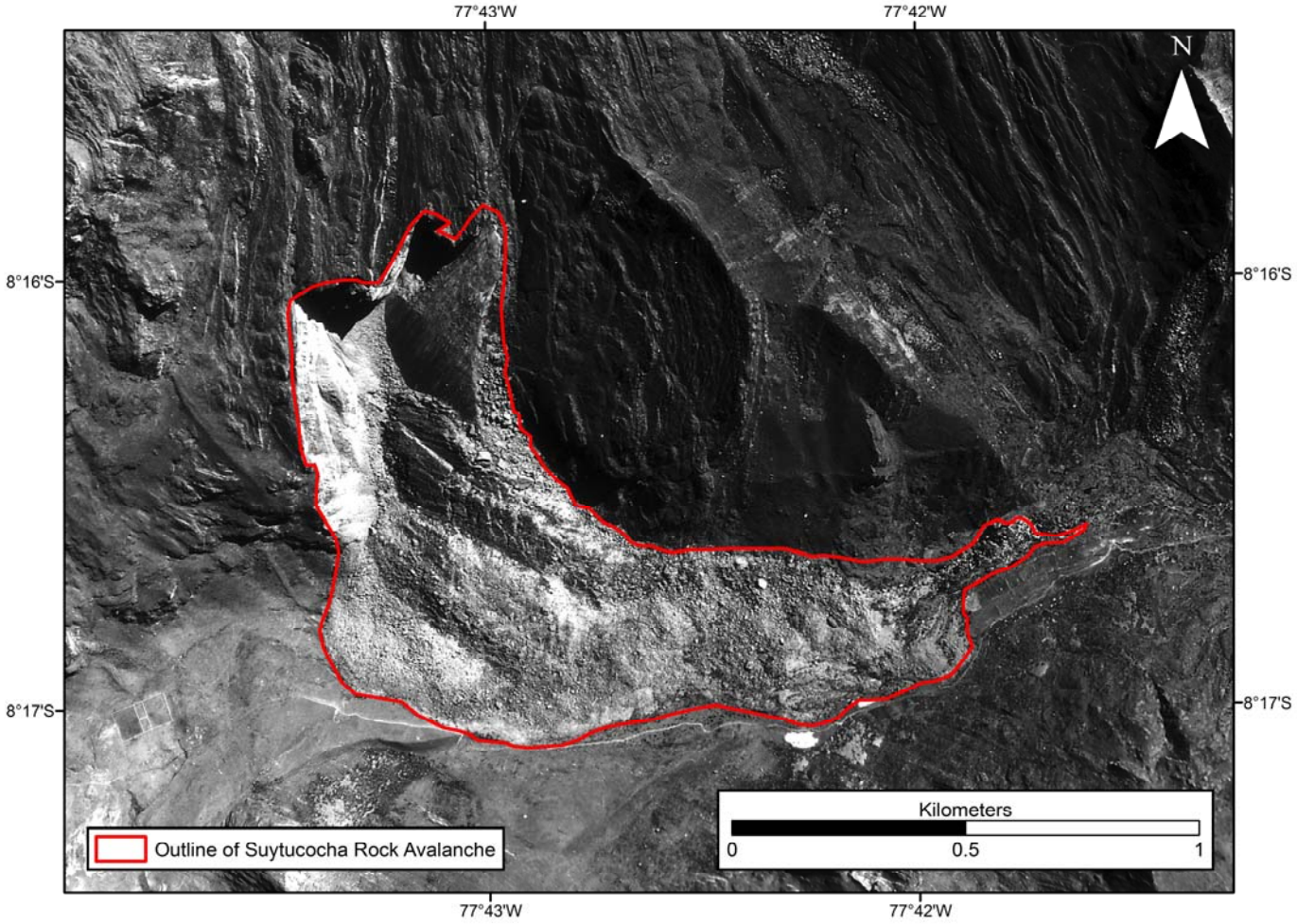

Figure 2. 16: Aerial photograph (1370PMW-M130-16416) of the Suytucocha rock avalanche

Wedge failure involves a southwest dipping bedding plane before descent in a southerly direction to the valley bottom due to the line of intersection. Debris is re-directed in the valley bottom downstream to the east.

Figure 2. 17: View of the Suytucocha rock avalanche looking northeast

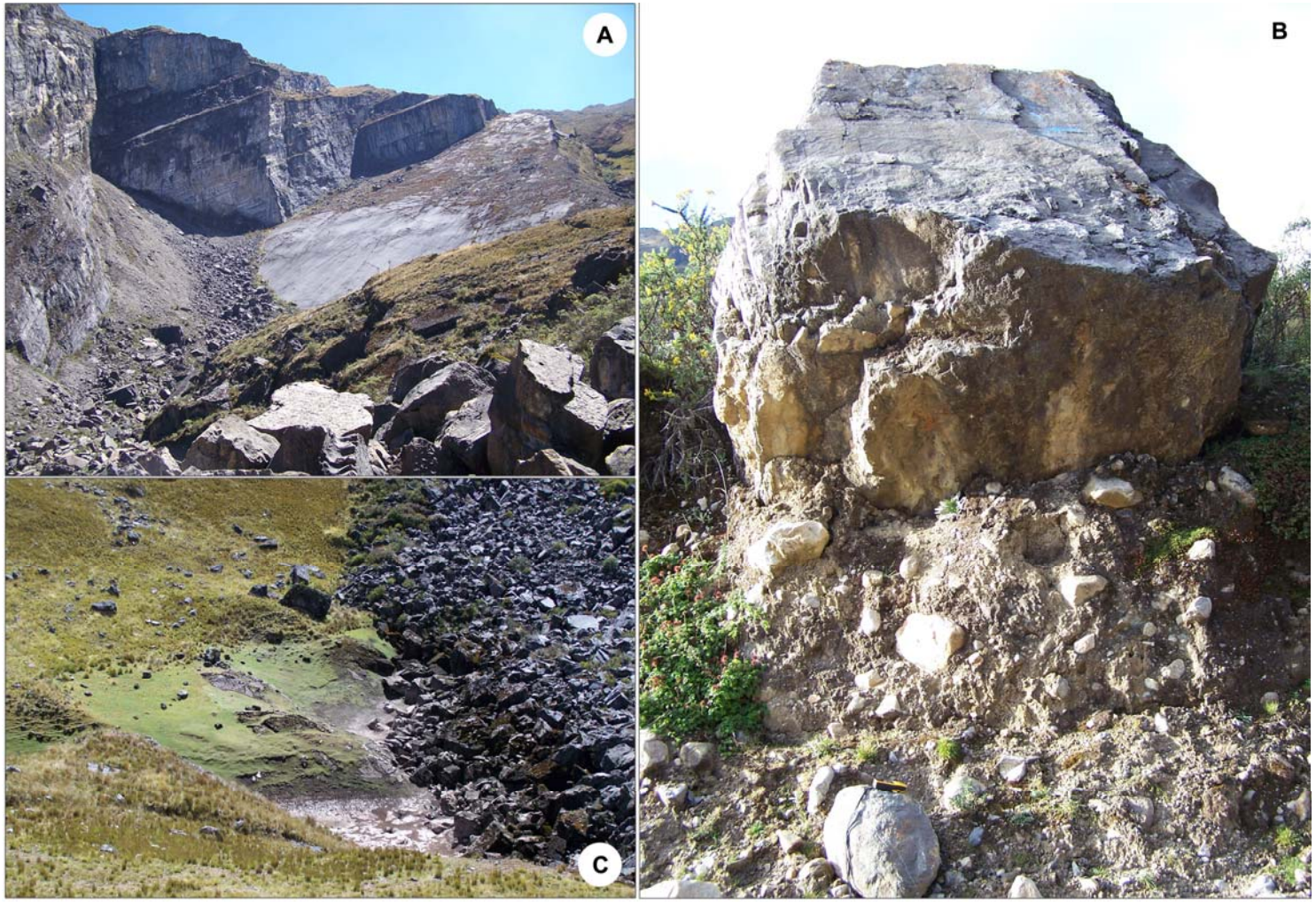

Figure 2. 18: Field observations at Suytucocha rock avalanche

A - Large amounts of land surface were preserved throughout the debris. B - A large boulder is shown overlying finer valley bottom sediments probably due to secondary movement. C - Evidence of a former lake/pond on the upstream boundary of the debris in the valley bottom.

Figure 2. 19: View of Quiches debris avalanche looking northwest taken by Heim (1949)

Reproduced after foto Lám. VI. in Heim (1949, p. 32).

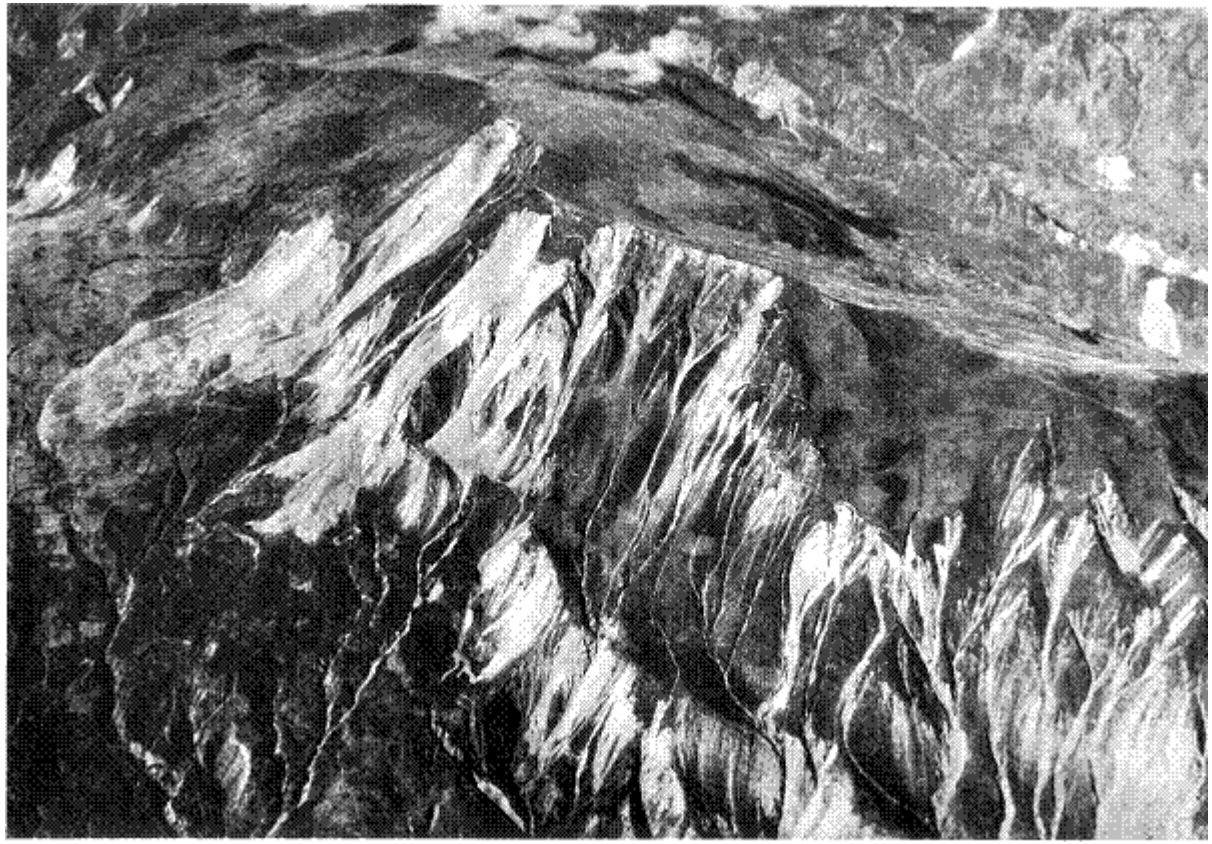

Figure 2. 20: Oblique aerial photograph of Quiches debris avalanche and other earthquake-triggered failures along the same slope taken by Heim (1948) in September 1947

Reproduced after Fig. 42 in Heim (1948). View is to the south**.**

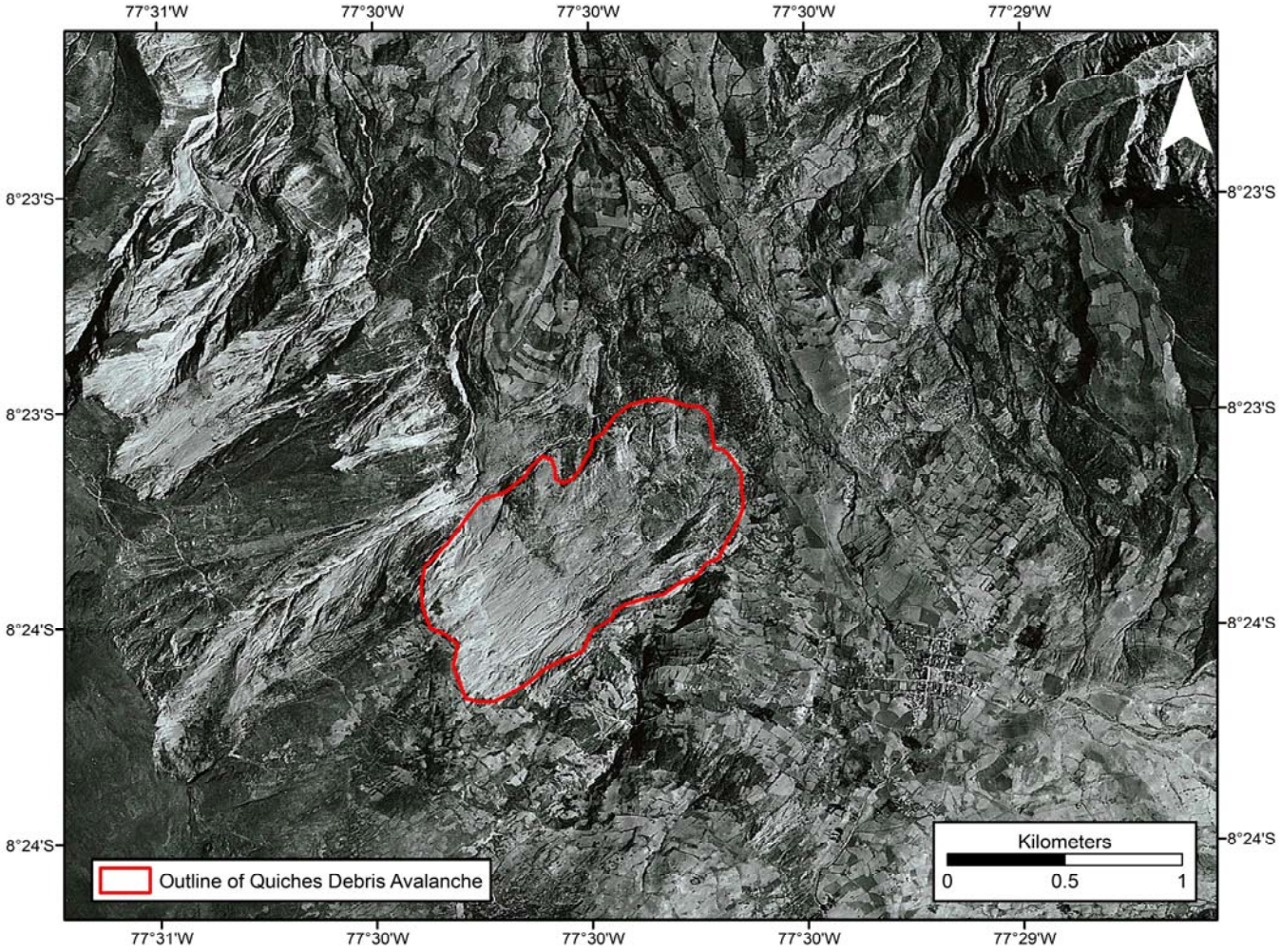

Figure 2. 21: Aerial photograph (PMW1370-M283-34781) of the Quiches debris avalanche

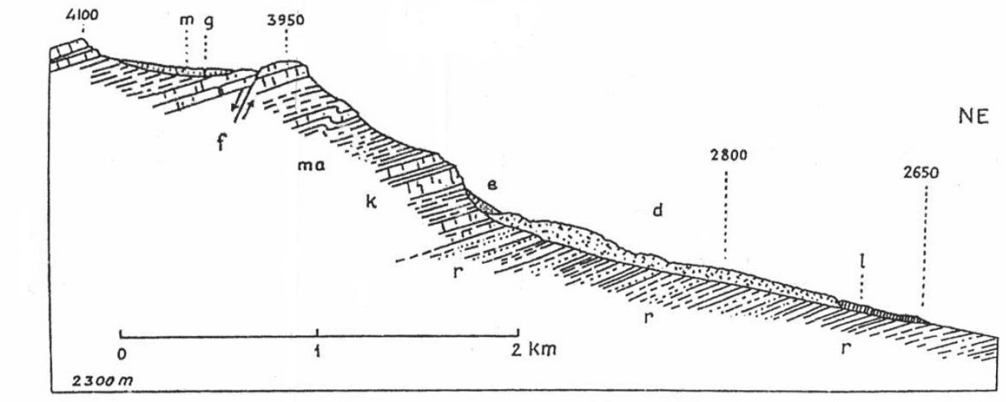

Figure 2. 22: Profile of Quiches debris avalanche reproduced from Fig. 2 Heim (1949, p.13)

k–Cretaceous limestone, ma–marls, r–Red Beds, m–moraines, e–rubble, d–collapse, l–mud current with stones, f–active fault, g–cracks

Figure 2. 23: The Pelagatos rock avalanche, looking south

Showing the debris which slid downslope to created a landslide dam in the valley bottom forming a number of ponds.

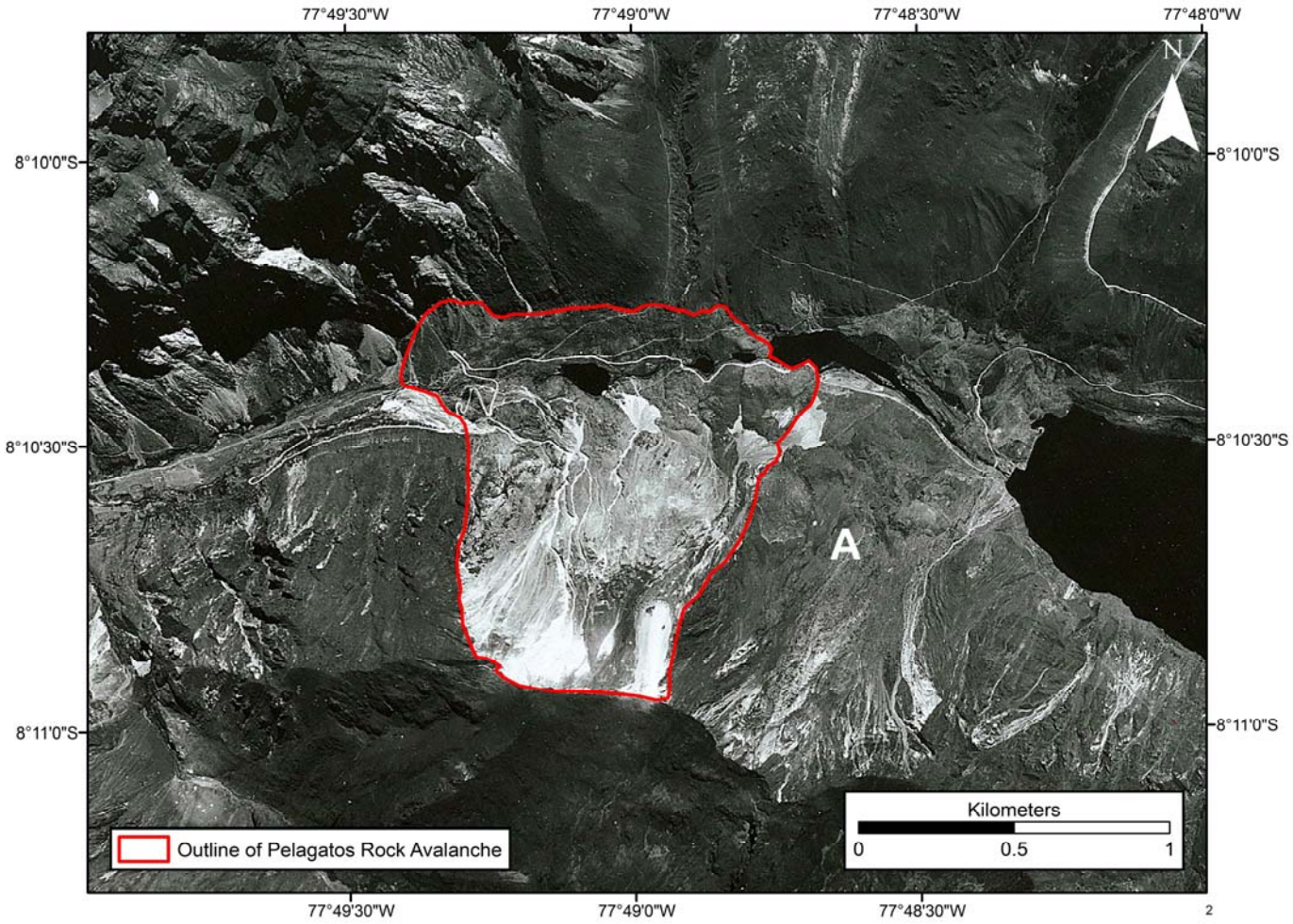

Figure 2. 24: Aerial photograph (1370PMW-M156-20024) of the Pelagatos rock avalanche

Extent of the failure is shown as well as the landslide dam which created a number of ponds in the valley bottom. Prehistoric landslide (A) referred to in text.

Figure 2. 25: Field observations of the Pelagatos rock avalanche debris

A - Debris of blocks within a finer matrix. B - Highly metamorphosed rocks within the debris**.**

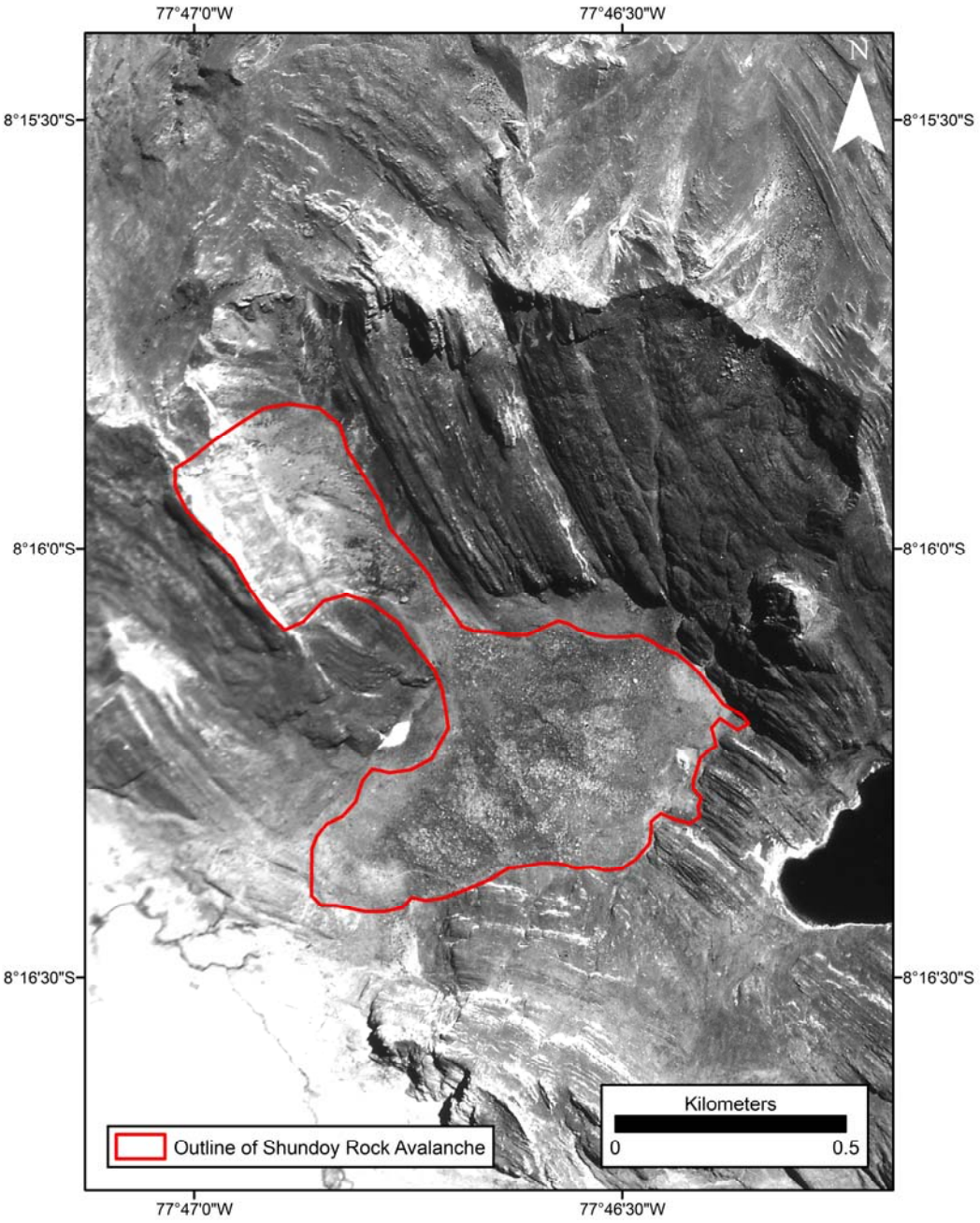

Figure 2. 26: Aerial photograph (1370PMW-M156-20027) of the Shundoy rock avalanche

Initial failure of the Shundoy rock avalanche occurred on northeast dipping bedding planes and debris diverted to the southeast by topography.

Figure 2. 27: The Acobamba rock/debris avalanche, looking north

View of the Acobamba rock/debris avalanche from the distal limit of debris showing location of initial failure at the top right which travelled down the valley covering the village of Acobamba in foreground.

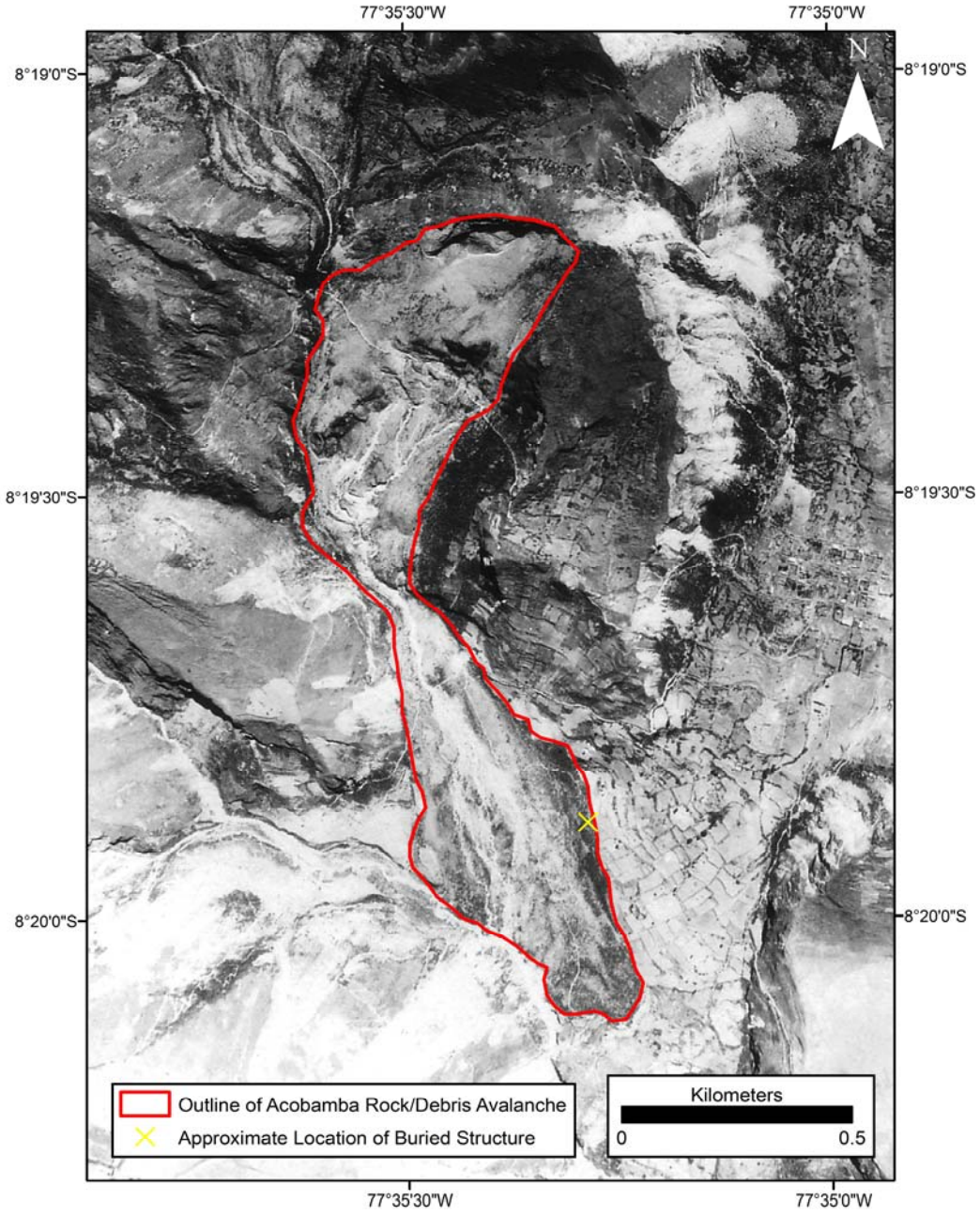

Figure 2. 28: Aerial photograph (1370PMW-M173-22501) of the Acobamba rock/debris avalanche

Location of the buried structure found along the eastern boundary of the debris is denoted by the yellow cross.

Figure 2. 29: Dwelling/structure of Acobamba village found buried within the rock/debris avalanche debris along the eastern boundary

Figure 2. 30: Debris at the Acobamba rock/debris avalanche

A - Photo of debris from the Acobamba rock/debris avalanche showing large boulders within a finer matrix. B - Photograph taken on-site at the Acobamba rock/debris avalanche in 1946 showing debris consisting of large boulders within a finer matrix. Reproduced from Silgado (1947).

Figure 2. 31: The Lechecocha 1 rock avalanche, looking north

The rock avalanche initiated as a wedge failure in Cretaceous limestone formed by the intersection of southwest dipping bedding planes and a nearly-vertical northeast dipping joint set. The ridge forms the continental divide between the Atlantic (Amazon) and the Pacific.

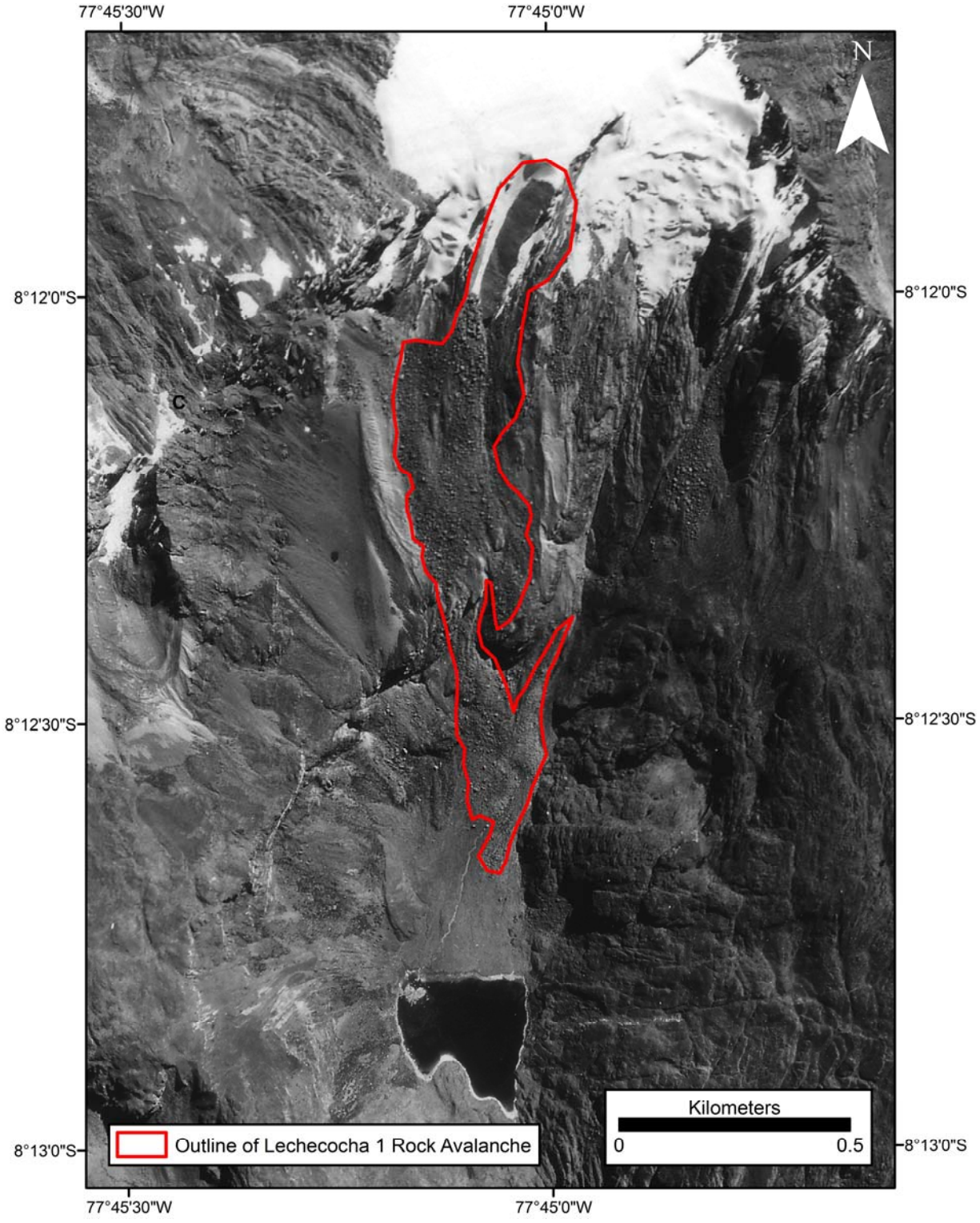

Figure 2. 32: Aerial photograph (1370PMW-M130-16419) of Lechecocha 1 rock avalanche

Figure 2. 33: The Paccha flowslide, looking northeast

Initial failure occurred within glacial cover. Flowslide demonstrates high fluidity in run-up on the opposite valley side slope.

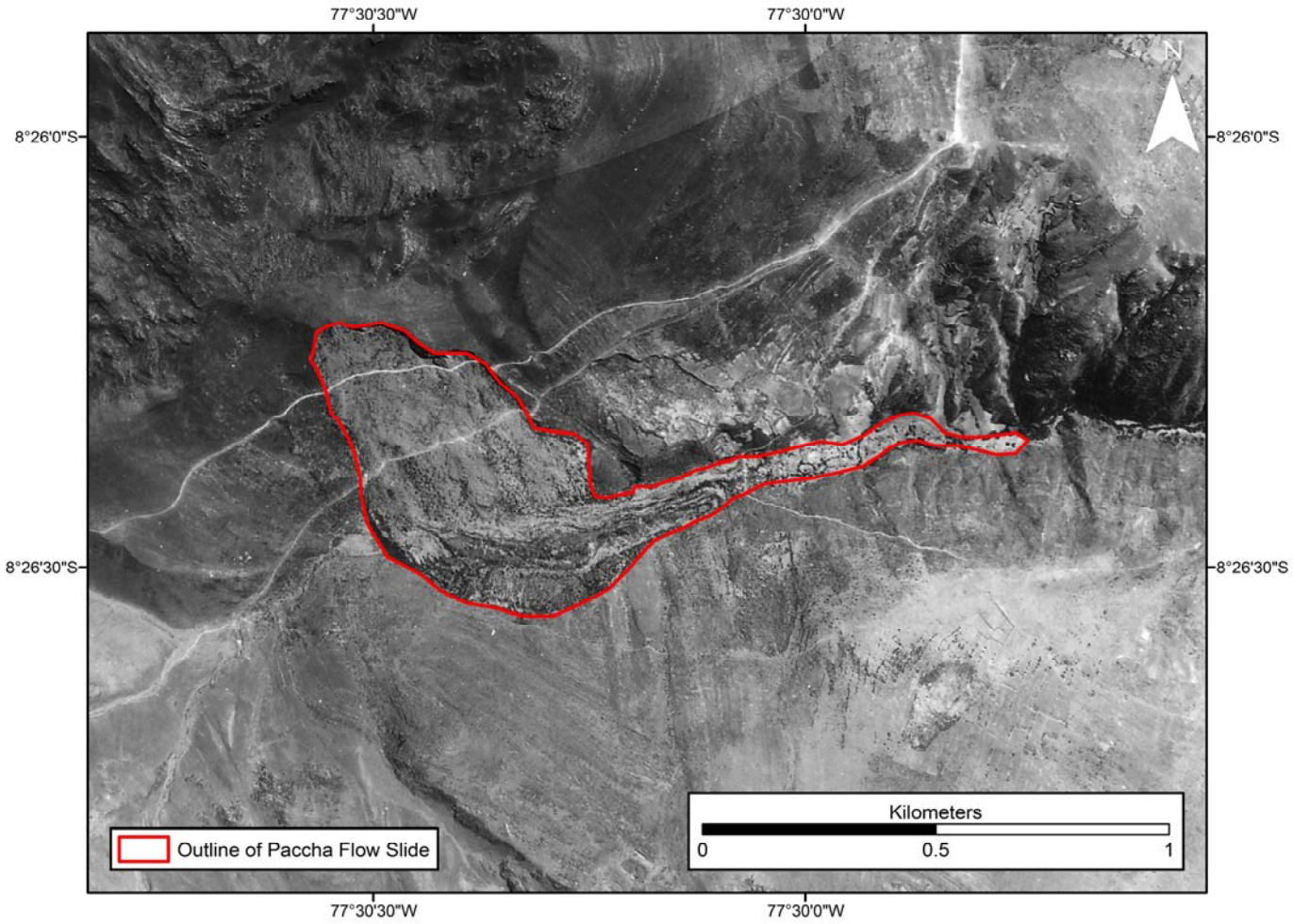

Figure 2. 34: Aerial photograph (1370PMW-M173-22497) of the Paccha flowslide

Figure 2. 35: Glacial (colluvial) materials involved in the Paccha flowslide

Exposure is located in the lateral scarp of the source area. The materials consist of limestone blocks in an argillaceous matrix.

Figure 2. 36: The Peñacocha rock slide

Peñacocha rock slide showing failure along southwest dipping bedding planes into the valley bottom below.

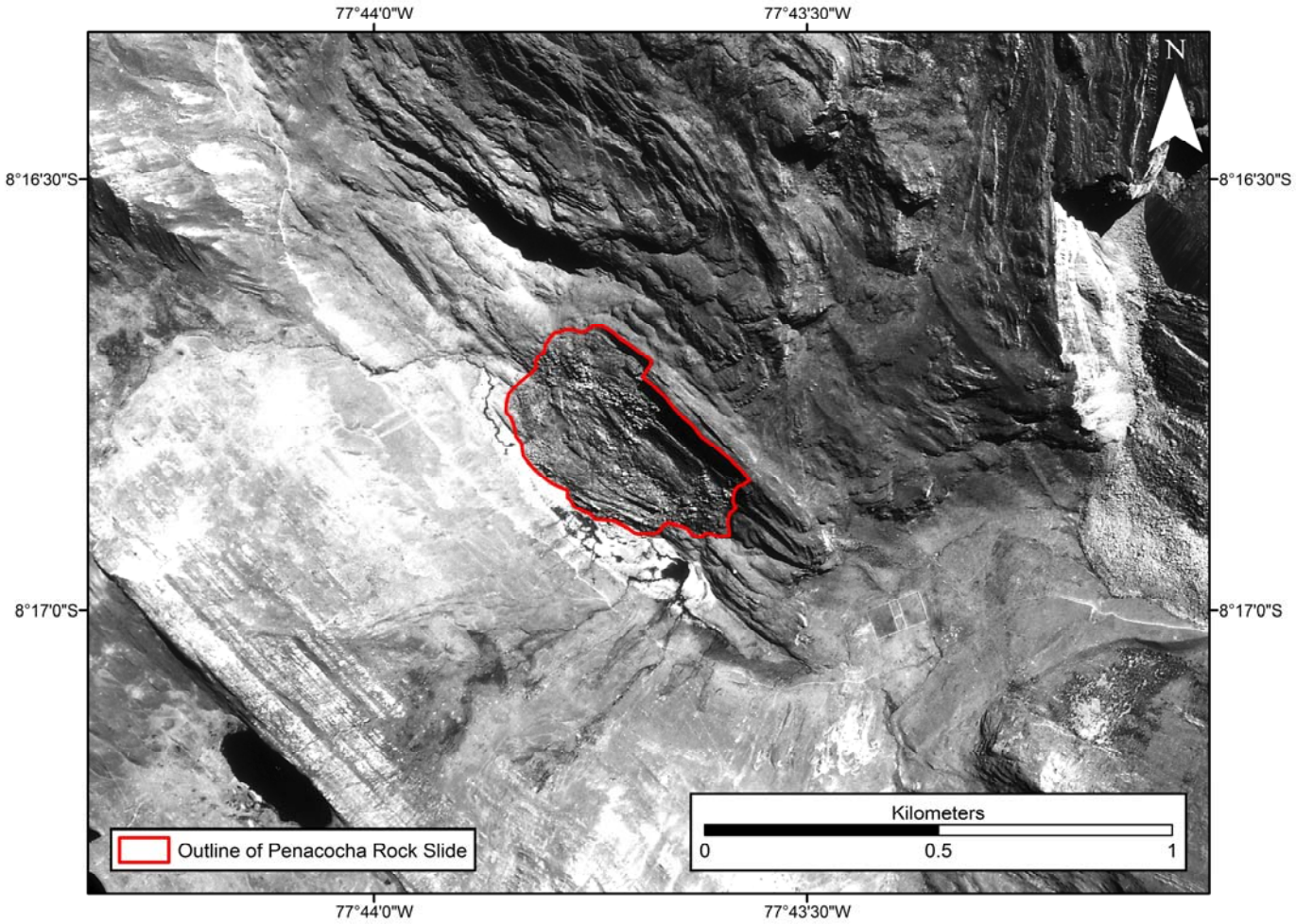

Figure 2. 37: Aerial photograph (1370PMW-M130-16416) of the Peñacocha rock slide

Note Suytucocha rock avalanche at right margin of photograph.

Figure 2. 38: The Trucha rock avalanche, looking north

Initial wedge failure formed by two intersecting discontinuities and prominent nearly-vertical backscarp. View is to the north and bedding is dipping to the west.

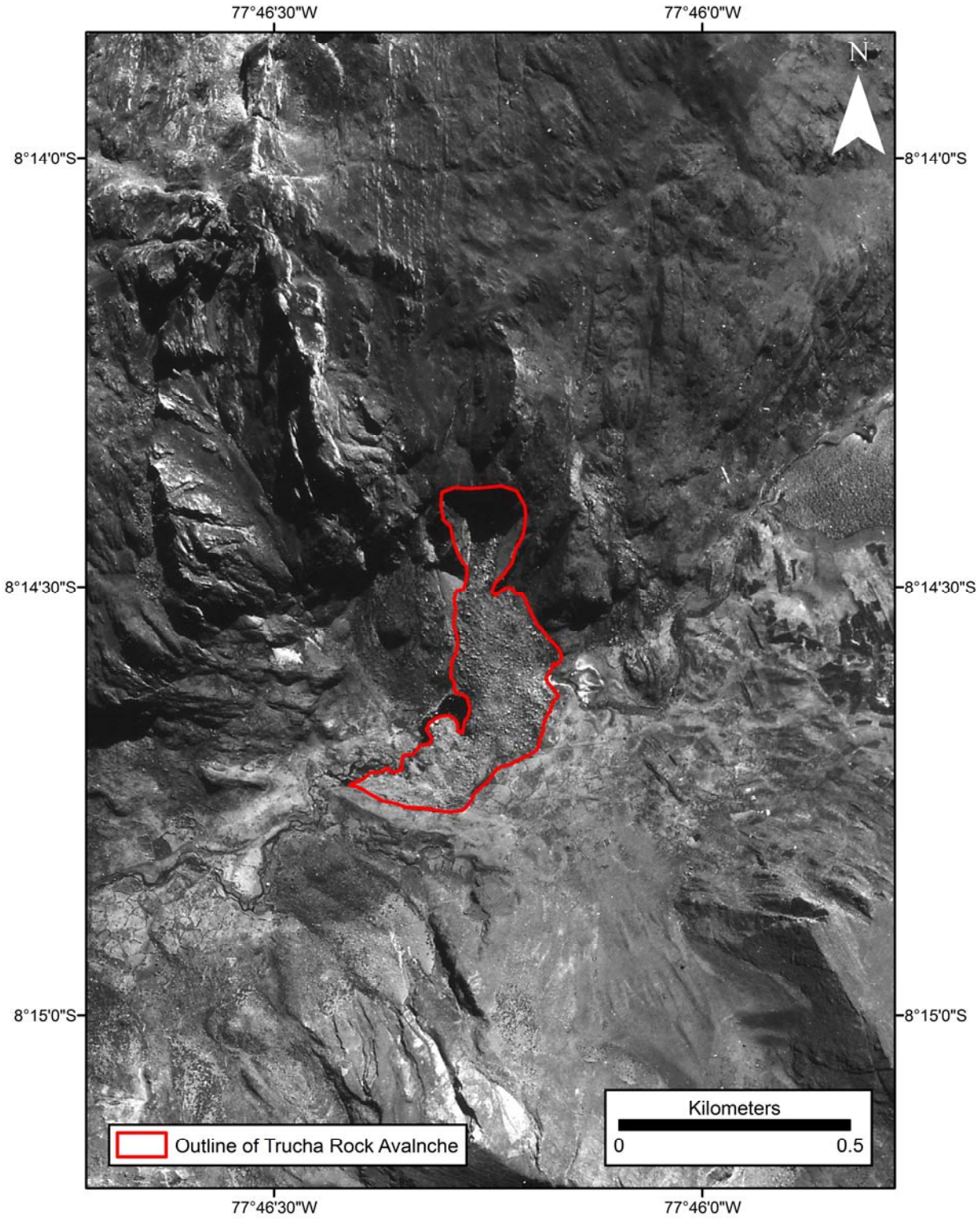

Figure 2. 39: Aerial photograph (1370PMW-M156-20027) of the Trucha rock avalanche

Figure 2. 40: Field observations at the Trucha rock avalanche

Wedge formed by A - east dipping discontinuities and C - west dipping bedding plane. B - Prominent nearly-vertical discontinuity forms backscarp.

Figure 2. 41: Striations plunging to the southwest on the west dipping bedding plane surface of the Trucha rock avalanche

Pencil/eraser scales are parallel to striations.

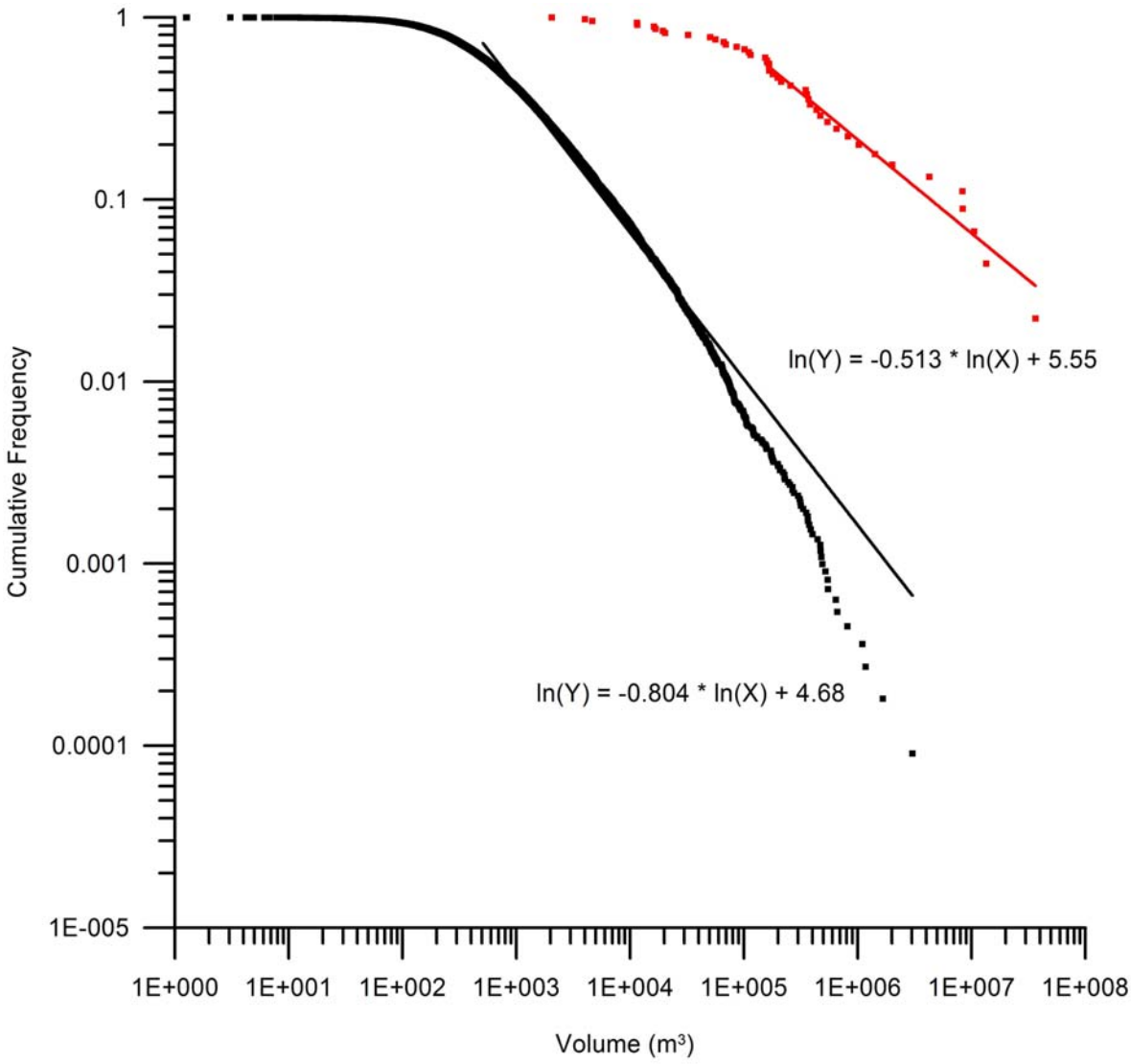

Figure 2. 42: Volume of individual landslides vs. cumulative frequency curves for the 1946 Ancash earthquake (red) and 1994 Northridge earthquake (black) (data from Harp and Jibson, 1995)

Best fit power laws are plotted for the lower part of the plot below the rollover.

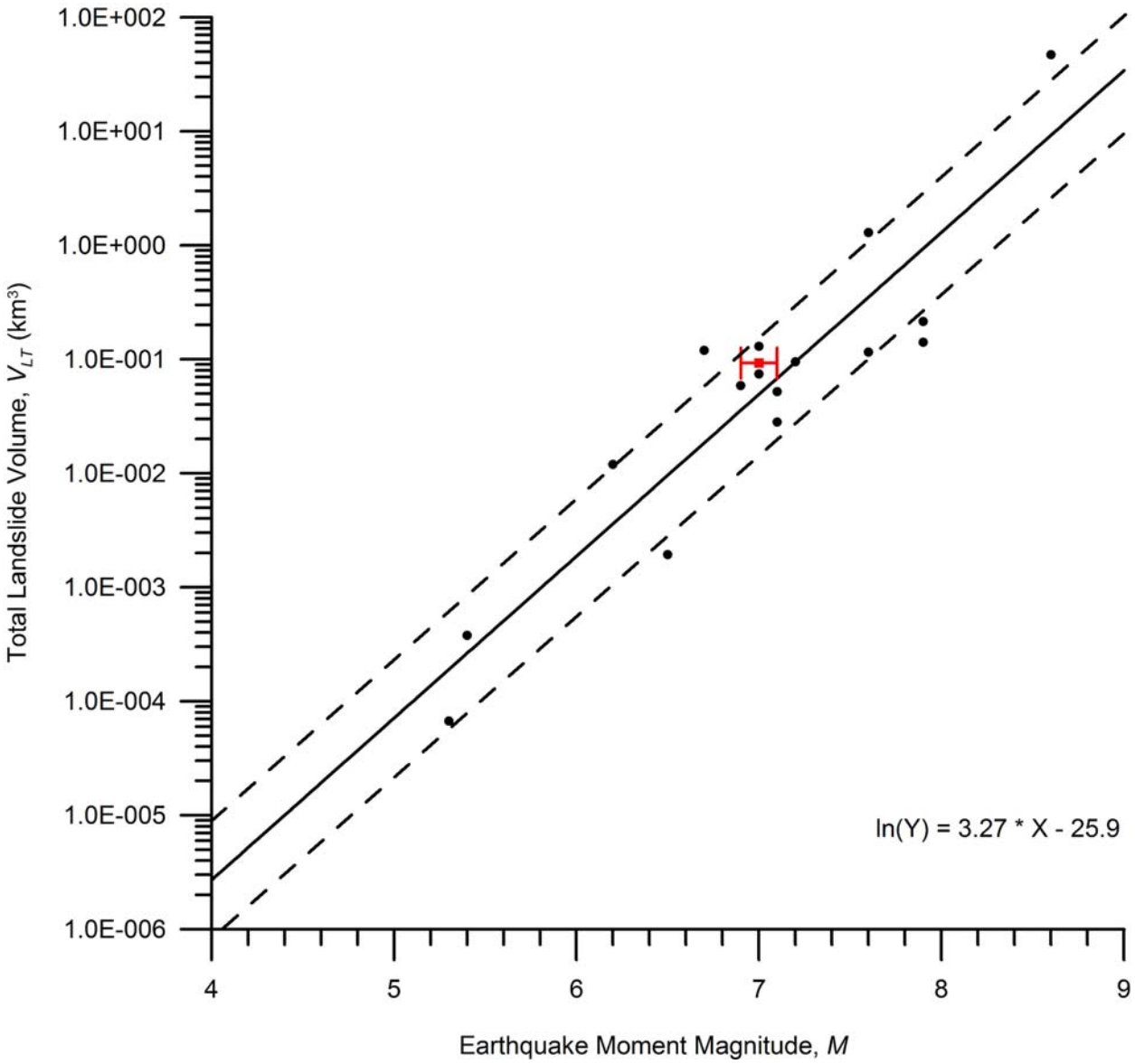

Figure 2. 43: Total landslide volume vs. earthquake moment magnitude

Data from Keefer (1994) and Malamud et al. (2004) (black dots) plotted with exponential best fit line. The 1946 Ancash earthquake data (red dot) is plotted with error bars based on a moment magnitude of 7.0±0.1 (Bellier et al., 1991) and estimated total landslide volume of 9.3E-02 km^3.

Table 2. 3: Inventory of landslides triggered by the 1946 Ancash earthquake

Landslide Number	Name	Failure Type	Latitude	Longitude	Isoseismal Area	Distance to Epicentre (km)	Mapping Unit	Formation	Slope Aspect	Slope Angle	Height (m) H	Length (m) L	Fahrböschung (°) ($\tan^{-1}$H/L)	Area (m^2)	Volume (m^3)
1	Rio Llama	Rock Avalanche	8° 23' 53" S	77° 35' 26" W	IX	28.8	Kis-Pchp	Parihuanca, Chulec, Pariatambo	210°	38°	1343	5104	15	1,397,942	36,550,546
2	Suytucocha	Rock Avalanche	8° 16' 35" S	77° 43' 4" W	IX	14.0	Kis-Pchp	Parihuanca, Chulec, Pariatambo	152°	40°	408	2078	11	712,856	13,503,994
3	Quiches	Debris Avalanche	8° 23' 35" S	77° 30' 18" W	IX	37.7	Kis-Pchp	Parihuanca, Chulec, Pariatambo	036°	35°	639	1662	21	604,495	10,582,563
4	Pelagatos	Debis Avalanche	8° 10' 35" S	77° 49' 3" W	IX	15.7	Ki-saca Ki-chi	Santa, Carhuaz Chimu	013°	31°	585	1284	24	515,513	8,362,779
5	Shundoy	Rock Avalanche	8° 15' 55" S	77° 46' 49" W	IX	8.6	Kis-jc	Jumasha, Celendin	147°	20°	392	1709	13	514,242	8,332,313
6	Acobamba	Rock/Debris Avalanche	8° 19' 51" S	77° 35' 23" W	VII	27.4	Kis-Pchp	Parihuanca, Chulec, Pariatambo	207°	31°	753	2095	20	326,404	4,254,996
7	Lechecocha 1	Rock Avalanche	8° 11' 60" S	77° 45' 2" W	IX	16.1	Kis-Pchp	Parihuanca, Chulec, Pariatambo	204°	21°	771	1722	24	196,212	2,005,002
8	Paccha	Flow Slide	8° 26' 21" S	77° 30' 26" W	IX	38.9	Kis-Pchp	Parihuanca, Chulec, Pariatambo	139°	23°	362	1774	12	155,451	1,421,002
9	Peñacocha	Rock Slide	8° 16' 47" S	77° 43' 40" W	IX	12.9	Kis-Pchp	Parihuanca, Chulec, Pariatambo	214°	19°	83	333	14	124,605	1,024,652
10	Trucha	Rock Avalanche	8° 14' 26" S	77° 46' 13" W	IX	11.3	Kis-jc	Jumasha, Celendin	180°	38°	263	722	20	107,103	819,203
11	Blanca 1	Rock Avalanche	8° 12' 48" S	77° 49' 2" W	IX	11.7	Kis-jc	Jumasha, Celendin	286°	37°	N/A	N/A	N/A	91,647	650,615
12	Blanca 2	Rock Avalanche	8° 12' 55" S	77° 49' 4" W	IX	11.5	Kis-jc	Jumasha, Celendin	287°	37°	N/A	N/A	N/A	80,963	541,672
13	Corona	Rock Avalanche	8° 20' 28" S	77° 39' 58" W	IX	19.2	Kis-jc	Jumasha, Celendin	166°	22°	N/A	N/A	N/A	73,499	469,497
14	Colorado	Rock Slide	8° 14' 52" S	77° 42' 6" W	IX	16.9	Ki-f	Farrat	276°	32°	N/A	N/A	N/A	69,818	435,154
15	Cajón	Rock Avalanche	8° 20' 11" S	77° 43' 35" W	VIII	12.5	Kis-jc	Jumasha, Celendin	230°	46°	N/A	N/A	N/A	63,758	380,490
16	Pilanco 2	Rock Avalanche	8° 18' 8" S	77° 40' 8" W	IX	18.7	Kis-Pchp	Parihuanca, Chulec, Pariatambo	160°	18°	N/A	N/A	N/A	62,494	369,390
17	Pingullo 1	Rock Avalanche	8° 16' 6" S	77° 42' 39" W	IX	15.0	Kis-Pchp	Parihuanca, Chulec, Pariatambo	181°	20°	N/A	N/A	N/A	61,202	358,156
18	Huagur 2	Rock Avalanche	8° 21' 24" S	77° 40' 46" W	IX	18.0	Kis-jc	Jumasha, Celendin	275°	15°	N/A	N/A	N/A	60,297	350,353
19	Prieta	Rock Avalanche	8° 11' 7" S	77° 46' 36" W	IX	16.1	Kis-jc	Jumasha, Celendin	223°	30°	N/A	N/A	N/A	48,868	256,782
20	Blanca 4	Rock Avalanche	8° 13' 9" S	77° 49' 11" W	IX	11.0	Kis-jc	Jumasha, Celendin	275°	33°	N/A	N/A	N/A	42,968	212,300
21	Challhuacocha 3	Rock Avalanche	8° 14' 1" S	77° 45' 11" W	IX	13.1	Kis-Pchp	Parihuanca, Chulec, Pariatambo	295°	35°	N/A	N/A	N/A	40,904	197,397
22	Pingullo 2	Rock Avalanche	8° 16' 31" S	77° 42' 9" W	IX	15.7	Kis-Pchp	Parihuanca, Chulec, Pariatambo	202°	24°	N/A	N/A	N/A	38,390	179,727
23	Huaycocoha	Rock Avalanche	8° 17' 43" S	77° 41' 35" W	IX	16.1	Kis-Pchp	Parihuanca, Chulec, Pariatambo	258°	37°	N/A	N/A	N/A	36,640	167,747
24	Uctucocha	Debris Avalanche	8° 16' 21" S	77° 47' 19" W	IX	7.3	Kis-jc	Jumasha, Celendin	161°	34°	N/A	N/A	N/A	36,441	166,402
25	Muyu Grande 1	Rock Avalanche	8° 15' 7" S	77° 46' 11" W	IX	10.4	Kis-jc	Jumasha, Celendin	331°	38°	N/A	N/A	N/A	36,406	166,166
26	Muyu Grande 2	Rock Avalanche	8° 15' 6" S	77° 46' 16" W	IX	10.3	Kis-jc	Jumasha, Celendin	333°	40°	N/A	N/A	N/A	35,423	159,575
27	Pushas	Rock Avalanche	8° 10' 36" S	77° 46' 25" W	IX	17.1	Kis-jc	Jumasha, Celendin	186°	24°	N/A	N/A	N/A	34,505	153,499
28	Pilanco 1	Rock Avalanche	8° 18' 1" S	77° 40' 2" W	IX	18.9	Kis-Pchp	Parihuanca, Chulec, Pariatambo	179°	15°	N/A	N/A	N/A	28,302	114,515
29	Lechecocha 2	Rock Avalanche	8° 11' 58" S	77° 44' 44" W	IX	16.5	Kis-Pchp	Parihuanca, Chulec, Pariatambo	197°	28°	N/A	N/A	N/A	27,569	110,158
30	Challhuacocha 1	Rock Avalanche	8° 13' 8" S	77° 44' 54" W	IX	14.7	Kis-Pchp	Parihuanca, Chulec, Pariatambo	251°	35°	N/A	N/A	N/A	26,025	101,160
31	Labrascocha	Rock Avalanche	8° 15' 11" S	77° 45' 55" W	IX	10.7	Kis-jc	Jumasha, Celendin	048°	28°	N/A	N/A	N/A	23,366	86,259
32	Blanca 3	Rock Avalanche	8° 13' 6" S	77° 49' 8" W	IX	11.0	Kis-jc	Jumasha, Celendin	280°	34°	N/A	N/A	N/A	20,131	69,202
33	Challhuacocha 2	Rock Avalanche	8° 13' 23" S	77° 44' 59" W	IX	14.2	Kis-Pchp	Parihuanca, Chulec, Pariatambo	306°	33°	N/A	N/A	N/A	19,616	66,601
34	Michito Grande 2	Rock Avalanche	8° 17' 36" S	77° 45' 60" W	IX	8.3	Kis-jc	Jumasha, Celendin	232°	24°	N/A	N/A	N/A	17,519	56,349
35	Huagur 1	Rock Avalanche	8° 21' 39" S	77° 40' 58" W	IX	17.8	Kis-jc	Jumasha, Celendin	200°	19°	N/A	N/A	N/A	16,300	50,650
36	Camino Peligroso 2	Rock Avalanche	8° 19' 59" S	77° 44' 43" W	VIII	10.3	Kis-jc	Jumasha, Celendin	230°	21°	N/A	N/A	N/A	12,051	32,408
37	Camino Peligroso 5	Rock Avalanche	8° 20' 19" S	77° 44' 28" W	VIII	11.0	Kis-jc	Jumasha, Celendin	216°	35°	N/A	N/A	N/A	8,781	20,296
38	Michito Grande 1	Rock Avalanche	8° 17' 25" S	77° 46' 9" W	IX	8.2	Kis-jc	Jumasha, Celendin	224°	25°	N/A	N/A	N/A	8,503	19,353
39	Michito Grande 4	Rock Avalanche	8° 18' 37" S	77° 44' 56" W	IX	9.8	Kis-jc	Jumasha, Celendin	207°	18°	N/A	N/A	N/A	7,694	16,694
40	Michito Grande 3	Rock Avalanche	8° 17' 58" S	77° 45' 39" W	IX	8.7	Kis-jc	Jumasha, Celendin	232°	33°	N/A	N/A	N/A	7,531	16,173
41	Yanabamba	Rock Fall	8° 18' 44" S	77° 45' 56" W	VIII	8.0	Kis-jc	Jumasha, Celendin	N/A	N/A	N/A	N/A	N/A	6,003	11,566
42	Camino Peligroso 3	Rock Avalanche	8° 20' 8" S	77° 44' 35" W	VIII	10.4	Kis-jc	Jumasha, Celendin	237°	42°	N/A	N/A	N/A	5,970	11,472
43	Camino Peligroso 4	Rock Avalanche	8° 20' 16" S	77° 44' 31" W	VIII	10.8	Kis-jc	Jumasha, Celendin	231°	29°	N/A	N/A	N/A	3,243	4,654
44	Camino Peligroso 6	Rock Avalanche	8° 20' 24" S	77° 44' 25" W	VIII	11.1	Kis-jc	Jumasha, Celendin	210°	38°	N/A	N/A	N/A	2,937	4,020
45	Camino Peligroso 1	Rock Avalanche	8° 19' 41" S	77° 45' 4" W	VIII	9.7	Kis-jc	Jumasha, Celendin	220°	20°	N/A	N/A	N/A	1,864	2,052

N/A means not applicable.

Chapter 3
Initial failure mechanisms of earthquake-triggered rock avalanches; relationship to rock mass structure

3.1 Introduction

As documented in the previous chapter, a total of 45 landslides are inferred to have been triggered by the M7.3 Ancash earthquake that occurred on November 10, 1946 in the northern Andean region of Peru. Of these landslides, 83% were rock avalanches which occurred within the epicentral area. Many of these rock avalanches displayed strong field evidence of wedge failure.

3.1.1 Objectives

The main objective of this chapter is to evaluate the failure mechanism in relation to the rock mass structure at three sites selected in the epicentral region. Secondly, the application of conventional wedge failure criteria is evaluated against field data for wedge failures in this region. Thirdly, for those wedge failures which do not meet conventional wedge failure criteria, new wedge criteria applicable to the wedge failures studied in the Ancash region are developed.

3.1.2 Methodology

Field work was carried out in July 2007 and June 2008 within the epicentral area of the 1946 Ancash earthquake by vehicle and foot traverses. Three rock avalanche sites were investigated and field measurements including the strike and dip of prominent discontinuities as well as orientation of striations were recorded. The topographic centre of the wedge was also established for two of the sites and was defined based on aerial photo interpretation, indicating the approximate line at which the two intersecting discontinuities meet and exit out of the slope. A 25 m resolution digital elevation model (DEM) was utilized in order to construct slope profiles for the individual rock avalanches. Landsat 7 ETM + imagery and georeferenced aerial photographs taken in 1962 were also used in conjunction with the DEM to locate rock avalanche sites using GIS. In addition, DIPS software was used to evaluate rock mass fabric measurements and construct structural plots on stereographic projections.

3.2 Conventional Wedge Failure

Wedge failure may occur in a rock slope when two sets of discontinuities intersect to form a wedge shaped block (e.g. Goodman, 1976; Hoek and Bray, 1977, Norrish and Wyllie, 1996; Wyllie and Mah,

2004). Wedge failure occurs when the line of intersection, which forms the axis of sliding, daylights in the slope and plunges at a higher angle than the friction angle for the material involved (Hoek and Bray, 1977). We term this mode of wedge failure, conventional wedge failure.

The formation and occurrence of wedge failures are largely dependent on the lithology and structure of the rock mass (Piteau, 1972). Wedge failures are common in dipping sedimentary rocks because they exhibit bedding planes and well defined orthogonal joint sets that give rise to favourable rock mass fabric geometry for wedge development (Norrish and Wyllie, 1996).

In order to evaluate the failure potential of a wedge it is necessary to undertake a kinematic analysis of rock mass discontinuities. Three criteria and one test are used in the kinematic analysis of potential conventional wedge failure.

3.2.1 Wedge Shape Criteria and Orientation of Line of Intersection

In order for wedge failure to occur, two discontinuities within a rock mass need to intersect in a line, to form a line of intersection (Figure 3. 1) (Hoek and Bray, 1977). Stereographic projection can define the shape of the wedge as well as the trend and plunge of the line of intersection (Hoek and Bray, 1977). The line of intersection is represented stereographically by the point where the two discontinuities intersect (Figure 3. 2).

The trend of the line of intersection (α_i), which indicates the direction of potential sliding, and the plunge of the line of intersection (ψ_i) can be estimated from the stereographic projection or calculated using the Equations 3. 1 and 3. 2 below which are modified after Equations 7.1 and 7.2 in Wyllie and Mah, (2004, p.156):

$$\alpha_i = \tan^{-1}((\tan\psi_A \cos\alpha_A - \tan\psi_B \cos\alpha_B)/(\tan\psi_B \sin\alpha_B - \tan\psi_A \sin\alpha_A)) + 180^\circ \quad \text{[Equation 3. 1]}$$

$$\psi_i = \tan^{-1}(\tan\psi_A \cos(\alpha_A - \alpha_i) = \tan\psi_B \cos(\alpha_B - \alpha_i)) \quad \text{[Equation 3. 2]}$$

Where α_A is the dip direction of discontinuity A, α_B is the dip direction of discontinuity B, ψ_A is the dip of discontinuity A, and ψ_B is the dip of discontinuity B (Figure 3. 2).

3.2.2 Kinematic Criteria

In order to meet the kinematic criteria for wedge failure, the line of intersection must daylight in the slope; therefore it must be less than the dip of the slope and plunge out of the slope (Goodman, 1976; Hoek and Bray, 1977). In addition, failure is only possible when the plunge of the line of intersection is greater than the angle of friction of the two intersecting discontinuities that form the wedge (Goodman,

1976; Hoek and Bray, 1977). Where the angles of friction are distinctly different for the two intersecting discontinuities, an average friction angle is assumed (Norrish and Wyllie, 1996).

Therefore, the plunge of the line of intersection (ψ_i) must be less than the dip of the slope parallel to the line of intersection (ψ_{fi}) and greater than the average friction angle (ϕ) of the two discontinuities forming the wedge (Equation 3. 3) (Figure 3. 3) (Goodman, 1976; Hoek and Bray, 1977).

$$\psi_{fi} > \psi_i > \phi \qquad \text{[Equation 3. 3]}$$

Plotting these criteria on a stereographic projection yields the wedge failure envelope (Figure 3. 2) (Hoek and Bray, 1977).

It is important to note that the dip of the slope face in Equation 3. 3 is determined parallel to the line of intersection. Therefore, the dip of the slope parallel to the line of intersection (ψ_{fi}) would only be the same as the true dip of the slope (ψ_f) if the dip direction of the slope (α_f) were the same as the trend of the line of intersection (α_i) (Hoek and Bray, 1977).

3.2.3 Trend Criteria

In order for sliding of the wedge to occur, the trend of the line of intersection (α_i) must plunge approximately parallel to the dip direction of the slope (α_f) (Norrish and Wyllie, 1996; Kliche, 1999; Wyllie and Mah, 2004). A range of ±20° of the dip direction of the slope has been established to satisfy the trend criteria for the line of intersection (Figure 3. 2) (Kliche, 1999):

$$(\alpha_f - 20^\circ) \leq \alpha_i \leq (\alpha_f + 20^\circ) \qquad \text{[Equation 3. 4]}$$

3.2.4 Markland's Test

Stereographic analysis can also determine whether sliding of a wedge will occur on both wedge forming discontinuities, indicating wedge failure, or on only one of the two, in which case the failure will be planar, a procedure referred to as Markland's Test (Figure 3. 2) (Goodman, 1976; Hoek and Bray, 1977). If the dip direction of discontinuity A (α_A) or the dip direction of discontinuity B (α_B) is between the trend of the line of intersection (α_i) and the dip direction of the slope (α_f) then sliding will occur on the plane whose dip direction is closest to the dip direction of the slope, usually the steeper of the planes, in the direction of maximum dip, resulting in planar failure. Otherwise sliding occurs along the line of intersection along both planes forming the wedge, resulting in wedge failure (Hoek and Bray, 1977; Norrish and Wyllie, 1996; Öcal and Özgenoğlu, 1997). In order to determine whether the wedge is sliding simultaneously along both planes (wedge failure) or along a single plane (planar failure), the following equations based on Hoek and Bray (1977) are used:

When the dip direction of the slope (α_f) is greater than the trend of the line of intersection (α_i):

If $\alpha_f > \alpha_A$ and/or $\alpha_B > \alpha_i$ [Equation 3. 5]

OR if the trend of the line of intersection (α_i) is greater than the dip direction of the slope (α_f)

If $\alpha_i > \alpha_A$ and/or $\alpha_B > \alpha_f$ [Equation 3. 6]

Then, if either the dip direction of discontinuity A or discontinuity B satisfy the criteria then sliding will occur along that discontinuity in the direction of maximum dip resulting in planar failure. If both dip directions of discontinuity A and discontinuity B satisfy the criteria then sliding will occur along the plane whose dip direction is closest to the dip direction of the slope. However, if neither the dip direction of discontinuity A or discontinuity B satisfies the criteria then sliding of the wedge will occur along both planes, resulting in wedge failure along the line of intersection (Figure 3. 2).

3.3 Wedge Failures Triggered by the 1946 Ancash Earthquake

Three rock avalanches were studied in order to gain a clearer understanding of the mechanism of wedge failures triggered by the 1946 Ancash earthquake; Camino Peligroso, Suytucocha and Trucha (Table 3. 1) (Figure 3. 4).

The Suytucocha rock avalanche was reported as triggered by the 1946 Ancash earthquake (Silgado, 1951). However, the two other rock avalanches, Camino Peligroso rock avalanche and Trucha rock avalanche, located in close proximity to the Suytucocha rock avalanche, are inferred to have occurred as a result of the earthquake, due to the similarity in debris morphology and appearance at the three sites.

The topography and lithology of the three rock avalanche wedge failures are comparable. All three wedge failures occurred on steep slopes along valleys trending either northeast-southwest or northwest-southeast. The dip directions of the slopes are roughly perpendicular to the trend of the valley, facilitating wedge movement out of the slope.

In addition to their comparable topography and lithology, the three wedge failures also show a similar structural pattern in bedding and jointing. Bedding within all three wedge failures is the most prominent discontinuity, dipping to the southwest. In addition, two joint sets follow a similar structural pattern; J1 dips steeply to the northeast or southwest and J2 dips steeply to the northwest or southeast. Both joint sets aid in the development of wedge failure through either forming the second intersecting discontinuity needed for wedge failure or by providing a backscarp, which acts as a release surface for the wedge. A stereographic projection summarizes the conceptual structural pattern of the wedge failures studied in the epicentral region (Figure 3. 5).

Table 3. 1: Summary table of three wedge failures triggered by the 1946 Ancash earthquake

Wedge Failure	Camino Peligroso	Suytucocha	Trucha
Latitude	8° 20' 8" S	8° 16' 35" S	8° 14' 26" S
Longitude	77° 44' 35" W	77° 43' 4" W	77° 46' 13" W
Isoseismal Area	VIII	IX	IX
Distance to Epicentre	10.4 km	14.0 km	11.3 km
Mapping Unit	Kis-jc	Kis-Pchp	Kis-jc
Formation	Jumasha, Celendin	Parihuanca, Chulec, Pariatambo	Jumasha, Celendin
Slope Angle	42°	40°	38°
Slope Dip Direction	237°	152°	180°

All three landslides occurred in formations composed of Cretaceous limestone. A friction angle of 30° was therefore selected and is considered representative of the strength of discontinuities in limestone (Cruden and Hu, 1988).

3.3.1 Camino Peligroso Rock Avalanche

The Camino Peligroso rock avalanche (Figure 3. 4) is located approximately 10 km northwest of the town of San Miguel, in the Department of Ancash. The rock avalanche is situated within the VIII intensity isoseismal and is approximately 10.4 km from the Ancash earthquake epicenter.

3.3.1.1 Topography and Geology

The Camino Peligroso rock avalanche (Figure 3. 6 and 3. 7) is located on the northeast side of a valley trending northwest-southeast. The northwest-southeast strike of the bedding is roughly parallel to the northwest-southeast trend of the valley and the dip of the bedding planes is roughly perpendicular to the northwest-southeast trend of the valley. The sliding area, deposit area and location of the slope profile for the Camino Peligroso rock avalanche is outlined on a contour map (Figure 3. 8). An average slope of 42° and slope dip direction S 237° W was measured along the slope profile (Figure 3. 9).

The source slope is underlain by limestone, calcareous shale and dolomite of the Jumasha and Celendin formations (Late Cretaceous) (Sanchez Fernandez, 1995). The rock mass involved in the failure of Camino Peligroso consists of massive limestone with orthogonal fractures. Striations were observed along the planar southwest dipping bedding plane, which formed a sliding surface, indicating the direction of wedge movement out of the slope.

3.3.1.2 Rock Mass Fabric

Rock mass fabric measurements, including striations and the dip and strike of bedding and joints were taken in undisturbed rock masses at the Camino Peligroso rock avalanche site. Poles were plotted on a lower hemisphere of an equal area stereographic projection (Figure 3. 10) which displays the slope, friction angle, orientation of striations and the conventional wedge failure envelope.

Three major pole concentrations exist, bedding (B), joint set 1 (J1) and joint set 2 (J2) (Figure 3. 10). Bedding has a dip/dip direction of 31°/214° and is dipping to the southwest out of the slope. J1 has a dip/dip direction of 76°/228° and is steeply dipping to the southwest slightly out of the slope. J2 has a dip/dip direction of 86°/309° and is steeply dipping to the northwest across the slope.

3.3.1.3 Conventional Wedge Failure Criteria

In order for conventional wedge failure to occur at the Camino Peligroso rock avalanche site under these geological conditions, three criteria outlined for wedge failure must be met. The Camino Peligroso rock avalanche satisfies the wedge shape criteria, since the bedding (B) and joint set J2 intersect to form a line of intersection. The trend (α_i) and plunge (ψ_i) of the line of intersection of B and J2 is shown on the stereonet and was calculated using Equations 3. 1 and 3. 2 (Wyllie and Mah, 2004):

$$\alpha_i=(\tan^{-1}((\tan\psi_{J2}\cos\alpha_{J2}-\tan\psi_B\cos\alpha_B)/(\tan\psi_B\sin\alpha_B-\tan\psi_{J2}\sin\alpha_{J2})))+180^\circ \quad \text{[Equation 3. 1]}$$

$$\alpha_i=(\tan^{-1}((\tan86^\circ\cos309^\circ-\tan31^\circ\cos214^\circ)/(\tan31^\circ\sin214^\circ-\tan86^\circ\sin309^\circ)))+180^\circ$$

$$\alpha_i = 221^\circ$$

$$\psi_i=\tan^{-1}(\tan\psi_{J2}\cos(\alpha_{J2}-\alpha_i)=\tan\psi_B\cos(\alpha_B-\alpha_i)) \quad \text{[Equation 3. 2]}$$

$$\psi_i=\tan^{-1}(\tan86^\circ\cos(309^\circ-221^\circ)=\tan31^\circ\cos(214^\circ-221^\circ))$$

$$\psi_i= 31^\circ$$

The trend of the line intersection is 221° and the plunge of the line of intersection is 31°.

In addition, the Camino Peligroso rock avalanche satisfies the kinematic criteria for wedge failure, with a slope dip parallel to the line of intersection (ψ_{fi}) of 41°, an average friction angle (ϕ) of 30° and a line of intersection plunge (ψ_i) of 31°:

$$\psi_{fi} > \psi_i > \phi \qquad \text{[Equation 3. 3]}$$

$$41^\circ > 31^\circ > 30^\circ$$

Therefeore, the line of intersection daylights in the slope and is great enough to overcome the friction angle of the two intersecting discontinuities.

The Camino Peligroso rock avalanche also satisfies the trend criteria outlined, the trend of the line of intersection (α_i) is within 20° degrees of the dip direction of the slope (α_f):

$$(\alpha_f - 20^\circ) \leq \alpha_i \leq (\alpha_f + 20^\circ) \qquad \text{[Equation 3. 4]}$$

$$(237^\circ - 20^\circ) \leq 221^\circ \leq (237^\circ + 20^\circ)$$

$$217^\circ \leq 221^\circ \leq 257^\circ$$

Lastly, Markland's test indicates that sliding of the wedge is occurring along both discontinuities B and J2 at the Camino Peligroso rock avalanche resulting in wedge failure, since neither the dip direction of discontinuity B or discontinuity J2 is situated between the trend of the line of intersection (α_i) and the dip direction of the slope (α_f):

$$\alpha_f > \alpha_A \text{ and/or } \alpha_B > \alpha_i \qquad \text{[Equation 3. 5]}$$

$$237^\circ > 214^\circ \text{ and/or } 309^\circ > 221^\circ$$

Based on the criteria outlined for wedge failure, the Camino Peligroso rock avalanche initiated due to wedge failure, as is evident in the stereographic projection (Figure 3. 10). The point of intersection lies within the wedge failure envelope because the kinematic criteria are satisfied. The stereonet also shows joint set J1 striking roughly parallel to the slope, dipping nearly-vertical, which aids in release of the wedge block out of the slope (Figure 3. 10). As a result, wedge failure occurred at the Camino Peligroso rock avalanche with the intersection of the bedding (B) and joint set 2 (J2), with a steep line of intersection plunging in a southwest direction out of the slope (Figure 3. 10).

3.3.1.4 Planar Failure

There is also a potential for planar sliding at the Camino Peligroso rock avalanche as is evident in the stereographic projection (Figure 3. 11). Planar sliding will occur on those planes whose poles lie within the planar failure envelope and outside the friction circle (Hoek and Bray, 1977). A large portion of

bedding plane (B) poles plot within the planar failure envelope, which indicates that planar failure may have also occurred in combination with wedge failure in a southwest direction out of the slope (Figure 3. 11). However, it is noted that the true dip direction of the bedding (B) is parallel to the trend of the line of intersection. The wedge is formed by the bedding (B) and the orthogonal joint set J2 which strikes roughly parallel to the bedding dip direction. Thus the Camino Peligroso failure is a wedge failure as indicated by Markland's Test.

3.3.2 Suytucocha Rock Avalanche

The Suytucocha rock avalanche is situated within the IX intensity isoseismal approximately 14.0 km from the Ancash earthquake epicentre and approximately 5 km west of the town of Mayas, in the Department of Ancash (Figure 3. 4).

3.3.2.1 Topography and Geology

The Suytucocha rock avalanche (Figure 3. 12 and 3. 13) is located on the north side of the Suytucocha valley that trends northeast-southwest. The northwest-southeast strike of the bedding is roughly perpendicular to the northeast-southwest orientation of the valley and thus the dip of the bedding planes is roughly parallel to the valley. The sliding area, deposit area and location of the slope profile for the Suytucocha rock avalanche is shown on a contour map (Figure 3. 14). An average slope of 40° and slope orientation of S 152° E was estimated for the source slope (Figure 3. 15).

The rock mass involved in the failure at the Suytucocha rock avalanche is a massive grey limestone with irregular fractures of the Parihuanca, Chulec and Pariatambo formations (Early Cretaceous) (Sanchez Fernandez, 1995). Field observations also suggested the presence of minor shale interbeds within the limestone sequence. The wedge failure appears to have partially involved sliding along a planar southwest dipping bedding plane before exiting the slope.

3.3.2.2 Rock Mass Fabric

Rock mass fabric measurements, including dip and strike of bedding and joints, were taken in undisturbed rock masses at the Suytucocha site. Poles are plotted on a lower hemisphere of equal area stereographic projection which displays the slope, friction angle, topographic centre of the wedge and the conventional wedge failure envelope (Figure 3. 16).

Three major pole concentrations exist, bedding (B), joint set 1 (J1) and joint set 2 (J2) (Figure 3. 16). Bedding (Figure 3. 17) has a dip/dip direction of 37°/219° and is moderately dipping to the southwest. J1 (Figure 3. 18) has a dip/dip direction of 75°/090° and is steeply dipping to the east. J1 is a remote

measurement of the orientation of the lateral scarp and differs slightly from the pole concentrations measured on outcrops. J2 (Figure 3. 19) has a dip/dip direction of 73°/313° and is steeply dipping to the northwest. The intersection of all three discontinuities (Figure 3. 20) occurs at the base of the headscarp.

3.3.2.3 Conventional Wedge Failure Criteria

Three criteria must be met in order for wedge failure to occur at the Suytucocha rock avalanche site under these geological conditions. The Suytucocha rock avalanche satisfies the conventional wedge shape criteria, since bedding plane B and joint set J1 intersect to form a line of intersection. The trend (α_i) and plunge (ψ_i) of the line of intersection of B and J1 can be determined on the stereonet (Figure 3. 16) or calculated (Wyllie and Mah, 2004):

$$\alpha_i=(\tan^{-1}((\tan\psi_{J1}\cos\alpha_{J1} - \tan\psi_B\cos\alpha_B)/(\tan\psi_B\sin\alpha_B - \tan\psi_{J1}\sin\alpha_{J1}))) + 180^\circ \quad \text{[Equation 3. 1]}$$

$$\alpha_i=(\tan^{-1}((\tan75^\circ\cos90^\circ - \tan37^\circ\cos219^\circ)/(\tan37^\circ\sin219^\circ - \tan75^\circ\sin90^\circ))) + 180^\circ$$

$$\alpha_i = 172^\circ$$

$$\psi_i=\tan^{-1}(\tan\psi_{J1}\cos(\alpha_{J1}-\alpha_i) = \tan\psi_B\cos(\alpha_B-\alpha_i)) \quad \text{[Equation 3. 2]}$$

$$\psi_i=\tan^{-1}(\tan75^\circ\cos(90^\circ-172^\circ) = \tan37^\circ\cos(219^\circ-172^\circ))$$

$$\psi_i= 27^\circ$$

The trend of the line intersection is thus 172° and the plunge of the line of intersection is 27°.

The Suytucocha rock avalanche, however, does not satisfy the kinematic criteria outlined above for conventional wedge failure, with a slope dip parallel to the line of intersection (ψ_{fi}) of 39°, a friction angle (ϕ) of 30° and a plunge of the line of intersection (ψ_i) of 27°:

$$\psi_{fi} > \psi_i > \phi \quad \text{[Equation 3. 3]}$$

$$39^\circ > 27^\circ < 30^\circ$$

The plunge of the line of intersection is not greater than the friction angle, therefore the point of intersection does not lie within the conventional wedge failure envelope.

The Suytucocha rock avalanche does satisfy the criteria outlined for the trend of the line of intersection (α_i) and is within 20° degrees of the dip direction of the slope (α_f):

$$(\alpha_f - 20^\circ) \leq \alpha_i \leq (\alpha_f + 20^\circ) \quad \text{[Equation 3.4]}$$

$$(152^\circ - 20^\circ) \leq 172^\circ \leq (152^\circ + 20^\circ)$$

$$132^\circ \leq 172^\circ \leq 172^\circ$$

Lastly, Markland's Test indicates that sliding of the wedge is occurring along both B and J1 at the Suytucocha rock avalanche, since neither the dip direction of bedding B (α_B) or joint set J1 (α_{J1}) is situated between the trend of the line of intersection (α_i) and the dip direction of the slope (α_f):

$$\alpha_i > \alpha_B \text{ and/or } \alpha_{J1} > \alpha_f \qquad \text{[Equation 3. 6]}$$

$$172^\circ > 219^\circ \text{ and/or } 90^\circ > 152^\circ$$

Based on the analysis of the measured rock mass fabric and the evaluation of the criteria outlined above for conventional wedge failure, it is not evident that the Suytucocha rock avalanche occurred due to wedge failure (Figure 3. 16). The point of intersection lies outside the wedge failure envelope and does not satisfy the kinematic criteria. In order for the point of intersection of the two intersecting planes to fall within the wedge failure envelope, a friction angle less than 27° is required. Therefore, it is not apparent that the Suytucocha rock avalanche developed as a wedge failure given our assumption of the value of internal friction (30°) for the limestone involved.

3.3.3 Trucha Rock Avalanche

The Trucha rock avalanche (Figure 3. 4) is located approximately 12 km northwest of the town of Mayas, in the Department of Ancash within the IX intensity isoseismals roughly 11.3 km from the Ancash earthquake epicentre.

3.3.3.1 Geology and Topography

The Trucha rock avalanche (Figure 3. 21 and 3. 22) is located on the north side of a valley trending northeast-southwest (Sanchez Fernandez, 1995). The north-south strike of the bedding is roughly perpendicular to the northeast-southwest orientation of the valley and the dip of the bedding planes is therefore roughly parallel to the northeast-southwest orientation of the valley. The sliding area, deposit area and location of the slope profile for the Trucha rock avalanche is shown on a contour map (Figure 3. 23). An average source slope angle of 38° and slope orientation of S 180° E was estimated from the slope profile (Figure 3. 24).

The slope is underlain by limestone, calcareous shale and dolomite of the Jumasha and Celendin formations (Late Cretaceous) (Sanchez Fernandez, 1995). Field observations indicate that the rock mass involved in the failure is a massive limestone with orthogonal fractures. Within the massive limestone, a thin weaker unit, most likely composed of shale was also observed. Striations along the main bedding plane surface were noted and indicate a southwesterly direction for wedge movement (Figure 3. 25).

3.3.3.2 Rock Mass Fabric

Rock mass fabric measurements, including strike and dip of bedding and joints as well as striations on the bedding surface were taken in undisturbed rock masses at the Trucha rock avalanche site. Poles are plotted on a lower hemisphere of equal area stereographic projection which displays the slope, friction angle, topographic centre of the wedge, striations and the wedge failure envelope (Figure 3. 25).

Three major pole concentrations exist at the Trucha rock avalanche site, bedding (B), joint set 1 (J1) and joint set 2 (J2). Bedding (Figure 3. 26) has a dip/dip direction of 44°/260° and is moderately dipping to the west. J1 (Figure 3. 27) has a dip/dip direction of 59°/111° and is steeply dipping to the east. J2 (Figure 3. 28) has a dip/dip direction of 77°/170° and is steeply dipping to the south. The intersection of all three discontinuities occurs at the base of the headscarp (Figure 3. 29).

3.3.3.3 Conventional Wedge Failure Criteria

Three criteria are required for wedge failure to occur at the Trucha rock avalanche site under these geological conditions. The Trucha rock avalanche satisfies the wedge shape criteria since bedding B and joint set J1 intersect to form a line of intersection. The trend (α_i) and plunge (ψ_i) of the line of intersection of B and J1 can be determined on the stereographic projection or calculated using Equations 3. 1 and 3. 2 (Wyllie and Mah, 2004):

$$\alpha_i=(\tan^{-1}((\tan\psi_{J1}\cos\alpha_{J1} - \tan\psi_B \cos\alpha_B)/(\tan\psi_B \sin\alpha_B - \tan\psi_{J1} \sin\alpha_{J1}))) + 180^\circ \quad \text{[Equation 3. 1]}$$

$$\alpha_i=(\tan^{-1}((\tan59^\circ \cos111^\circ - \tan44^\circ \cos260^\circ)/(\tan44^\circ \sin260^\circ - \tan59^\circ \sin111^\circ))) + 180^\circ$$

$$\alpha_i = 190^\circ$$

$$\psi_i=\tan^{-1}(\tan\psi_{J1} \cos(\alpha_{J1}-\alpha_i) = \tan\psi_B \cos(\alpha_B-\alpha_i)) \quad \text{[Equation 3. 2]}$$

$$\psi_i=\tan^{-1}(\tan59^\circ \cos(111^\circ-190^\circ) = \tan44^\circ \cos(260^\circ-190^\circ))$$

$$\psi_i= 18^\circ$$

The trend of the line intersection is thus 190° and the plunge of the line of intersection is 18°.

Similar to the Suytucocha rock avalanche, the Trucha rock avalanche does not satisfy the kinematic criteria outlined for wedge failure, with a slope dip parallel to the line of intersection (ψ_{fi}) of 38°, a friction angle (ϕ) of 30° and a plunge of the line of intersection (ψ_i) of 18°:

$$\psi_{fi} > \psi_i > \phi \quad \text{[Equation 3. 3]}$$

$$38^\circ > 18^\circ < 30^\circ$$

The plunge of the line of intersection is not greater than the friction angle, which indicates that the point of intersection lies outside the wedge failure envelope.

The Trucha rock slope failure satisfies the criteria outlined for the trend of the line of intersection (α_i) and is within 20° of the dip direction of the slope (α_f):

$$(\alpha_f - 20°) \leq \alpha_i \leq (\alpha_f + 20°) \quad \text{[Equation 3. 4]}$$

$$(180° - 20°) \leq 190° \leq (180° + 20°)$$

$$160° \leq 190° \leq 200°$$

Lastly, Markland's Test indicates wedge sliding is occurring along both bedding B and joint set J1 at the Trucha rock avalanche, since neither the dip direction of B (α_B) or J1(α_{J1}) is situated between the trend of the line of intersection (α_i) and the dip direction of the slope (α_f):

$$\alpha_i > \alpha_B \text{ and/or } \alpha_{J1} > \alpha_f \quad \text{[Equation 3. 6]}$$

$$190° > 260° \text{ and/or } 111° > 180°$$

Based on the criteria outlined for wedge failure, it is not evident that the Trucha rock avalanche occurred due to wedge failure (Figure 3.25). The point of intersection lies outside the wedge failure envelope and does not satisfy the kinematic criteria. In order for the point of intersection of the two intersecting planes to fall within the wedge failure envelope, a friction angle less than 18° is required, which is much less than the value (30°) selected for the kinematic analysis.

3.4 Discussion of Conventional Wedge Failure Analyses

Field observations, discontinuity measurements and stereographic projections indicate the occurrence of wedge failures in all three of the sites studied. However, two of the three wedge failures studied, Suytucocha and Trucha, do not meet the kinematic criteria outlined for conventional wedge failure. In order for wedge failure to occur, the plunge of the line of intersection must be greater than the friction angle of the two discontinuities forming the wedge. This is not true for the Suytucocha and Trucha rock avalanche sites, where the plunge of the line of intersection was found to be 27° and 18° respectively, lower than the 30° friction angle assumed for the materials involved in the failures.

As a result, the point of intersection between the two discontinuities forming the wedge lies outside the friction circle of 30° and therefore lies outside the wedge failure envelope. In order for the wedge failure to occur at these two sites, the stereographic projection indicates that the friction angle would need to be significantly less than the values selected in order to meet the kinematic criteria. In the case of the Suytucocha rock avalanche, the friction angle would need to be less than 27° and in the case of the Trucha rock avalanche, the friction angle would need to be less than 18°. Although seismic shaking and/or water pressures may have contributed to a decrease in the friction angle at these two sites, it is considered highly unlikely that seismic shaking and/or water pressures would have decreased the friction angle by more than 12°, which is the requirement for wedge failure at the Trucha rock avalanche. Therefore,

another element must have facilitated wedge failure at these two sites besides the seismic shaking which occurred during the earthquake.

3.5 Stepped Wedge Failure

Field observations at the Suytucocha and Trucha rock avalanche sites clearly indicate the occurrence of wedge failure; rock mass fabric and topography geometry meet all the wedge failure criteria except for the kinematic criteria. In order to satisfy the conventional wedge failure kinematic criteria, either the friction angle would need to be significantly decreased or the line of intersection would need to be significantly increased. However, we explore the possibility that a steeper line of intersection facilitated the wedge failures at Suytucocha and Trucha.

It is evident from visual observations of these two wedge failures that the line of intersection is not a continuous line out of the slope but appears more as a stepped line of intersection, formed by the combination of a nearly-vertical dipping discontinuity, forming the backscarp, and a flatter dipping discontinuity roughly parallel to the dip direction of the slope. The steep dipping discontinuity may appear as a backscarp of the wedge failure while the flatter dipping discontinuity is interpreted to be the conventional line of intersection created by the two discontinuities forming the wedge. This combination of planar structural elements forms a stepped failure path where failure results from the combined mechanism of a main sliding discontinuity, dipping out of the slope, and, either separation along geologic discontinuities which are roughly perpendicular to the main discontinuity, or the tensile fracture of intact rock connecting the main discontinuities as has been suggested for stepped planar failure (Call and Savely, 1990; Call, 1992). In order to verify this hypothesis, the following criteria were developed for stepped wedge failure.

3.5.1 Stepped Wedge Shape Criteria

Similar to wedge failure, in order for stepped wedge failure to occur, two discontinuities within a rock mass need to intersect at a line, forming a line of intersection. In addition, a third discontinuity roughly parallel to the strike of the slope, dipping nearly-vertical into or out of the slope is required in order to form the first component of the stepped line of intersection. This discontinuity (which forms the backscarp in most cases), in combination with the conventional line of intersection, forms a new steeper stepped line of intersection which daylights in the slope. In addition, the backscarp acts as a release surface for wedge failure to occur. The shape of the stepped wedge appears differently from that of a typical wedge due to the presence of a prominent backscarp (Figure 3. 30).

Modifications can be made to the stereographic projection in order to show the stepped line of intersection. The stepped line of intersection was estimated based on the plunge and trend of the topographic center of the wedge. The topographic centre of the wedge was defined based on aerial photo interpretation and approximates the line at which the two intersecting discontinuities meet and exit out of the slope. A point which represents the plunge and trend of the topographic centre of the wedge that lies within the stepped wedge failure envelope is assumed to be the plunge and trend of the stepped line of intersection, and is termed the point of the stepped line of intersection (Figure 3. 31).

3.5.2 Stepped Wedge Kinematic Criteria

The kinematic criteria for conventional wedge failure can be revised for stepped wedge failure. In order to satisfy stepped wedge kinematic criteria, the slope parallel to the line of intersection (ψ_{fi}) must be greater than the plunge of the stepped line of intersection (ψ_{si}), which must be greater than the friction angle (ϕ) which is greater then the plunge of the conventional line of intersection (ψ_i) (Figure 3. 32):

$$\psi_{fi} > \psi_{si} > \phi > \psi_i \qquad \text{[Equation 3. 7]}$$

3.5.3 Stepped Wedge Trend Criteria

Similar to conventional wedge failure, in order for sliding of the stepped wedge to occur, the trend of the stepped line of intersection should plunge approximately parallel to the dip direction of the slope. The only difference between conventional wedge trend criteria and stepped wedge trend criteria is the substitution of the trend of the stepped line of intersection (α_{si}) for the trend of the conventional line of intersection (α_i). A range of ±20º of the dip direction of the slope (α_f) has been established to satisfy the trend criteria for the conventional line of intersection and should also satisfy the trend criteria for a stepped line of intersection (α_{si}) (Equation 3. 8) (Kliche, 1999):

$$(\alpha_f - 20^\circ) \leq \alpha_{si} \leq (\alpha_f + 20^\circ) \qquad \text{[Equation 3. 8]}$$

3.5.4 Markland's Test

Similar to conventional wedge failure, stereographic analysis can also determine whether sliding of a stepped wedge will occur on both wedge forming discontinuities, resulting in wedge failure, or on only one of the two, resulting in planar failure, a procedure referred to as Markland's Test (Hoek and Bray, 1977; Goodman 1976). Again, the only difference between Markland's Test for conventional wedge failure and Markland's Test for stepped wedge failure is the substitution of the trend of the stepped line of intersection (α_{si}) for the trend of the conventional line of intersection (α_i). In order to determine whether

the stepped wedge is sliding along both discontinuities or a single discontinuity, the following equations based on Hoek and Bray (1977) are used:

When the dip direction of the slope (α_f) is greater than the trend of the stepped line of intersection (α_{si}) if;

$\alpha_f > \alpha_A$ and/or $\alpha_B > \alpha_{si}$ [Equation 3. 9]

OR if the trend of the stepped line of intersection (α_{si}) is greater than the dip direction of the slope (α_f) if;

$\alpha_{si} > \alpha_A$ and/or $\alpha_B > \alpha_f$ [Equation 3. 10]

then if either the dip direction of discontinuity A (α_A) or the dip direction of discontinuity B (α_B) satisfies the criteria then sliding will occur along that plane in the direction of maximum dip resulting in planar failure. If both dip directions of discontinuity A and discontinuity B meet the criteria then sliding will occur along the plane whose dip direction is closest to the dip direction of the slope. However, if neither the dip direction of discontinuity A nor the dip direction of discontinuity B satisfies the criteria then sliding of the wedge will occur on both planes resulting in wedge failure along the stepped line of intersection.

3.6 Re-Evaluation of Case Histories Using Stepped Wedge Failure Criteria

Two of the three sites, Suytucocha and Trucha, which did not satisfy conventional wedge failure criteria, were re-evaluated using the stepped wedge failure criteria developed above.

3.6.1 Suytucocha Rock Avalanche

In order for stepped wedge failure to occur at the Suytucocha rock avalanche site, three criteria for stepped wedge failure must be met. Suytucocha satisfies the stepped wedge shape criteria, since bedding B and joint set J1 intersect. The trend (α_{si}) and plunge (ψ_{si}) of the stepped line of intersection of bedding B and joint set J1 can be determined by estimating the trend and plunge of the topographic center of the wedge indicated by the point of the stepped line of intersection. The point of the stepped line intersection indicates a trend of 163° and a plunge of 39° (Figure 3. 33).

Suytucocha satisfies the stepped wedge criteria outlined for kinematic criteria, with a slope dip parallel to the stepped line of intersection (ψ_{fi}) of 40°, a plunge for the stepped line of intersection (ψ_{si}) of 39°, a friction angle (ϕ) of 30° and a plunge for the conventional line of intersection (ψ_i) of 27°:

$\psi_{fi} > \psi_{si} > \phi > \psi_i$ [Equation 3. 7]

$40° > 39° > 30° > 27°$

Therefore, the stepped line of intersection daylights in the slope and plunges at a greater angle than the friction angle of the two intersecting discontinuities.

Suytucocha also satisfies the criteria outlined for the stepped wedge trend criteria. The trend of the stepped line of intersection (α_{si}) is within 20° of the dip direction of the slope (α_f):

$$(\alpha_f - 20°) \leq \alpha_{si} \leq (\alpha_f + 20°) \quad \text{[Equation 3. 8]}$$

$$(152° - 20°) \leq 163° \leq (152° + 20°)$$

$$132° \leq 163° \leq 172°$$

Lastly, Markland's Test for stepped wedge criteria indicates that sliding of the wedge is still occurring along both bedding B and joint set J1 at the Suytucocha rock avalanche, since neither the dip direction of bedding B (α_B) nor the dip direction of joint set J1 (α_{J1}) is situated between the trend of the stepped line of intersection (α_{si}) and the dip direction of the slope (α_f):

$$\alpha_{si} > \alpha_B \text{ and/or } \alpha_{J1} > \alpha_f \quad \text{[Equation 3. 10]}$$

$$163° > 219° \text{ and/or } 90° > 152°$$

Based on the criteria outlined for stepped wedge failure, the analysis suggests that the Suytucocha rock avalanche occurred due to stepped wedge failure (Figure 3. 33). The point assumed to represent the plunge and trend of the stepped line of intersection (the plunge and trend of the topographic centre of the wedge) lies within the stepped wedge failure envelope. Thus the stepped wedge kinematic criteria is satisfied. The stereonet (Figure 3. 33) also shows J2 striking roughly parallel to the slope, dipping nearly-vertical, which aids in release of the wedge block. As a result, stepped wedge failure is indicated at Suytucocha with the intersection of the bedding (B) and joint set 1 (J1), with a moderately steep stepped line of intersection dipping in a south direction out of the slope.

3.6.2 Trucha Rock Avalanche

In order for stepped wedge failure to occur at the Trucha rock avalanche site, three criteria for stepped wedge failure must be met. The Trucha rock avalanche satisfies the stepped wedge shape criteria, since bedding B and joint set J1 intersect. The trend (α_{si}) and plunge (ψ_{si}) of the stepped line of intersection of B and J1 can be determined by estimating the plunge and trend of the topographic center of the wedge indicated by the point representing the orientation of the stepped line of intersection. The point of the stepped line of intersection indicates a trend of 185° and a plunge of 32° (Figure 3. 34).

The Trucha rock avalanche satisfies the stepped wedge criteria outlined for the kinematic criteria, with a slope dip parallel to the stepped line of intersection (ψ_{fi}) of 38°, a plunge for the stepped line of intersection (ψ_{si}) of 32°, a friction angle (ϕ) of 30° and a plunge for the conventional line of intersection (ψ_i) of 18°:

$$\psi_{fi} > \psi_{si} > \phi > \psi_i \qquad \text{[Equation 3. 7]}$$

$$38° > 32° > 30° > 18°$$

Therefore, the stepped line of intersection daylights in the slope and its plunge exceeds the friction angle of the two intersecting discontinuities.

Trucha satisfies the criteria outlined for the stepped wedge trend criteria. The stepped line of intersection (α_{si}) is within 20° degrees of the dip direction of the slope (α_f):

$$(\alpha_f - 20°) \leq \alpha_{si} \leq (\alpha_f + 20°) \qquad \text{[Equation 3. 8]}$$

$$(180° - 20°) \leq 185° \leq (180° + 20°)$$

$$160° \leq 185° \leq 200°$$

Lastly, Markland's Test indicates that sliding of the wedge is still occurring along both B and J1 at the Trucha rock avalanche, since neither the dip direction of bedding B (α_B) nor the dip direction of joint set J1 (α_{J1}) is situated between the trend of the stepped line of intersection (α_{si}) and the dip direction of the slope (α_f):

$$\alpha_{si} > \alpha_B \text{ and/or } \alpha_{J1} > \alpha_f \qquad \text{[Equation 3. 10]}$$

$$185° > 260° \text{ and/or } 111° > 180°$$

Based on the criteria outlined for stepped wedge failure, the analysis indicates that the Trucha rock avalanche occurred due to wedge failure along a stepped line of intersection (Figure 3. 34). The point assumed to be the plunge and trend of the stepped line of intersection lies within the stepped wedge failure envelope. Thus the stepped wedge kinematic criteria is satisfied. The stereonet (Figure 3. 34) also shows J2 striking roughly parallel to the slope, dipping nearly-vertical, which aids in release of the wedge block. As a result, stepped wedge failure at the Trucha rock avalanche resulted from the intersection of the bedding (B) and joint set 1 (J1), with a moderately steep stepped line of intersection dipping in a south direction out of the slope.

3.7 Discussion of Stepped Wedge Failures in Ancash

In addition to the newly developed criteria for stepped wedge failure, five general characteristics which appear typical of the stepped wedge failures studied can be distinguished.

1) All three of the rock avalanches investigated in detail, appear to have similar topography which facilitates the occurrence of stepped wedge failure. Stepped wedge failures occur along the sides of valleys where the dip direction of bedding planes run parallel to the orientation of the valleys, i.e. the strike of the bedding planes is perpendicular to the orientation of the valley. This is clearly evident at both the Suytucocha and Trucha rock avalanche sites.

2) Stepped wedge failures occur along valleys which are transverse to the dominant northwest-southeast structural features in the epicentral region along the continental divide. In addition to the Suytucocha and Trucha rock avalanches, a series of wedge failures were observed within this region at the Blanca rock avalanches (Figure 3. 35).

3) In order to accommodate the daylighting of a steeper stepped line of intersection, a steep slope is needed in order to satisfy the stepped wedge kinematic criteria. Of the two stepped wedge failure sites studied, the average slope ranged from 38° to 40°. A steep slope is thus essential in the development of a stepped wedge because it allows the stepped line of intersection to daylight in the slope.

4) The stepped line of intersection is formed through the combination of the conventional line of intersection and a nearly-vertical dipping discontinuity parallel to the strike of the slope, which forms the backscarp of the stepped wedge. Prominent backscarps were evident at both the Suytucocha and Trucha rock avalanches.

5) Stepped wedge failure is facilitated by very steep bedding planes which act as one of the intersecting discontinuities needed for stepped wedge shape criteria. The dip of the bedding planes at the Suytucocha and Trucha rock avalanches ranged from 37° to 44°.

Although, the Camino Peligroso rock avalanche met the criteria for conventional wedge failure, it is possible that it would also meet the stepped wedge criteria because it has many similar characteristics of a stepped wedge failure. Unfortunately, the topographic centre of the wedge could not be estimated and it could not be confirmed as a stepped wedge failure. Therefore, the Camino Peligroso rock avalanche could be considered a transitional case which satisfies both wedge failure and stepped wedge failure criteria.

3.8 Conclusions

The three rock avalanches studied offer much insight into the mechanism of wedge failure. Only the Camino Peligroso rock avalanche met the conventional wedge failure criteria, while the Suytucocha and Trucha rock avalanches did not. Further observation of the Suytucocha and Trucha rock avalanches suggested that a steeper stepped line of intersection was required in order for wedge failure to occur. This is termed stepped wedge failure. Criteria were developed for stepped wedge failure based on the topography and rock mass fabric of the two field sites studied. In addition to the newly developed stepped wedge failure criteria, additional characteristics associated with stepped wedge failure were noted. These include the occurrence of stepped wedge failures along transverse valleys where the dip of the bedding is parallel to the trend of the valley. Most importantly, a steep source slope is required for the stepper stepped line of intersection to daylight in the slope and a nearly-vertical discontinuity roughly parallel to the slope allows the formation of a stepped line of intersection in conjunction with the conventional line of intersection. Lastly, the steep dip (>35°) of the bedding planes involved in wedge shape development facilitates stepped wedge failure.

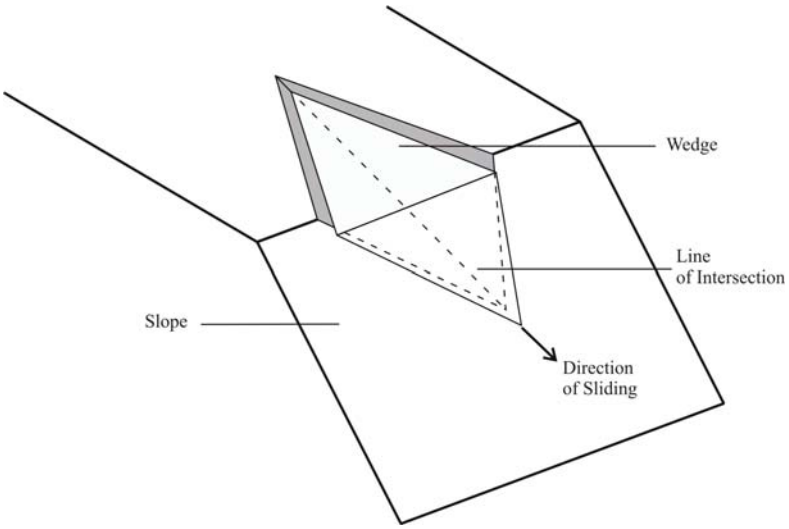

Figure 3. 1: Schematic sketch of conventional wedge failure showing wedge formed by intersecting discontinuities sliding out of the slope along the line of intersection

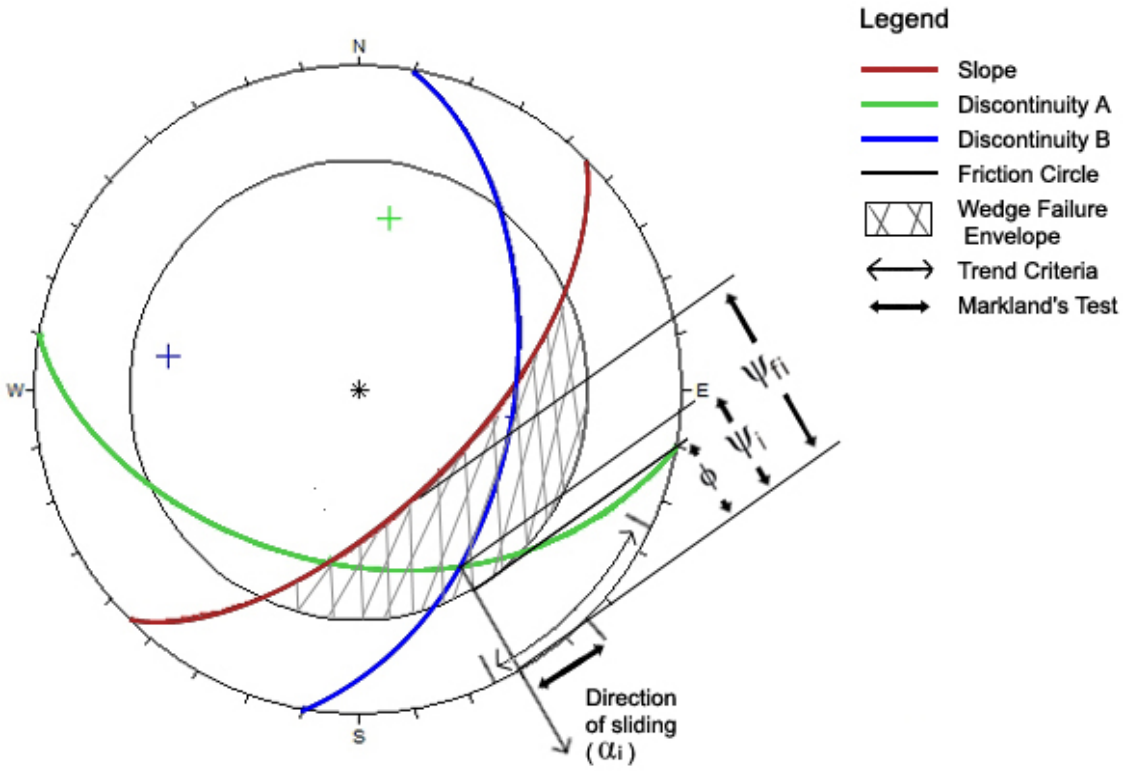

Figure 3. 2: Lower hemisphere of equal area stereographic projection showing kinematic analysis of conventional wedge failure

The dip of the slope parallel to the line of intersection (ψ_{fi}), angle of friction (ϕ), plunge (ψ_i) and trend (α_i) of the line of intersection are shown.

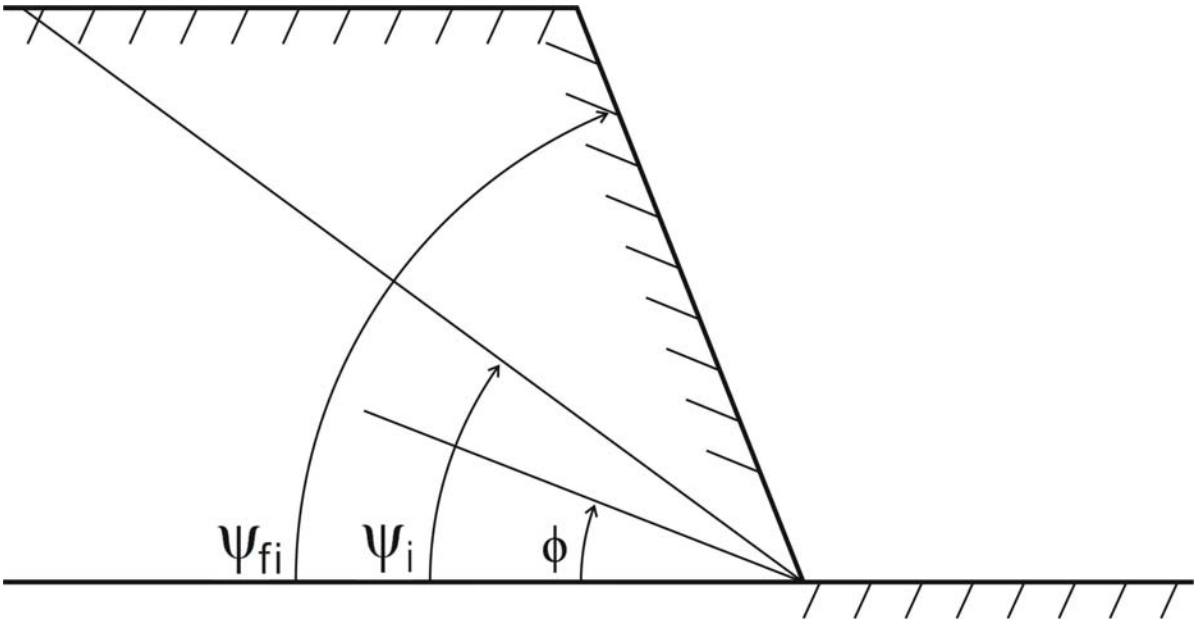

Figure 3. 3: Cross-section of slope parallel to the line of intersection for conventional wedge failure

Dip of the slope parallel to the line of intersection (ψ_{fi}) is greater than the plunge of the line of intersection (ψ_i) which is greater than the angle of friction (ϕ).

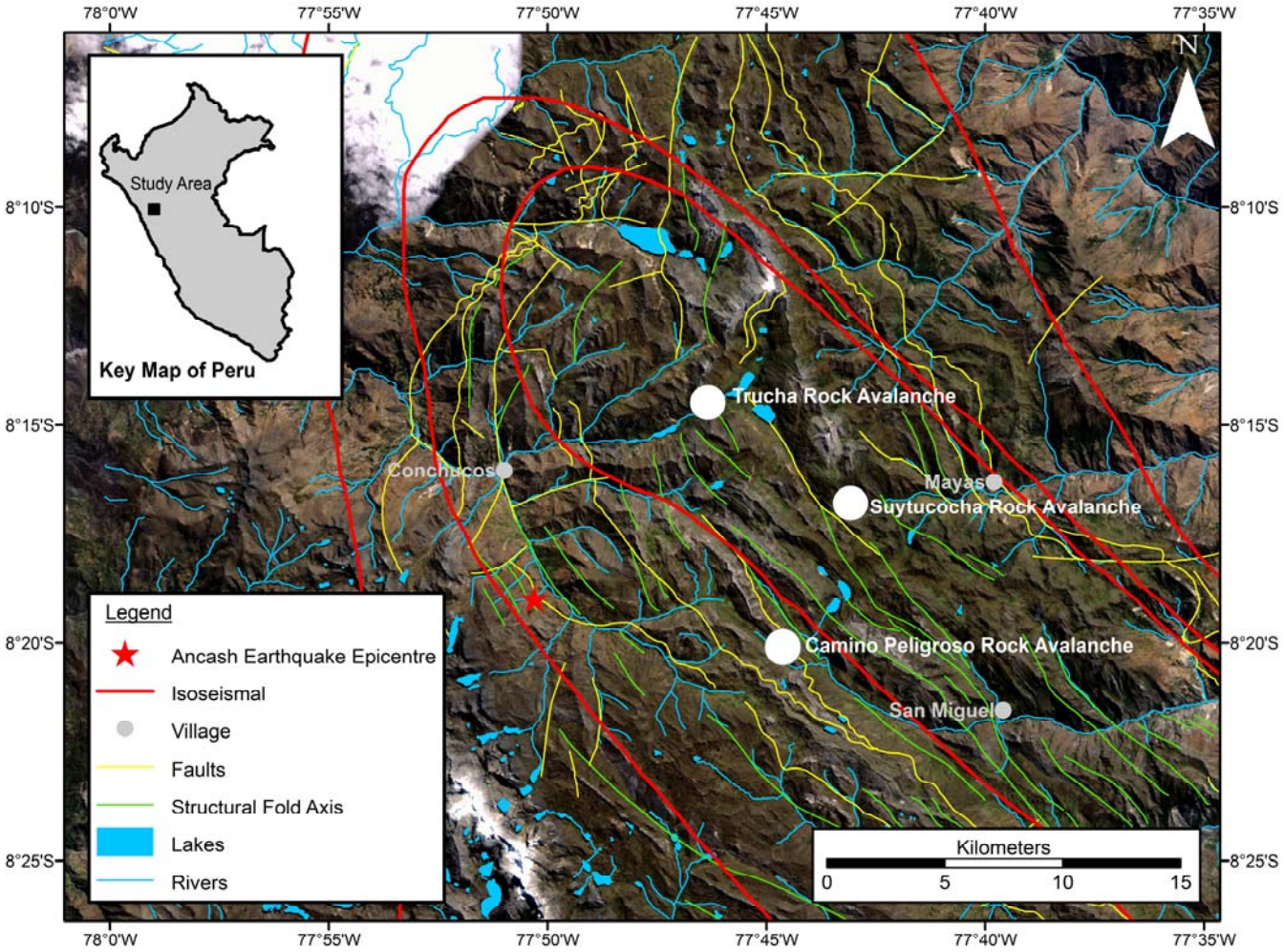

Figure 3. 4: Map showing the location of the Camino Peligroso, Suytucocha and Trucha rock avalanches

The 1946 Ancash earthquake epicenter and isoseismal intensities (Silgado, 1951) are shown. Faults (yellow) and structural fold axes (green) are also shown (Sanchez Fernandez, 1995).

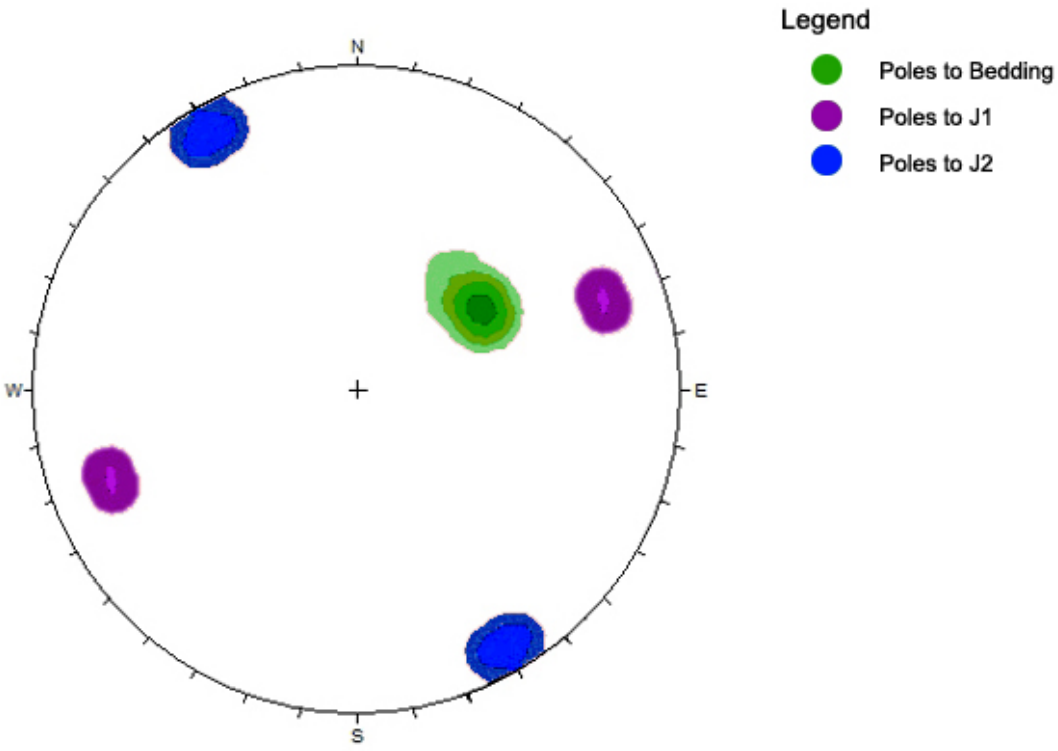

Figure 3. 5: Conceptual stereographic projection for rock mass fabric in Cretaceous sedimentary rocks in the epicentral region of the 1946 Ancash earthquake

The projection shows poles to southwest dipping bedding, poles to northeast/southwest dipping joint set J1 and poles to northwest/southeast dipping joint set J2.

Figure 3. 6: View of Camino Peligroso rock avalanche, looking northeast showing southwest dipping bedding planes

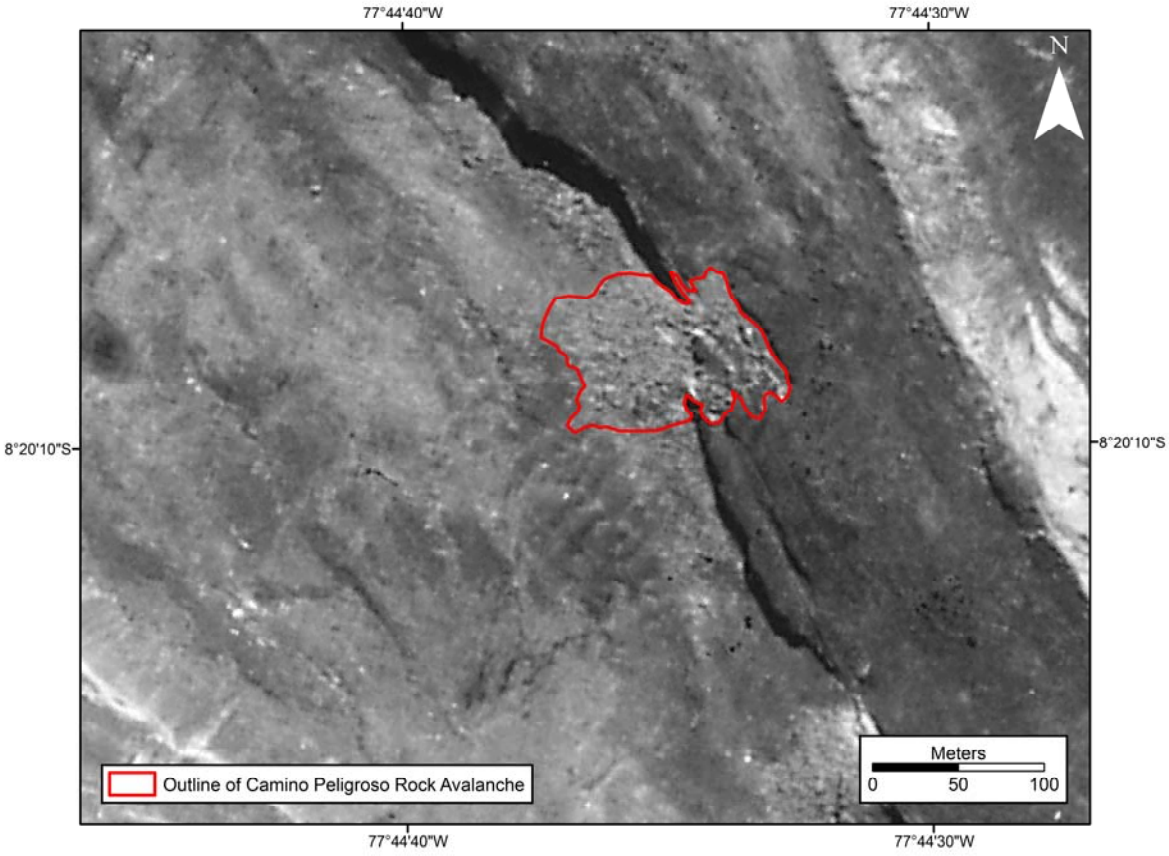

Figure 3. 7: Aerial photograph (1370PMW-MWM156-20030) of the Camino Peligroso rock avalanche

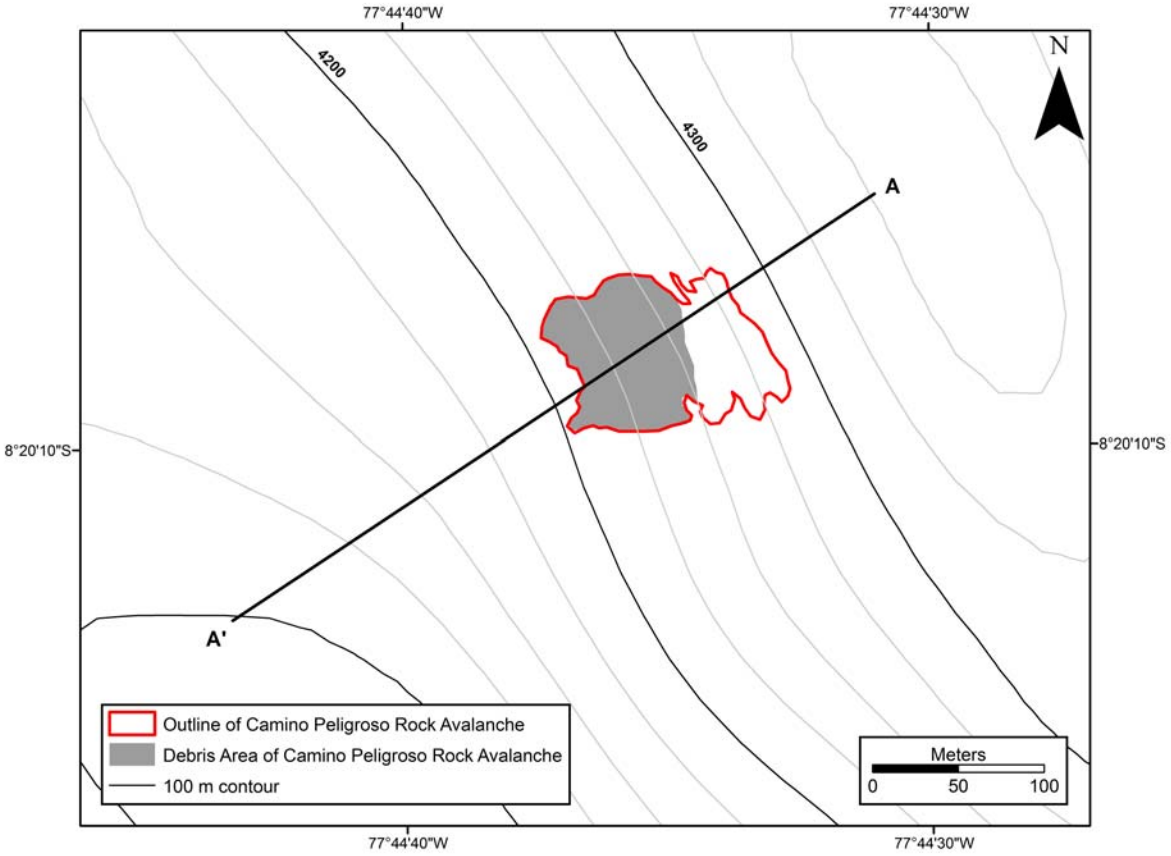

Figure 3. 8: **Contour map of the Camino Peligroso rock avalanche showing slope profile from A-A'.**

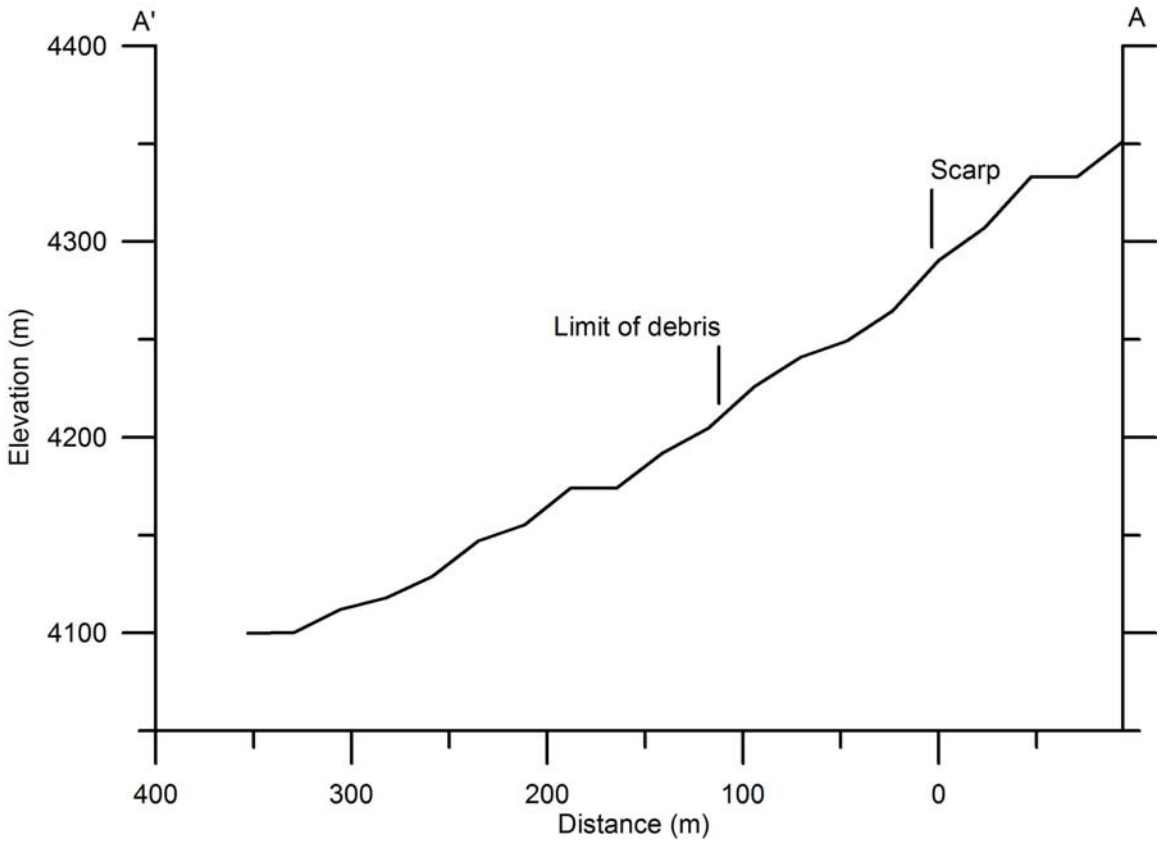

Figure 3. 9: Slope profile from A-A' at Camino Peligroso rock avalanche site showing the location of the slide scarp and the limit of debris

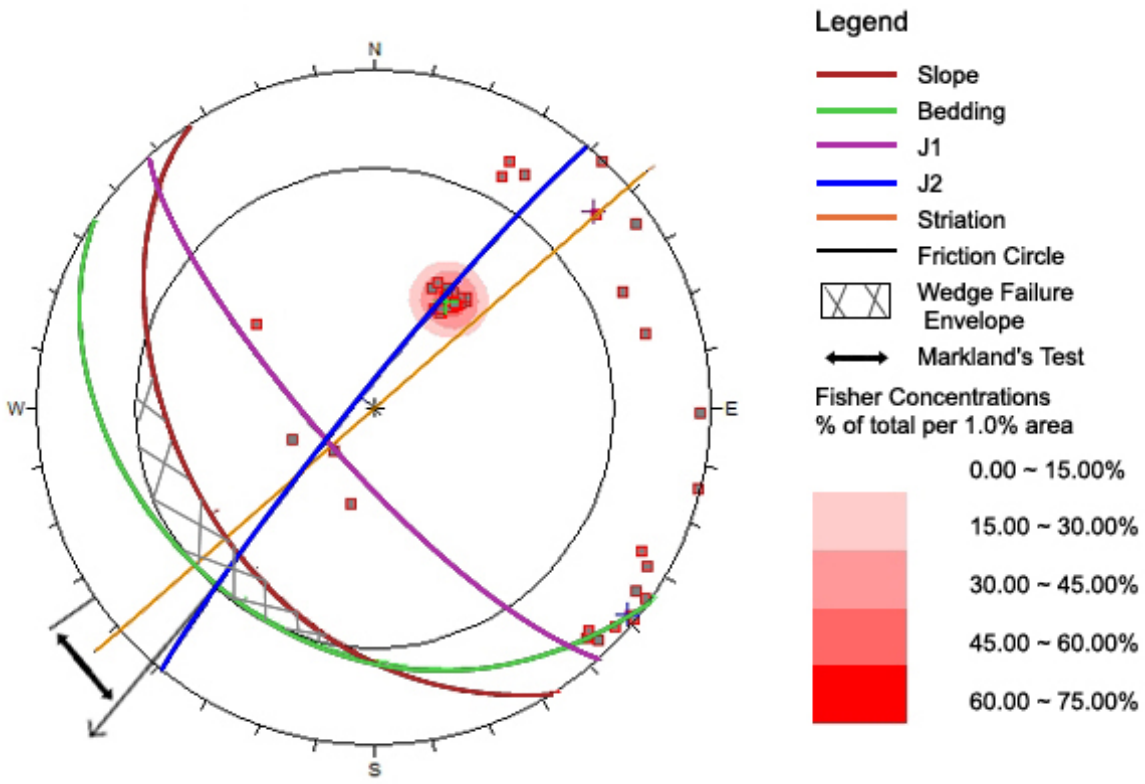

Figure 3. 10: Undisturbed rock fabric at the Camino Peligroso rock avalanche site – wedge failure

Poles and contours of 52 discontinuities are plotted on a lower hemisphere of equal area stereographic projection. Discontinuity sets are bedding, J1 and J2. Slope, striation and friction circle are indicated. Conventional wedge failure envelope is shown in hatched area. The direction of wedge failure is indicated by the arrow pointing to the southwest.

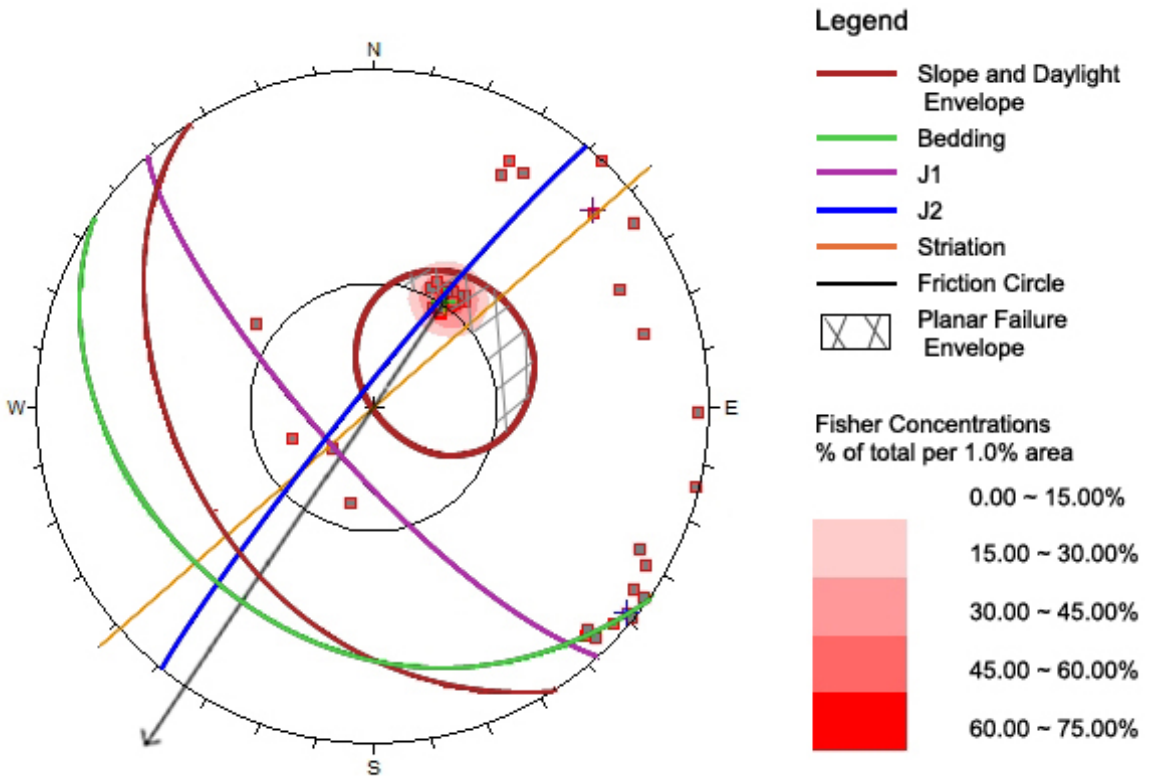

Figure 3. 11: Undisturbed rock fabric at Camino Peligroso rock avalanche site – planar failure

Poles and contours of 52 discontinuities are plotted on a lower hemisphere of equal area stereographic projection. Discontinuity sets are bedding, J1 and J2. Slope, daylight envelope, striation and friction circle are indicated. Planar failure envelope is shown in hatched area. The direction of potential planar failure is indicated by the arrow pointing to the southwest and corresponds to the direction of true dip of the bedding. Note that the strike of J2 is more or less parallel to the true dip direction. Also note the orientation of the striation on the sliding surface indicates a trend to the west of the true dip direction indicating the influence of J2 in "guiding" the failure.

Figure 3. 12: View of the source of the Suytucocha rock avalanche, looking north

Wedge is formed by southwest dipping bedding (at right) and nearly-vertical east dipping joint set J1 (at left). The backscarp is formed by northwest dipping joint set J2.

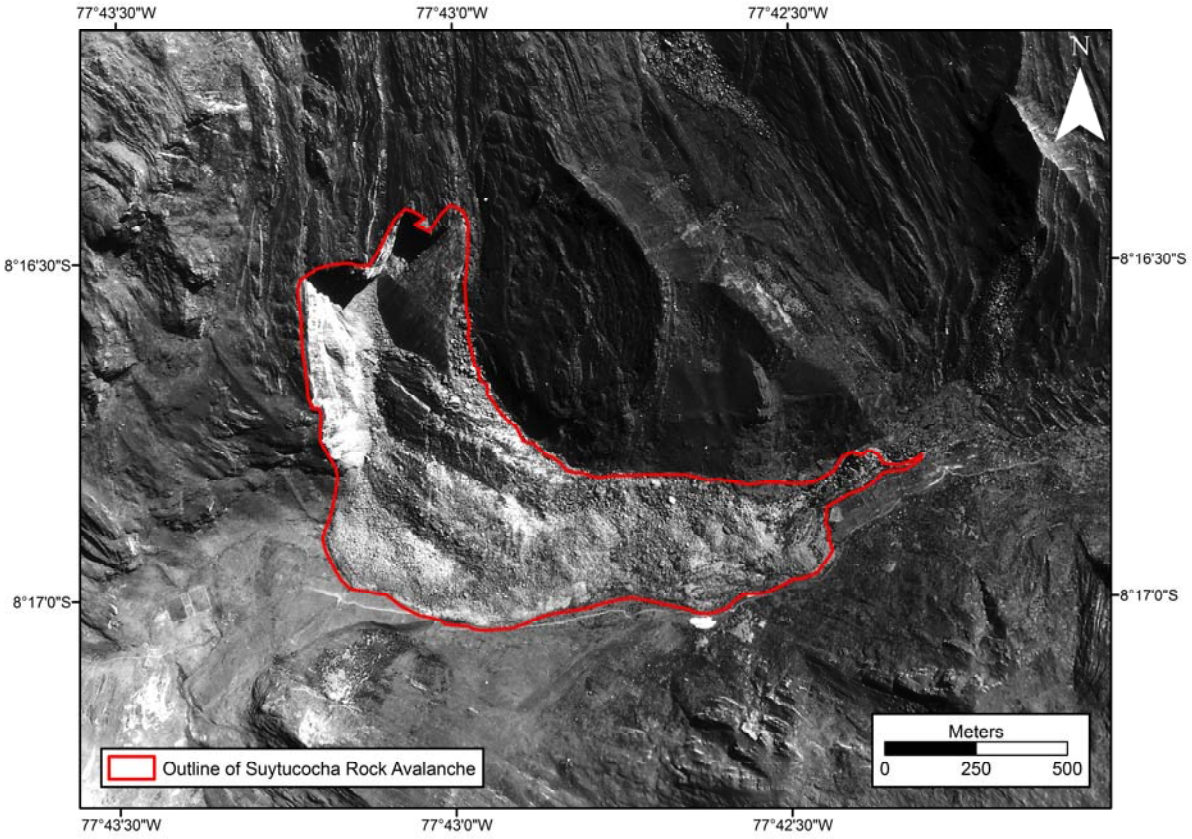

Figure 3. 13: Aerial photograph (1370PMW-MWM130-16416) of the Suytucocha rock avalanche

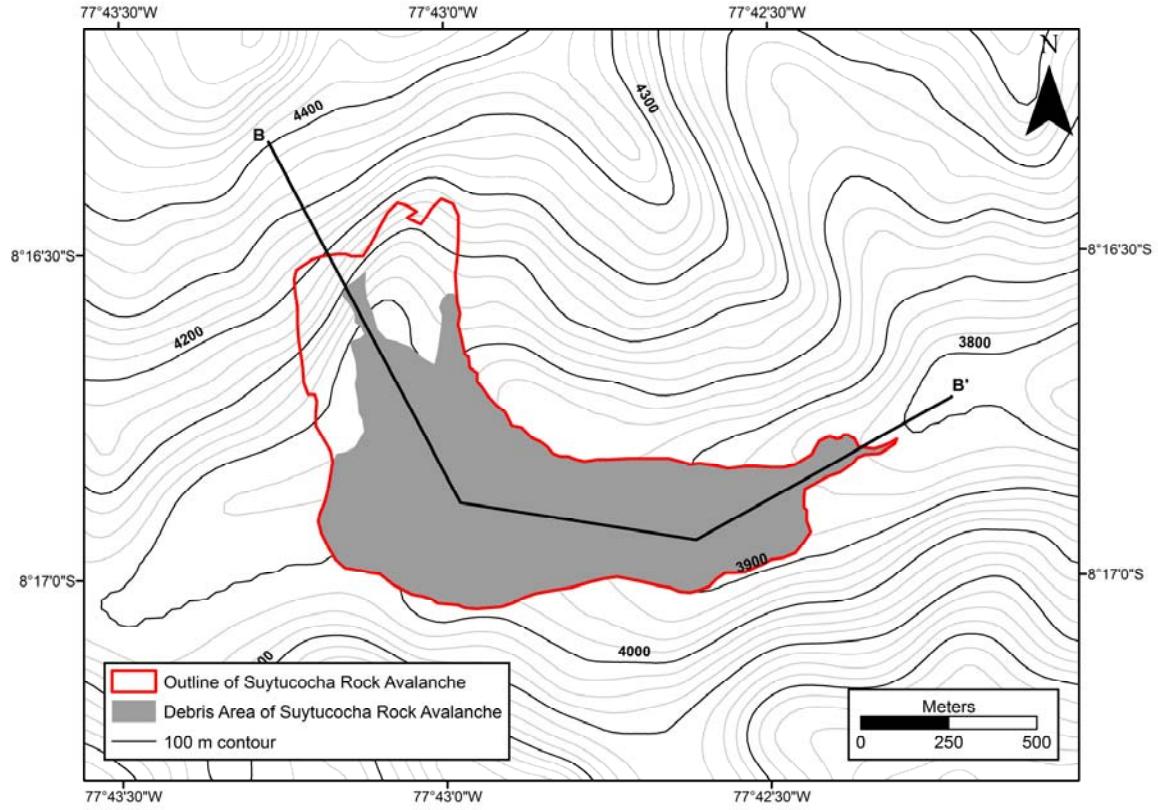

Figure 3. 14: Contour map of the Suytucocha rock avalanche showing slope profile from B-B'

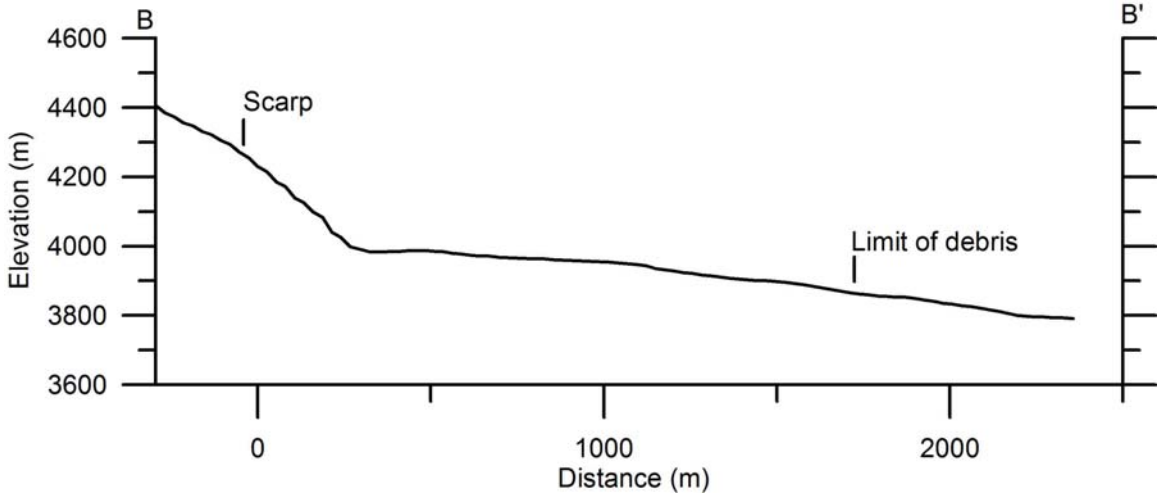

Figure 3. 15: Slope profile from B-B' at the Suytucocha rock avalanche site showing the location of the slide scarp and the limit of debris

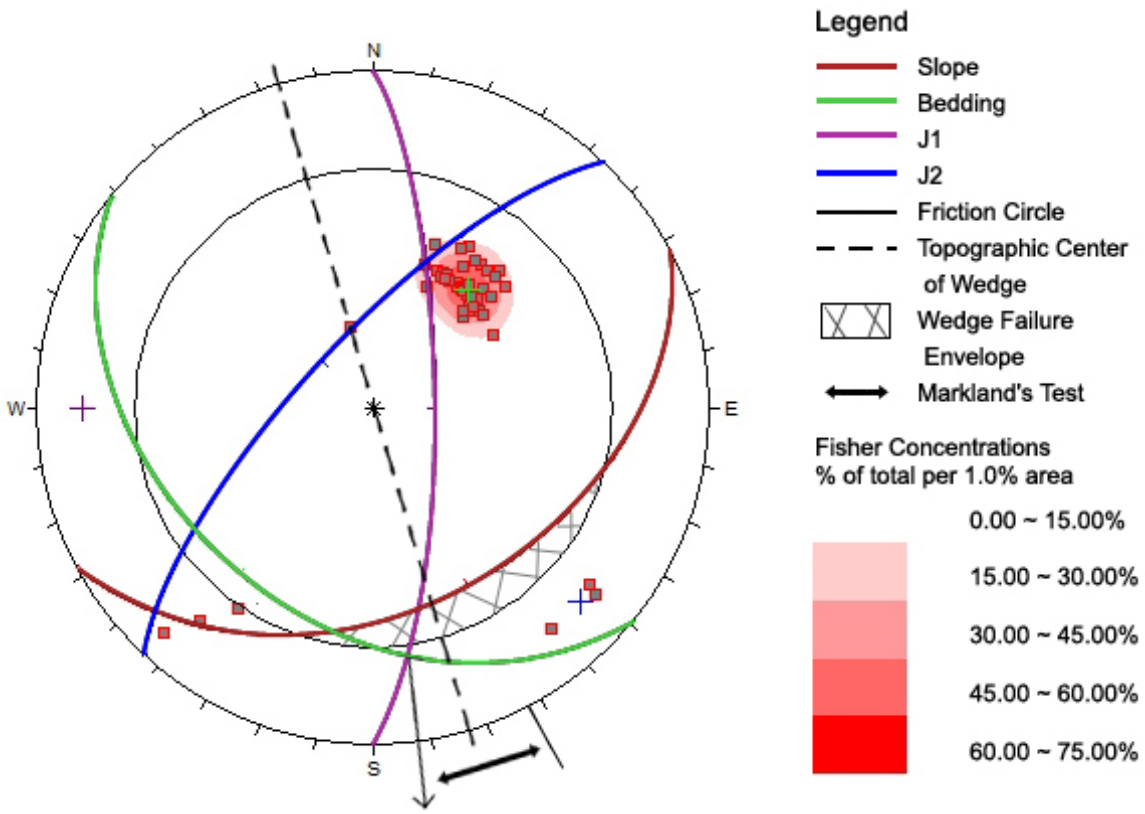

Figure 3. 16: Undisturbed rock fabric at Suytucocha rock avalanche site – wedge failure

Poles and contours of 47 discontinuities are plotted on a lower hemisphere of equal area stereographic projection. Discontinuity sets are bedding, J1 and J2. Slope, friction circle and topographic center of wedge are indicated. Conventional wedge failure envelope is shown in hatched area. The direction of wedge failure is indicated by the arrow pointing to the south.

Figure 3. 17: View of southwest dipping bedding plane at Suytucocha rock avalanche, looking north

Figure 3. 18: View of nearly-vertical east dipping joint set J1 at Suytucocha rock avalanche, looking northwest

Figure 3. 19: View of northwest dipping joint set J2 forming backscarp at Suytucocha rock avalanche, looking north

Figure 3. 20: View of bedding plane, J1 and J2 at Suytucocha rock avalanche, looking north

Figure 3. 21: View of Trucha rock avalanche, looking north

Wedge is formed by west dipping bedding plane and east dipping joint set J1. The backscarp is formed by nearly-vertical south dipping joint set J2.

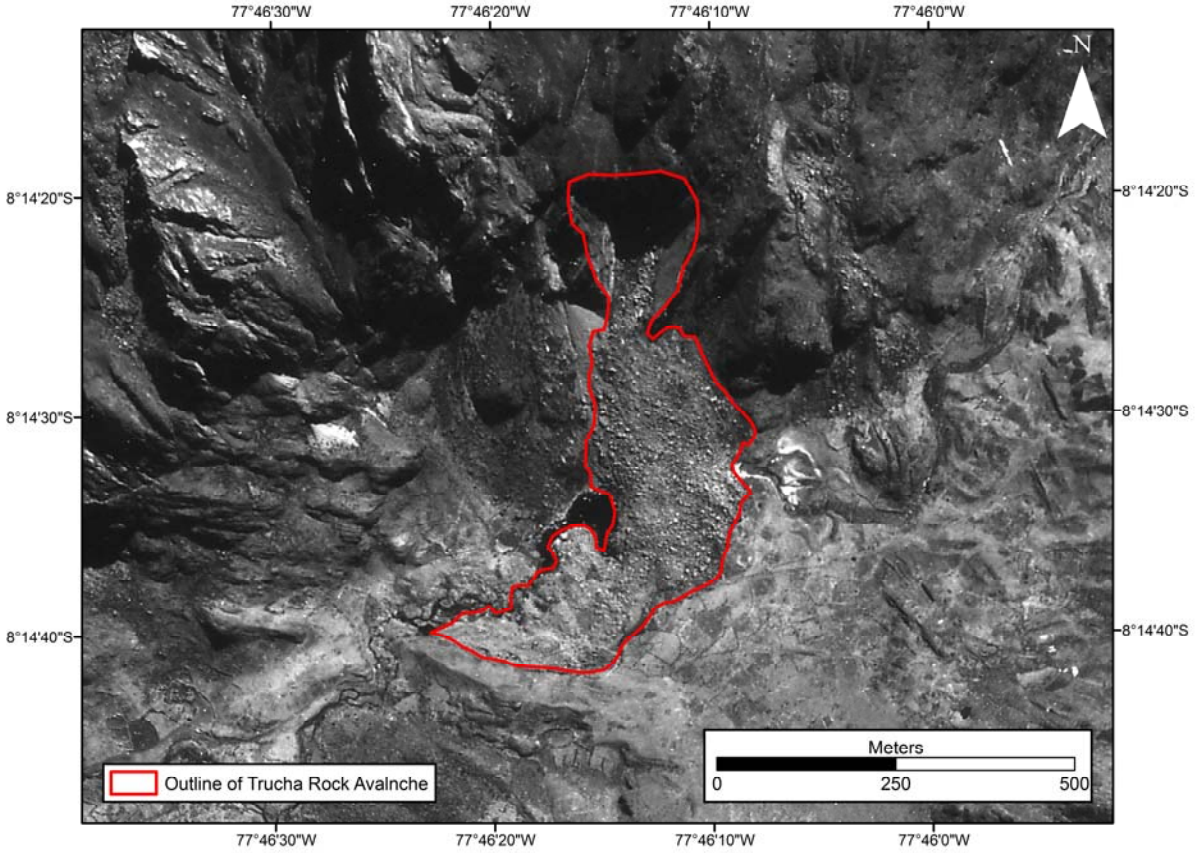

Figure 3. 22: Aerial photograph (1370PMW-MWM156-20027) of the Trucha rock avalanche

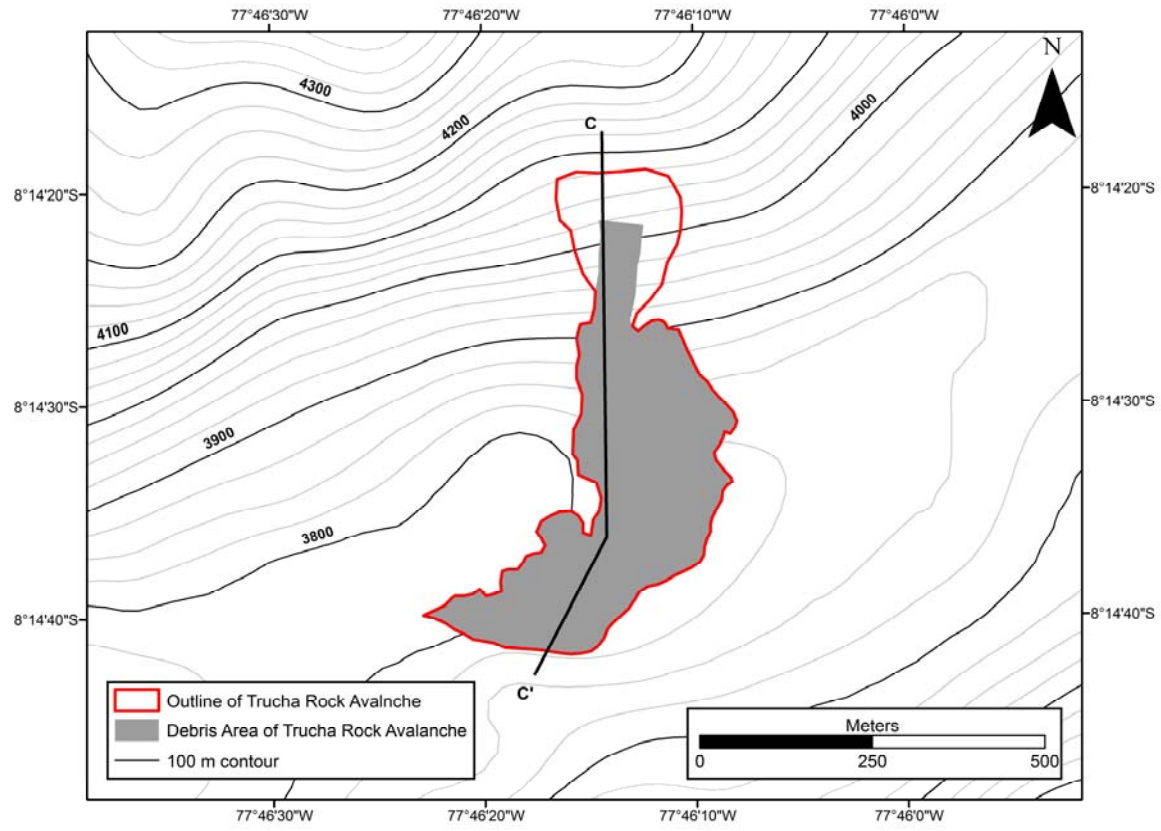

Figure 3. 23: Contour map of the Trucha rock avalanche showing slope profile from C-C'

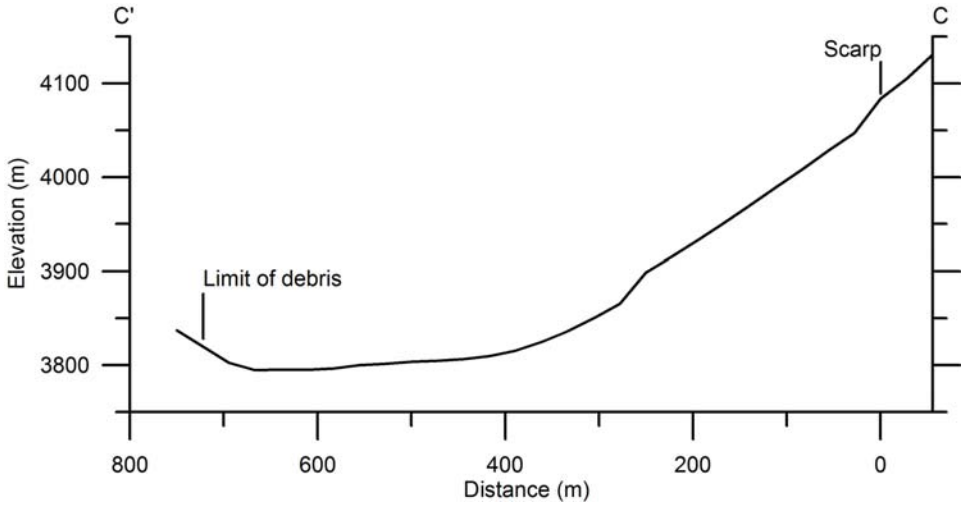

Figure 3. 24: Slope profile from C-C' at the Trucha rock avalanche site showing the location of the slide scarp and the limit of debris

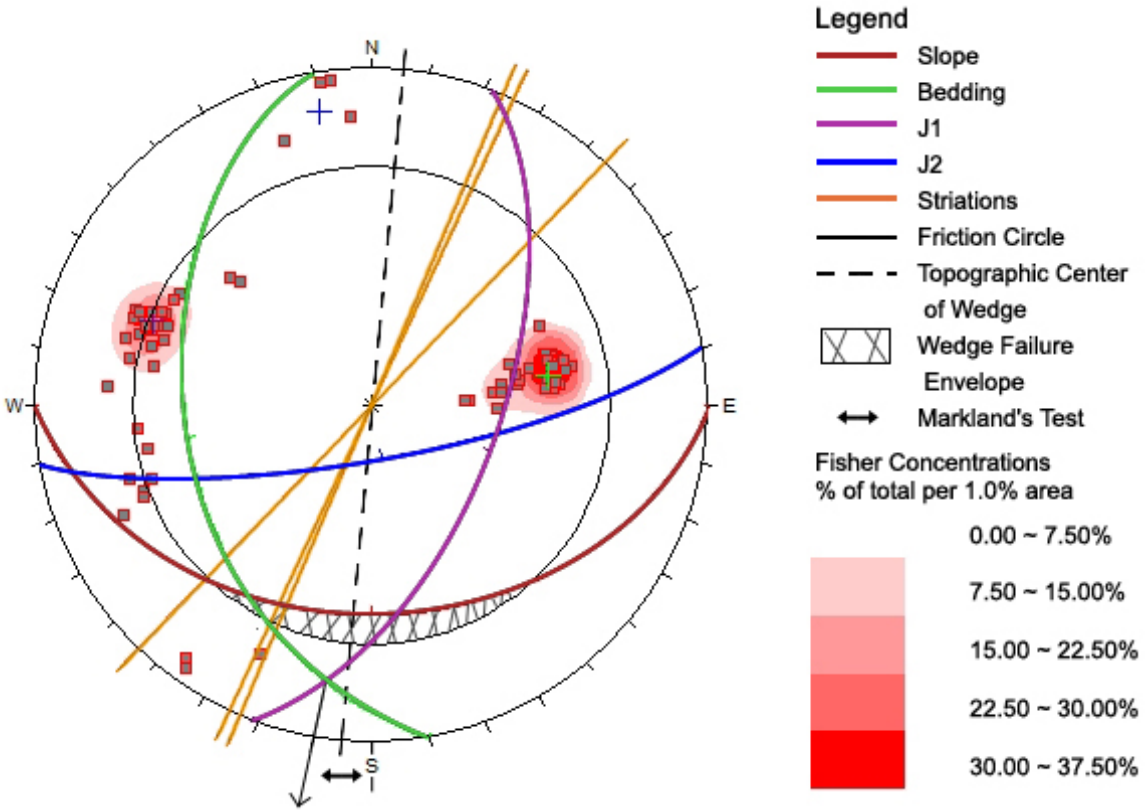

Figure 3. 25: Undisturbed rock fabric at the Trucha rock avalanche site – wedge failure

Poles and contours of 82 discontinuities are plotted on a lower hemisphere of equal area stereographic projection. Discontinuity sets are bedding, J1 and J2. Slope, striations, friction circle and topographic center of wedge are indicated. Conventional wedge failure envelope is shown in hatched area. The direction of wedge failure is indicated by the arrow pointing to the south.

Figure 3. 26: View of west dipping bedding plane at Trucha rock avalanche, looking northeast

Figure 3. 27: View of east dipping joint set J1 at Trucha rock avalanche, looking northwest

Figure 3. 28: View of nearly-vertical south dipping joint set J2 forming backscarp at Trucha rock avalanche, looking north

Figure 3. 29: View of bedding, J1 and J2 at Trucha rock avalanche, looking northwest

Compare to Figure 3. 25.

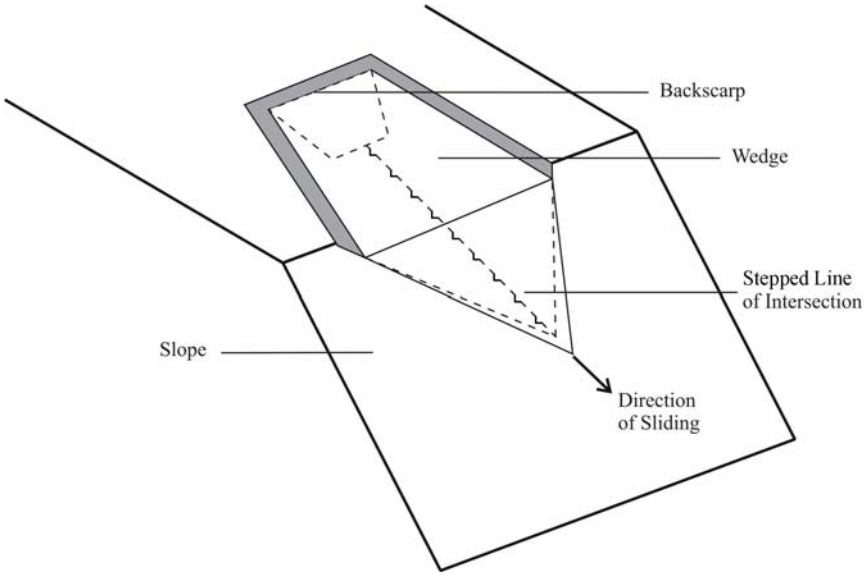

Figure 3. 30: Schematic sketch of stepped wedge failure

Wedge formed by intersecting discontinuities and backscarp sliding out of the slope along the stepped line of intersection.

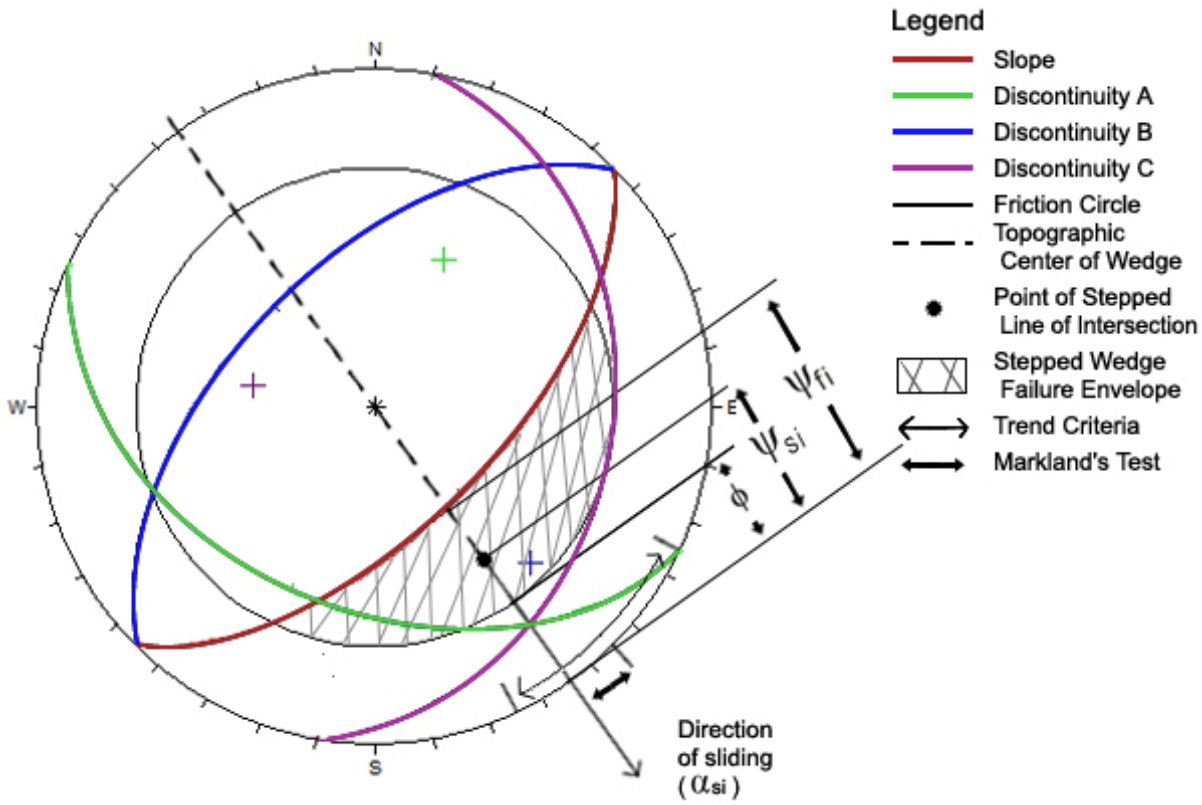

Figure 3. 31: Lower hemisphere of equal area stereographic projection showing stepped wedge failure criteria

The dip of the slope parallel to the line of intersection (ψ_{fi}), angle of friction (ϕ), plunge (ψ_{si}) and trend (α_{si}) of the stepped line of intersection are shown. Note the point of stepped line of intersection which represents the plunge and trend of the stepped line of intersection**.**

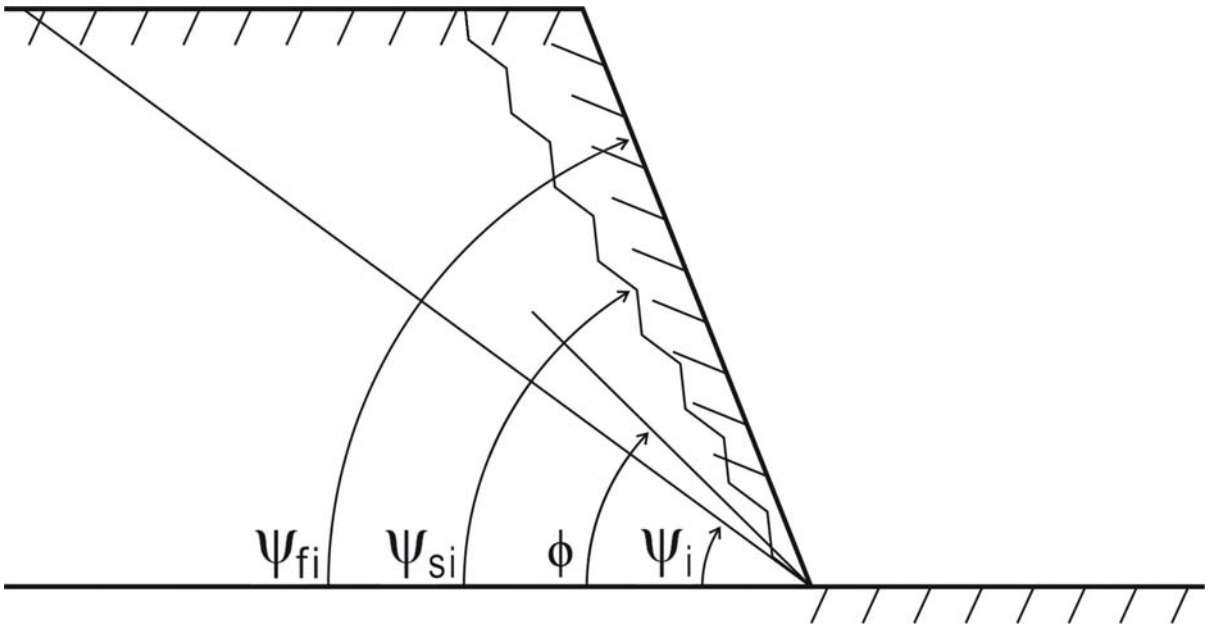

Figure 3. 32: Cross-sectional sketch of slope parallel to the line of intersection illustrating stepped wedge failure.

Dip of the slope parallel to the line of intersection (ψ_{fi}) is greater than the plunge of the stepped line of intersection (ψ_{si}) which is greater than the angle of friction (ϕ) which is greater than the plunge of the conventional line of intersection (ψ_i).

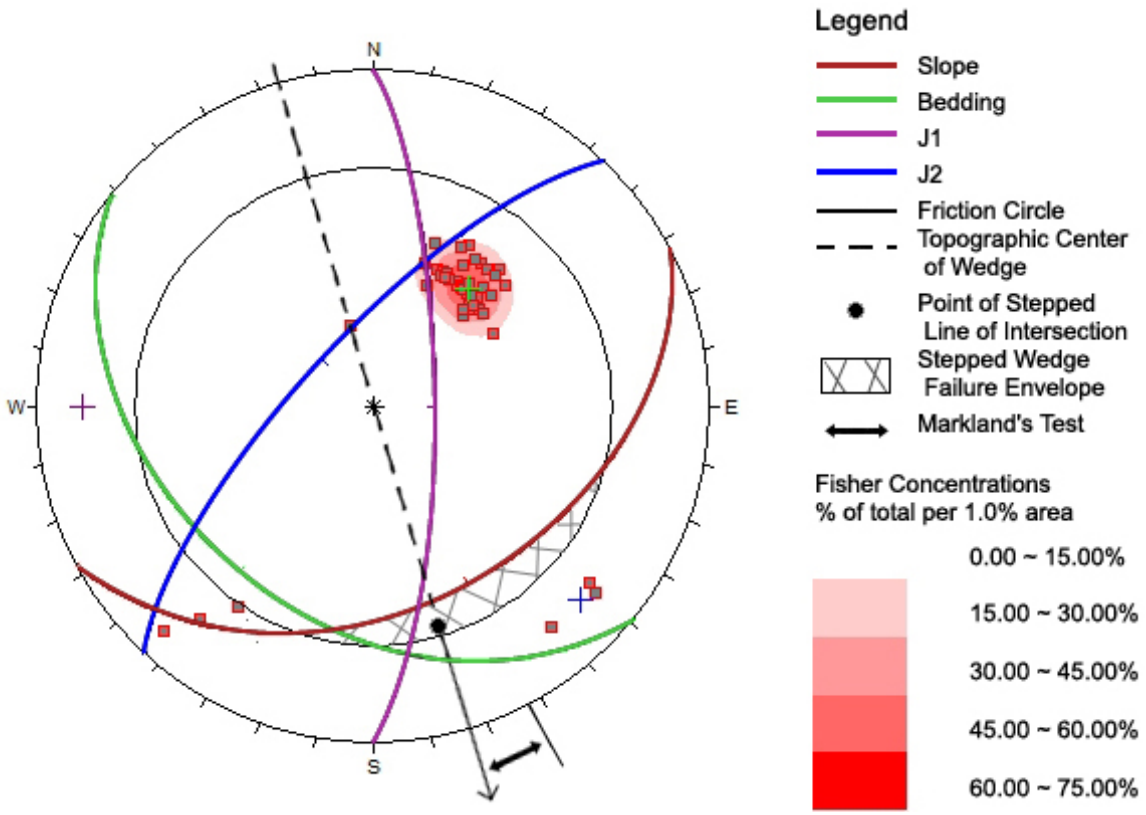

Figure 3. 33: Undisturbed rock fabric at Suytucocha rock avalanche site – stepped wedge failure

Poles and contours of 47 discontinuities are plotted on a lower hemisphere of equal area stereographic projection. Discontinuity sets are bedding, J1 and J2. Slope, friction circle and topographic center of wedge are indicated. Stepped wedge failure envelope is shown in hatched area. The point of stepped line of intersection represents the plunge and trend of the stepped line of intersection and corresponds to the plunge and trend of the topographic centre of the wedge. The direction of wedge failure is indicated by the arrow pointing to the southeast.

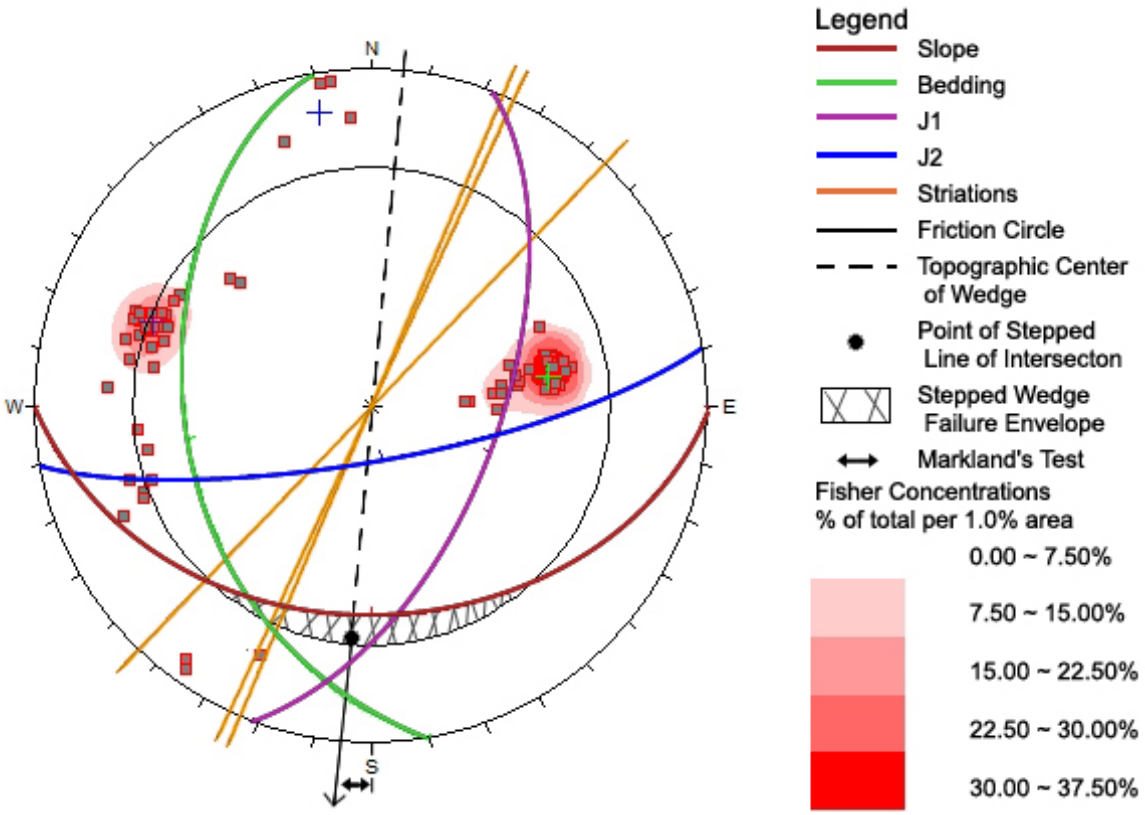

Figure 3. 34: Undisturbed rock fabric at Trucha rock avalanche site – stepped wedge failure

Poles and contours of 82 discontinuities are plotted on a lower hemisphere of equal area stereographic projection. Discontinuity sets are bedding, J1 and J2. Slope, striations, friction circle and topographic center of wedge are indicated. Stepped wedge failure envelope is shown in hatched area. The point of stepped line of intersection represents the plunge and trend of the stepped line of intersection and corresponds to the plunge and trend of the topographic centre of the wedge. The direction of wedge failure is indicated by the arrow pointing to the south.

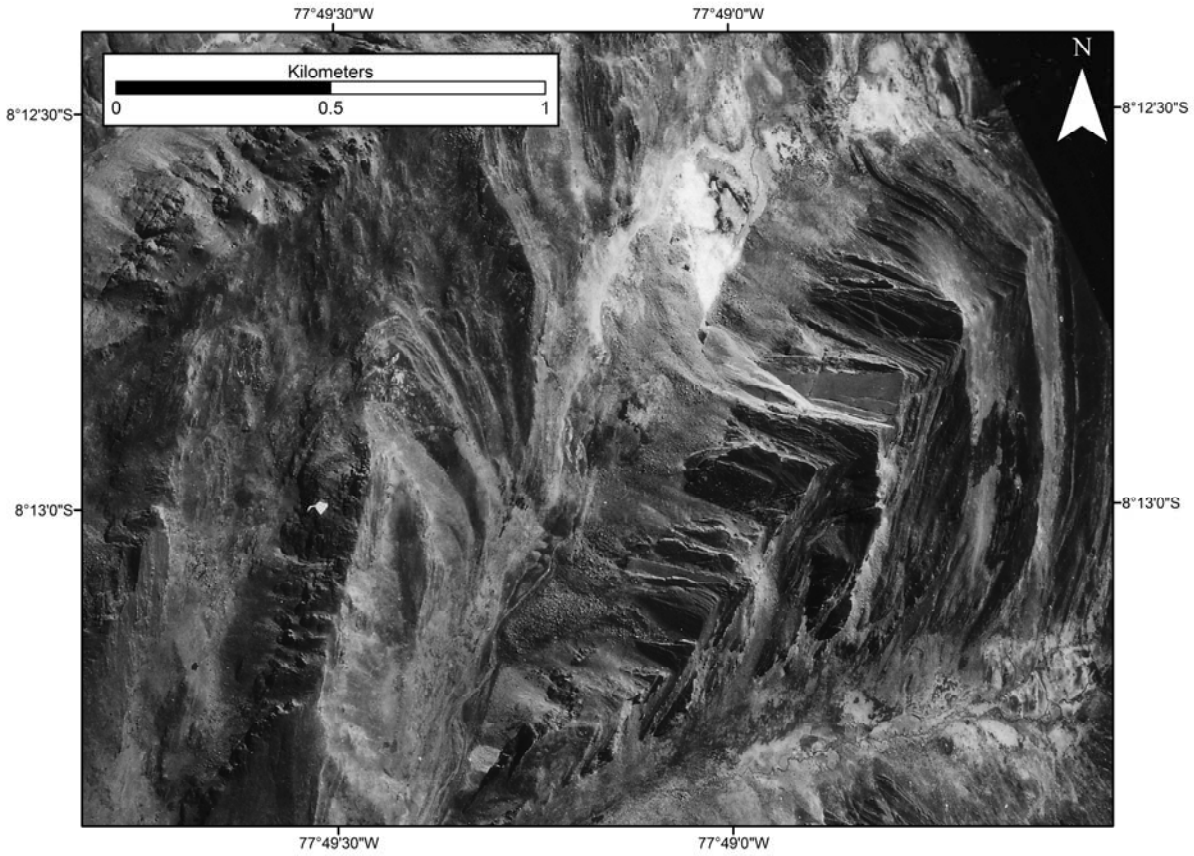

Figure 3. 35: Aerial photograph (1370PMW-MWM173-22474) Blanca rock avalanches

A series of wedge failures along a transverse valley trending northeast-southwest forming the Blanca rock avalanches (Blanca 1, 2, 3, and 4, in Table 2. 3). Wedges have moved to the northwest and are formed by southwest dipping bedding planes (the planar surfaces visible in the image) and steep northeast dipping joints (corresponding to J1 in Figure 3. 5).

Chapter 4
Summary and Contributions

4.1 Inventory of landslides triggered by the M7.3 Ancash Earthquake

This thesis is the first detailed study and quantitative analysis of a landslide-inducing earthquake in Peru and in the Andean region. Based on a literature review, field observations and the interpretation of aerial photographs taken in 1962, a total of 45 landslides are inferred to have been triggered by the M7.3 1946 Ancash earthquake. Significant knowledge gaps concerning the landslides triggered by the 1946 Ancash earthquake have been filled. These include detailed locations, geology, source slope geometry, path geometry and documentation of landslides within the epicentral area of the 1946 event. 83% are rock avalanches involving Cretaceous limestone and shale. The largest rock avalanches occurred at Rio Llama (36,550,546 m^3), Suytucocha (13,503,994 m^3) and Quiches (10,582,563 m^3). A number of rock avalanches involved significant entrainment of colluvial material which enhanced initial failure volumes.

4.2 Landslide Volume and Denudation Rates

Volume estimates were calculated for all 45 earthquake-triggered landslides. Individual landslide volumes vs. frequency plots were comparable to a similar data set of earthquake-triggered landslides for the M6.7 1994 Northridge earthquake (Harp and Jibson, 1995). The total minimum volume of material moved during the 1946 Ancash earthquake was estimated at 0.093 km^3. This volume estimate, plotted against earthquake moment magnitude, plots near the regression line in the empirical relation for earthquake-triggered landslide events developed by Keefer (1994) and Malamud et al. (2004).

A denudation (average surface lowering) of 76 mm was estimated to have occurred over the area of the VIII intensity isoseismal of the 1946 Ancash earthquake due to earthquake-triggered landslides. A denudation rate of 0.00585 mm/yr was estimated to have occurred over the same area based on a recurrence interval for the 1946 Ancash earthquake of 13,000 years (Bellier et al., 1991). This denudation rate may be compared to that for the M6.7 1994 Northridge earthquake at 0.1 mm/yr (Malamud et al., 2004). In addition, the 1946 Ancash denudation is compared to the landslide-based denudation rate calculated for Peru of 0.192 mm/yr and the range of denudation rates calculated for the Andes of 0.01-6.9 mm/yr (Aalto et al., 2006).

The denudation rate for similar earthquakes to the 1946 Ancash event is the lowest rate of these values due to the fact that the recurrence interval for Ancash events is high at 13,000 years. This is due to the fact that the 1946 Ancash earthquake is an intraplate earthquake that occurred in the interior of the South American plate (Doser, 1987). Intraplate earthquakes tend to occur much less frequently than earthquakes which occur along plate boundaries (Johnston and Kanter, 1990).

4.3 Rock Avalanches Initiated by Stepped Wedge Failure

Rock avalanches constituted 83% of the landslides which are inferred to have occurred during the 1946 Ancash earthquake. Many of these rock avalanches display initial failure characteristics typical of wedge failure. Three rock avalanches were analyzed using the conventional wedge failure criteria (Hoek and Bray, 1977). However, two of the rock avalanches did not satisfy the conventional criteria even though they clearly displayed evidence of wedge failure. In order to demonstrate wedge failure at these two rock avalanche sites, a new set of criteria was developed, i.e. stepped wedge criteria.

Stepped wedge failure involves movement along a stepped line of intersection formed by a vertical (or nearly-vertical) discontinuity striking parallel to the slope contours and the conventional line of intersection formed by the bedding and joint set. The nearly-vertical discontinuity also forms the backscarp of the stepped wedge failure. Four characteristics of stepped wedge failure were distinguished based on the examples studied in the epicentral area.

1) Stepped wedge failures occur along valleys which are transverse to the dominant northwest-southeast structural features in the Western Cordillera along both sides of the continental divide.

2) Stepped wedge failures occur along the sides of valleys where the dip direction of bedding planes is parallel to the orientation of the valleys, i.e. the strike of the bedding planes is perpendicular to the orientation of the valley.

3) A steeper stepped line of intersection is fundamental for the development of stepped wedge failure. Therefore, a steep slope is needed for failure in order to accommodate a steeper stepped line of intersection.

4) Lastly, stepped wedge failure is facilitated by very steep bedding planes which act as one of the intersecting discontinuities required for wedge shape development.

4.4 Implications for hazard assessment

This regional study of landslides triggered by the 1946 Ancash earthquake contributes valuable knowledge to the understanding of landslide-inducing earthquakes. The landslide inventory compiled serves as a database for hazard assessment in the Ancash region. It is the first quantitative study of a landslide-inducing earthquake in Peru and the Andean region.

Although the total volume of landslides triggered by the M7.3 1946 Ancash earthquake fits the worldwide empirical relation with respect to earthquake magnitude, low frequency intraplate earthquakes such as the 1946 Ancash earthquake, pose less hazard than higher frequency subduction earthquakes of similar magnitude.

Stepped wedge failure criteria developed in this work can be used to evaluate wedge failure potential in rock slopes where the rock mass displays a nearly-vertical joint set striking parallel to the slope at a right angle to the conventional line of intersection. It is noted that the rock slopes exhibiting this rock mass fabric may appear stable with respect to wedge failure when evaluated using conventional wedge criteria.

Appendix A

Listing of literature sources for landslide-inducing earthquakes, with magnitudes greater than or equal to 7.0, in the Andes (Venezuela, Colombia, Ecuador, Peru, Bolivia, Chile and Argentina) 1890-2007

Alva Hurtado, J.E. and Chang Chang, L., 1985. Mapa de areas de deslizamientos por sismos en el Perú, V Congreso Nacional de Mecánica de Suelos e Ingeniería de Cimentaciones, Lima, Peru.

Askew, B.L. and Algermissen, S.T. (Editors), 1985. Catalog of Earthquakes for South America; Description of the Catalog and National Reports. Earthquake Mitigation Program in the Andean Region (Project SISRA), Volume 1, Lima, Peru, 190 pp.

Cluff, L.S., 1971. Peru earthquake of May 31, 1970; engineering geology observations. Bulletin of the Seismological Society of America, 61(3): 511-533.

Comte, D. and Pardo, M., 1991. Reappraisal of Great Historical Earthquakes in the Northern Chile and Southern Peru Seismic Gaps. Natural Hazards, 4: 23-44.

Davis, S.N. and Karzulovic, J., 1963. Landslides at Lago Rinihue, Chile. Bulletin of the Seismological Society of America, 53(6): 1403-1414.

Ericksen, G.E. and Plafker, G., 1972. Geologic control of destruction during the Peru earthquake of May 31, 1970. Proj. Rep. Peru Inv. (IR) PE-3, USGS, Publications of the U. S. Geological Survey.

Heim, A., 1949. Observaciones geologicas en la Region del Terrmoto de Ancash de Noviembre de 1946. Sociedad Geologica del Peru, Jubilar(II): 1-28.

Keefer, D.K., 1984. Landslides caused by earthquakes. Geological Society of America Bulletin, 95: 406-421.

Keefer, D.K. and Mosely, M.E., 2004. Southern Peru desert shattered by the great 2001 earthquake: Implications for paleoseismic and paleo-El Niño-Southern Oscillation records. Proceedings of the National Academy of Sciences of the United States, 101(30): 10878-10883.

Lliboutry, L., 1975. La catastrophe de Yungay (Perou). , Proceedings of Snow and Ice Symposium. IAHS-AISH Publication, Moscow, 1971, pp. 353-363.

Lomnitz, C., 1970. Major earthquakes and tsunamis in Chile during the period 1535 to 1955. Geologische Rundschau, 59: 938-960.

Murria, J. and Hernandez, A., 1999. Seismological, geological, geotechnical and engineering of the July 9, 1997 Cariaco Venezuela earthquake. In: P.S. Seco e Pinto (Editor), Earthquake geotechnical engineering. Proceedings of the 2nd international conference on earthquake geotechnical engineering. A.A.Balkema, Lisbon, pp. 765-769.

Nieto, A.S., Schuster, R.L. and Plaza-Nieto, G., 1991. Mass wasting and flooding. Natural Disaster Studies, Report: 5: 51-82.

Plafker, G., Ericksen, G.E. and Concha, J.F., 1971. Geological aspects of the May 31, 1970, Peru earthquake. Bulletin of the Seismological Society of America, 61(3): 543-578.

Rodriguez, C.E., Bommer, J.J. and Chandler, R.J., 1999. Eathquake-induced landslides: 1980-1997. Soil Dynamics and Earthquake Engineering, 18: 325-346.

Rojahn, C., Brogan, G.E. and Slemmons, D.B., 1978. Preliminary report, San Juan, Argentina earthquake November 23, 1977. Newsletter - Earthquake Engineering Research Institute, 12(3): 51-69.

Rüegg, W., 1950. Le tremblement de terre d'Ancash (Pérou) du 10 novembre 1946 et ses causes géotectoniques. Travaux de Institut Français d'Études Andines, 2: 153-166.

Schuster, R.L., Nieto, A.S., O'Rourke, T.D., Crespo, E. and Plaza-Nieto, G., 1996. Mass wasting triggered by the 5 March 1987 Ecuador earthquakes. Engineering Geology, 42(1): 1-23.

Scott, K.M., Macias, J.L., Naranjo, J.A., Rodriguez, S. and McGeehin, J.P., 2001. Catastrophic Debris Flows Transformed from Landslides in Volcanic Terrains: Mobility, Hazard Assessment, and Mitigation Strategies. 1630.

Silgado, E.F., 1947. Datos Sismologicos del Peru 1946, Boletín 7. Instituto Geológica del Perú, Ministerio de Fomento, Dirección de Minas y Petróleo, Lima, Perú, 42 pp.

Silgado, E.F., 1951. The Ancash, Peru, earthquake of November 10, 1946. Bulletin of the Seismological Society of America, 41(2): 83-100.

Silgado, E.F., 1978. Historia de los sismos más notables ocurridos en el Perú (1513-1974), Boletin 3. Instituto de Geologia y Minera, Lima, Peru, 130 pp.

Silgado, E.F. and Giesecke, A., 1981. Terremotos en el Perú. Rikchay Perú, Lima, Peru, 142 pp.

Tibaldi, A., Ferrari, L. and Pasquare, G., 1995. Landslides triggered by earthquakes and their relations with faults and mountain slope geometry; an example from Ecuador. Geomorphology, 11(3): 215-226.

USGS., 2007. Earthquake Hazards Program. http://earthquake.usgs.gov/.

References

Aalto, R., Dunne, T. and Guyot, J.L., 2006. Geomorphic Controls on Andean Denudation Rates. Journal of Geology, 114: 85-99.

Alva Hurtado, J.E. and Chang Chang, L., 1985. Mapa de areas de deslizamientos por sismos en el Perú, V Congreso Nacional de Mecánica de Suelos e Ingeniería de Cimentaciones, Lima, Peru.

Bellier, O., Dumont, J.F., Sébrier, M. and Mercier, J.L., 1991. Geological constraints on the kinematics and fault-plane solution of the Quiches fault zone reactivated during the November 10 1946 Ancash earthquake, northern Peru. Bulletin of the Seismological Society of America, 81(2): 468-490.

Benavides-Cáceres, V.E., 1956. Cretaceous System in Northern Peru. Bulletin of the American Museum of Natural History, 108(Article 4): 353-494.

Bommer, J.J. and Rodriguez, C.E., 2002. Earthquake-induced landslides in Central America. Engineering Geology, 63(3-4): 189-220.

Call, R.D., 1992. Chapter 10.4 - Slope Stability. In: H.L. Hartman (Editor), SME Mining Engineering Handbook 2nd Edition. Society for Mining and Metallurgy and Exploration Inc., Littleton, Colorado, pp. 1269.

Call, R.D. and Savely, J.P., 1990. 6.8 Open Pit Rock Mechanics. In: B.A. Kennedy (Editor), Surface Mining 2nd Edition. Society for Mining, Metallurgy and Exploration Inc., Littleton, Clorado, pp. 1194.

Centre for Research in Water Resources, 1999. Digital Atlas of the World Water Balance, Version 3.0 The University of Texas at Austin, Austin, Texas.

Cobbing, E.J. et al., 1981. The geology of the Western Cordillera of northern Peru. Overseas Memoir 5. Institute of Geological Sciences, London, 143 pp.

Cruden, D.M. and Hu, X.Q., 1988. Basic friction angles of carbonate rocks from Kananaskis Country, Canada. Bulletin of the International Association of Engineering Geology, 38(1): 55-59.

Doser, D.I., 1987. The Ancash, Peru, earthquake of 1946 November 10: evidence for low-angle normal faulting in the high Andes of northern Peru. Geophysical Journal of the Royal Astronomical Society, 91(1): 57-71.

Ericksen, G.E., Plafker, G. and Fernandez Concha, J., 1970. Preliminary report on the geologic events associated with the May 31, 1970, Peru earthquake. U. S. Geological Survey Circular, 639: 1-25.

ESRI Canada Schools and Libraries Program, 2005. Global Elevation with Shaded Relief, ArcCanada 3.1: Schools and Library Edition, Toronto, ON.

Goodman, R.E., 1976. Methods of Geological Engineering in Discontinuous Rocks. West Publishing Company, St. Paul, MN, 472 pp.

Harp, E.L. and Jibson, R.W., 1995. Inventory of landslides triggered by the 1994 Northridge, California earthquake: U.S. Geological Survey Open-File Report 95-213.

Heim, A., 1948. Wunderland Peru. Verlag Hans Huber, Bern, 301 pp.

Heim, A., 1949. Observaciones geologicas en la Region del Terrmoto de Ancash de Noviembre de 1946. Sociedad Geologica del Peru, Jubilar(II): 1-28.

Hoek, E. and Bray, J.W., 1977. Rock Slope Engineering, 2nd edition. The Institution of Mining and Metallurgy, London, UK, 402 pp.

Johnston, A.C. and Kanter, L., 1990. Earthquakes in stable continental crust. Scientific American, 262: 68-75.

Keefer, D.K., 1984. Landslides caused by earthquakes. Geological Society of America Bulletin, 95: 406-421.

Keefer, D.K., 1994. The importance of earthquake-induced landslides to long-term slope erosion and slope-failure hazards in seismically active regions. Geomorphology, 10(1-4): 265-284.

Keefer, D.K. and Mosely, M.E., 2004. Southern Peru desert shattered by the great 2001 earthquake: Implications for paleoseismic and paleo-El Niño-Southern Oscillation records. Proceedings of the National Academy of Sciences of the United States, 101(30): 10878-10883.

Khazai, B. and Sitar, N., 2004. Evaluation of factors controlling earthquake-induced landslides caused by Chi-chi earthquake and comparison with the Northridge and Loma Prieta events. Engineering Geology, 71(1-2): 79-95.

Kliche, C.A., 1999. Rock Slope Stability. SME, 253 pp.

Macharé, J. et al., 2003. Database and Map of Quaternary Faults and Folds in Peru and its Offshore Region, U.S. Geological Survey.

Malamud, B.D., Turcotte, D.L., Guzzetti, F. and Reichenbach, P., 2004. Landslides, earthquakes, and erosion. Earth and Planetary Science Letters, 229(1-2): 45-59.

McNulty, B.A., Farber, D.L., Wallace, G.S., Lopez, R. and Palacios, O., 1998. Role of plate kinematics and plate-slip vector partitioning in continental magmatic arcs: Evidence from the Cordillera Blanca, Peru. Geology, 26(9): 827-830.

National Geospatial - Intelligence Agency, 2008. GeoNET Names Server, Bethesda.

Norabuena, E.O. and Snoke, J.A., 1994. Structure of the subducting Nazca Plate beneath Peru. Journal of Geophysical Research, 99(B5): 9215-9226.

Norrish, N.I. and Wyllie, D.C., 1996. Chapter 15: Rock Slope Stability Analysis. In: A.K. Turner and R.L. Schuster (Editors), Landslides Investigation and Mitigation Special Report 247. Transportation Research Board - National Research Council, Washington, D.C., pp. 391-425.

Öcal, A. and Özgenoğlu, A., 1997. Technical Note - Determination of Sliding Mode of Tetrahedral Wedges in Jointed Rock Slopes. Rock Mechanics and Rock Engineering, 30(3): 161-165.

Piteau, D.R., 1972. Enginering Geology Considerations and Approach in Assessing the Stability of Rock Slopes. Bulletin of the Association of Engineering Geologists, 9(3): 301-320.

Plafker, G., Ericksen, G.E. and Concha, J.F., 1971. Geological aspects of the May 31, 1970, Peru earthquake. Bulletin of the Seismological Society of America, 61(3): 543-578.

Rüegg, W., 1950. Le tremblement de terre d'Ancash (Pérou) du 10 novembre 1946 et ses causes géotectoniques. Travaux de Institut Français d'Études Andines, 2: 153-166.

Sanchez Fernandez, A.W., 1995. Mapa geologico del cuadrangulo de Pallasca, Departamento de Ancash. Instituto Geologico Minero y Metalurgico, Ministerio de Energia y Minas, Republica del Peru.

Silgado, E.F., 1947. Datos Sismologicos del Peru 1946, Boletín 7. Instituto Geológica del Perú, Ministerio de Fomento, Dirección de Minas y Petróleo, Lima, Perú, 42 pp.

Silgado, E.F., 1951. The Ancash, Peru, earthquake of November 10, 1946. Bulletin of the Seismological Society of America, 41(2): 83-100.

Silgado, E.F., 1978. Historia de los sismos más notables ocurridos en el Perú (1513-1974), Boletin 3. Instituto de Geologia y Minera, Lima, Peru, 130 pp.

Silgado, E.F. and Giesecke, A., 1981. Terremotos en el Perú. Rikchay Perú, Lima, Peru, 142 pp.

Stauder, W., 1975. Subduction of the Nazca Plate under Peru as evidenced by focal mechanisms and by seismicity. Journal of Geophysical Research, 80(8): 1053-1064.

Suárez, G., Molnar, P. and Burchfield, B.C., 1983. Seismicity, fault plane solutions, depth of faulting, and active tectonics of the Andes of Peru, Ecuador, and southern Columbia. Journal of Geophysical Research, 88(B12): 10,403-10,428.

Utsu, T., 2002. A List of Deadly Earthquakes in the World: 1500-2000. In: W. Lee, H.K., H. Kanamori, P.C. Jennings and C. Kisslinger (Editors), International Handbook of Earthquake and Engineering Seismology. Academic Press, London, pp. 691-717.

Wilson, J.J., 1963. Cretaceous stratigraphy of central Andes of Peru. Bulletin of the American Association of Petroleum Geologists, 47(1): 1-34.

Wyllie, D.C. and Mah, C.W., 2004. Rock Slope Engineering, 4th Edition. Spon Press, New York, 431 pp.